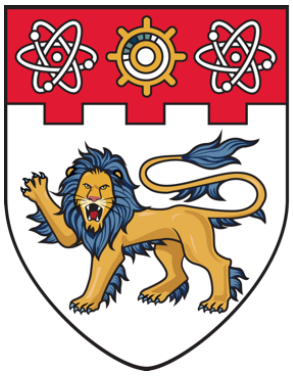

NANYANG TECHNOLOGICAL UNIVERSITY
SINGAPORE

NONGENETIC ENGINEERING OF SUBCELLULAR TARGETED THERAPEUTIC AGENTS TO FACILITATE PRECISE CELL ACTIVITY MANIPULATION

DO CONG THANG

SCHOOL OF PHYSICAL AND MATHEMATICAL SCIENCES

2021

NONGENETIC ENGINEERING OF SUBCELLULAR TARGETED THERAPEUTIC AGENTS TO FACILITATE PRECISE CELL ACTIVITY MANIPULATION

DO CONG THANG

SCHOOL OF PHYSICAL AND MATHEMATICAL SCIENCES

A thesis submitted to the Nanyang Technological University in partial fulfilment of the requirement for the degree of Doctor of Philosophy

2021

Statement of Originality

I hereby certify that the work embodied in this thesis is the result of original research done by me except where otherwise stated in this thesis. The thesis work has not been submitted for a degree or professional qualification to any other university or institution. I declare that this thesis is written by myself and is free of plagiarism and of sufficient grammatical clarity to be examined. I confirm that the investigations were conducted in accord with the ethics policies and integrity standards of Nanyang Technological University and that the research data are presented honestly and without prejudice.

30 July 2021

Date

Do Cong Thang

Supervisor Declaration Statement

I have reviewed the content and presentation style of this thesis and declare it of sufficient grammatical clarity to be examined. To the best of my knowledge, the thesis is free of plagiarism and the research and writing are those of the candidate's except as acknowledged in the Author Attribution Statement. I confirm that the investigations were conducted in accord with the ethics policies and integrity standards of Nanyang Technological University and that the research data are presented honestly and without prejudice.

4th Aug 2021

Date

Xing Bengang

Authorship Attribution Statement

This thesis contains material from [2] papers published in the following peer-reviewed journal(s) / from papers accepted at conferences in which I am listed as an author.

Part of chapter 1 is published as D. C. Thang, Z. Wang, X. Lu, B. G. Xing, Precise Cell Behaviors Manipulations Through Light-Responsive Nano-regulators: Recent Advance and Perspective. *Theranostics*. 2019, 9, 3308. DOI: 10.7150/thno.33888

The contributions of the co-authors are as follows:

- Prof Xing Bengang provided the initial project direction and edited the manuscript drafts.
- I prepared the manuscript drafts. The manuscript was revised by Dr Wang Zhimin and Dr. Lu Xiaoling.

Chapter 2 is published as D. C. Thang, Z. Wang, M. Hu, Q. Y. Han, B. G. Xing, Extra-Specific Manifestation of Nanoheater's Position Effect on Distinctive Cellular Photothermal Response. *ACS Nano*, 2020, 14, 5836. DOI: 10.1021/acsnano.0c00951

The contributions of the co-authors are as follows:

- Prof Xing suggested the initial project direction and edited the manuscript drafts.
- I performed all the materials synthesis and characterization, cellular analysis and conducted data evaluation.
- I wrote the drafts of the manuscript. The manuscript was revised together with Dr. Zhimin Wang, Dr. Hu Ming, and Ms. Qinyu Han.

30 July 2021

Date

Do Cong Thang

Abstract

Precise cellular event manipulation is highly demanded in current development of biomedical therapeutics. This direction requires highly interdisciplinary design systems that revolutionize cell fate regulation. To achieve precise cellular modulation, thorough understanding of therapeutic agents entering the cells is required. The localization of such agents within the complex three-dimensional cellular structure has substantial implications in the precise activation of signal transduction and recruitment of functional components to regulate cell events and stress responses. Therefore, spatiotemporal modulation of organelle functions and signaling pathways offers ample opportunities in the understanding of disease procession. The above-mentioned methods can be utilized to expedite targeted theranostics with utmost efficacy.

In chapter 2, we investigate photothermal nanotheranostics under the influence of nanoheaters' subcellular distribution and their molecular mechanism on cellular heat response. We revealed the biological basis of divergent thermal effects at subcellular resolution by localizing photothermal nanoparticles into specific locations of cell sections. The cell surface conjugation and the lysosomal cellular uptake nanoheaters induced similar level of heat shock protein expression in live cells after photothermal excitation. However, heat stress from lysosome distribution nanoparticles promoted apoptosis through activation of Bid protein, whereas the heat from clusters of cell membrane localized nanoheater stimulated more membrane structure perturbation and necrotic cell death. This study stipulates intuitions underlying the different subcellular positions of nanoparticles for the selective thermal response, which provides valuable perspectives on optimal precision nanomedicine.

In chapter 3, we developed furin cleavable peptide-substrate caged metabolic precursors that can be specifically cleaved in the cytoplasm of targeted tumor cells. Upon specific uptake and cleavage of the furin peptide moiety, the free azide sugar is released after self-immolation of the linker. The unnatural sugar subsequently undergoes a metabolic process to express clickable azide functional group on the cancer cell surface. The conjugated N_3 can therefore

be easily labelled with DBCO-Cy3 which offers efficient, stable and selective conjugation of therapeutics agent independent of its uptake efficiency.

In chapter 4, we introduce a strategy to degrade casein kinase 2α (CK2α) protein using PROTAC molecules. The heterobifunctional degraders were designed based on one warhead which specifically targets the CK2α protein, linked with a E3 ligase, CRBN. Upon incubation, the protein of interest was ubiquitinated and depleted by the 26S proteasome machinery. Our designed molecules exhibited concentration and time dependent degradation of CK2α in different cell lines and zebra fish. “Hook effect” was also observed in which high concentration beyond a certain threshold reduced its efficacy due to saturation of unfavorable binary complexes. Further studies are in progress to investigate the loss of protein function on the downstream effect of cellular regulations.

In chapter 5, we propose a different type of small molecule protein degrader to deplete a protein of interest in specific type of cells. Unlike PROTAC molecules which require connection of two functional groups including protein ligand and the E3 ligase targeting moiety, molecule glues offer simpler chemical structure and are more applicable as clinical drugs. Lenalidomide and analogs of thalidomide is a CRBN E3 ligase targeting substrate that is known to degrade other proteins such as Ikaros and CK1α. Upon intracellular administration, this simple molecule showed uniquely high affinity to both proteins, triggering the proteolysis. In this chapter, a nitroreductase responsive moiety was introduced into the lenalidomide structure. Under hypoxic conditions, the caging moiety was removed, releasing the free lenalidomide to function as a CK1α protein degrader. This study paved new insights in the development of small molecule for protein degradation in selected cell type.

Acknowledgements

First, I would like to thank Nanyang Technological University for the precious opportunity to study and explore within a professional and convenient atmosphere.

Second, I would like to express my deepest gratitude to my supervisor Professor Xing Bengang for his continuous support and encouragement throughout these four years. Thank you for being patient, enthusiastic guidance and all the perpetual hope that he has placed on me. After several years working under him, I am grateful for becoming a more critical thinker, more skillful in experiment conducting, more professional in scientific paper preparation, presentation and importantly becoming a more independent researcher.

Thirdly, I would like to express my appreciation for all the lab members and friends, Dr. ZHANG Zhijun, Dr. LYU Linna, Dr. CHEONG Haolun, Dr. HU Ming, Dr. WANG Zhimin, Ms. KWEK Jia Min, Germain, Mr. SZETO Wai Mun, Dominic, Mr. LANG Wenchao for the kind help and discussion. Great thanks to my first inspirational mentor Dr. AI XiangZhao for giving me assistances from the first day I joining to Prof. Xing's lab and his constant support until this moment. Many thanks to two of my best friends in the lab, Mr. Lau Jun Wei, Ms. Han Qinyu for all the help in doing research as well as mental support to relieve stress and enjoy the research. Thank you to teach me the importance of help, kindness and of working together. Because of you guys, I no longer feel lonely and believe more in myself. Special thanks to my special friend, Ms. Trang for being by my side all the time, caring and supporting me from a long distance that make me feel my Vietnam never far away during these four years.

Finally, I would love to thank my family members who always beside me during those 27 years. Thank you to take care and always believe in me as a reason for me to overcome all the

difficulties that I faced during the long period of studying abroad. I would not be able to go this far without the love, warmth, and peace in the family.

Table of Contents

Chapter 1. General Introduction

Precise cellular event manipulation is of high demanded in specific biomedical applications.[1] This interdisciplinary frontier has perceived abundant efforts in designing systems that can regulate cell fate for theranostic innovations. Nevertheless, relevant clinical applications of these systems are still limited due to general side effects stemming from off-target accumulation of therapeutics agents, lack of tunable monitoring over amplitude, time and location at deep tissue level.[2] These circumstances drove the advancement of stimulous-responsive platforms which exploit endogenous stimuli (such as pH, enzyme and redox reactions, etc.) and exogenous stimuli (such as light, magnetic fields, ionizing irradiation, etc.). However, simply delivering the targeted therapeutic agents into a cell is not enough to understand the mechanism of action and the cellular response pathways. Therefore, intensive consideration should be placed to investigate the localization of the agents endogenously. Approaches in targeting specific organelles could develop therapeutics for disorders that have a root cause in a particular organelle. For example, increasing evidence for the role of mitochondrial dysfunction in cardiovascular diseases suggest that directly targeting the mitochondria could be a valuable approach.[3] Likewise, targeting small molecules to the lysosome for treatment of lysosomal storage disorders, or targeting the endoplasmic reticulum in Alzheimer's disease or diabetes, could potentially contribute to the development of disease related therapeutics.[4] In this chapter, we summarize approaches in targeting different chemical agents specifically to subcellular compartments and their applications in achieving efficient non-genetic regulation of cell activities and its ultimate goal of disease diagnosis and therapy.

1.1 Plasma membrane targeted engineering

1.1.1. Insertion of hydrophobic moiety into the lipid bilayer

Therapeutic agents can be conjugated with hydrophobic moieties to anchor it on the cell membrane. Principally, spontaneous insertion into the lipid bilayer can be attained through a thermodynamically favored mechanism. Hydrophobic moieties including alkyl chain, lipid groups, glycosylphosphatidylinositol (GPI) anchors or cholesterol have been popularly recruited to induce membrane insertion. The relative ease of such membrane anchoring has been applied to attach a variety of cargo for cellular monitoring namely fluorescent dyes, aptamers, peptide, and antibody. For example, GPI has been used to tether a membrane potential fluorescent dye indicator, nile red onto the cell membrane to manifest the direct neuronal voltage with wash-free imaging and to detect supra- and sub-threshold activity.[5] Similarly, by using alkyl chain, FRET probes were attached to the membrane bilipid layers to specifically manifest the proteolytic activity on cell surface. As the furin enzyme perform differently at localized subcellular area, insertion of small molecular probes in the membrane offers opportunities to visualize its function real time.[6] Macromolecules such as oligonucleotides have been installed as well, enabling the clustering of cells functionalized with complimentary sequences.[7] DNA probes were attached to the membrane by diacyl lipid chains for metal ion sensing in extracellular microspace. The membrane-anchored DNAzyme reported and semi-quantified exogenous as well as cell-extruded ions in real time.[8] (**Figure 1**). Nanoparticles as well as polymers have also been attached as larger cell-targeting scaffolds, including nanoparticles [9] and polymers.[10]

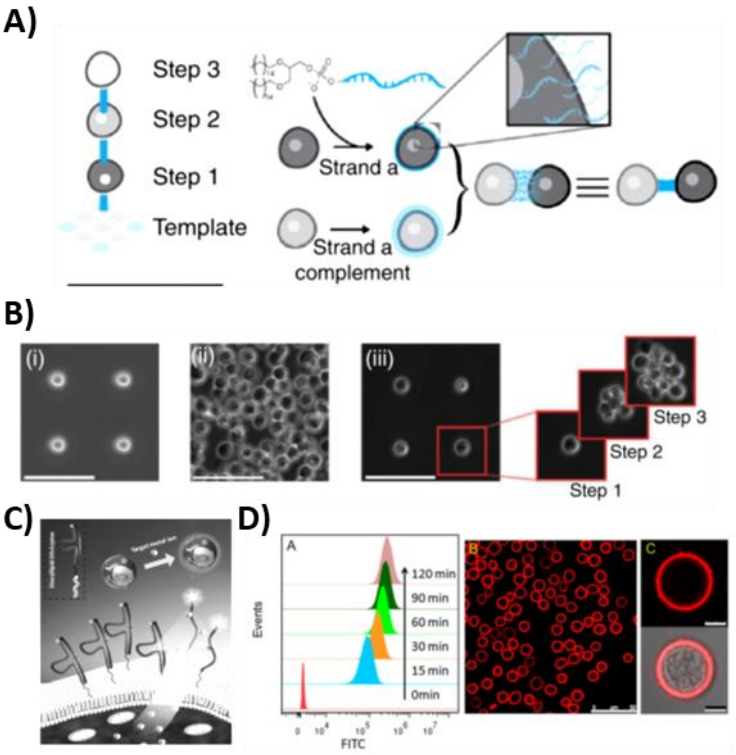

Figure 1: **A**) Lipid-modified oligonucleotides induce cell surface chemical modelling and adhesion. **B**) Programmed assembly following i) DNA spots, (ii) cells in a flow cell and (iii) a single-cell array.[7] **C**) Modification of cell membranes with diacyllipid-DNA probes. **D**) Flow cytometry assay and confocal images of CEM cells after diacyllipid-DNA-FITC treatments.[8]

1.1.2. Chemical modification or ligand-receptors interacting of cell surface components.

The surface area of the cell consists of a variety of functional groups and receptors that can be employed for direct chemical conjugation and interaction. This straightforward method offers a convenient and stable remodeling of the cell membrane. Commonly, amine and thiol groups are ubiquitously present on the membrane proteins. Free amines on the lysine group can be readily targeted without any cell pretreatment. Other than proteins, other component can also be chemically modified such as lipid, carbohydrate or glycans. Although lacking specificity, this method has been extensively applied for induction of intercellular interaction

and cell function mediation. The most used method is to react N-hydroxysuccinimide (NHS)-activated esters with amine groups of lysine or arginine residues. Cells will be treated with NHS-biotin group prior to conjugation with other cargo. By this method, antibodies recognizing epithelial growth factor receptor (EGFR) can be tethered on the cell surface with enhanced ability to interact with the EGFR expressing cell such as HEK293T and Hela.[11] Likewise, streptavidin labelled cells can directly mediate the formation of cell clusters and layers.[12] Maleimide group can also be introduced into the cell surface by this method which could consequently induce the conjugation of thiolated agents or nanoparticles via Michael addition of sulfhydryl groups.[13] In addition, 3-(acrylamide)phenylboronic acid can be used for the binding with membrane glycoproteins through covalent boronate ester bonds to generate a crosslink of cells as form of cell aggregations.[14]

Membrane receptors or proteins can also be targeted for the attachment of designed cargo. For example, the tropane analog dichloropane is a potent ligand of dopamine and norepinephrine transporters (DAT and NET respectively). 6-pyrrolyl-7-trifluoromethyl-quinoxaline-2,3-dione (PFQX), a ligand for α-amino-3-hydroxy-5-methyl-4-isoxazolepropionic acid (AMPA)-type glutamate receptor (AMPAR) was conjugated onto a dextran polymer carrier for molecule-specific targeting of voltage sensitive dyes by selectively binding the target membrane proteins.[15] (**Figure 2)**.

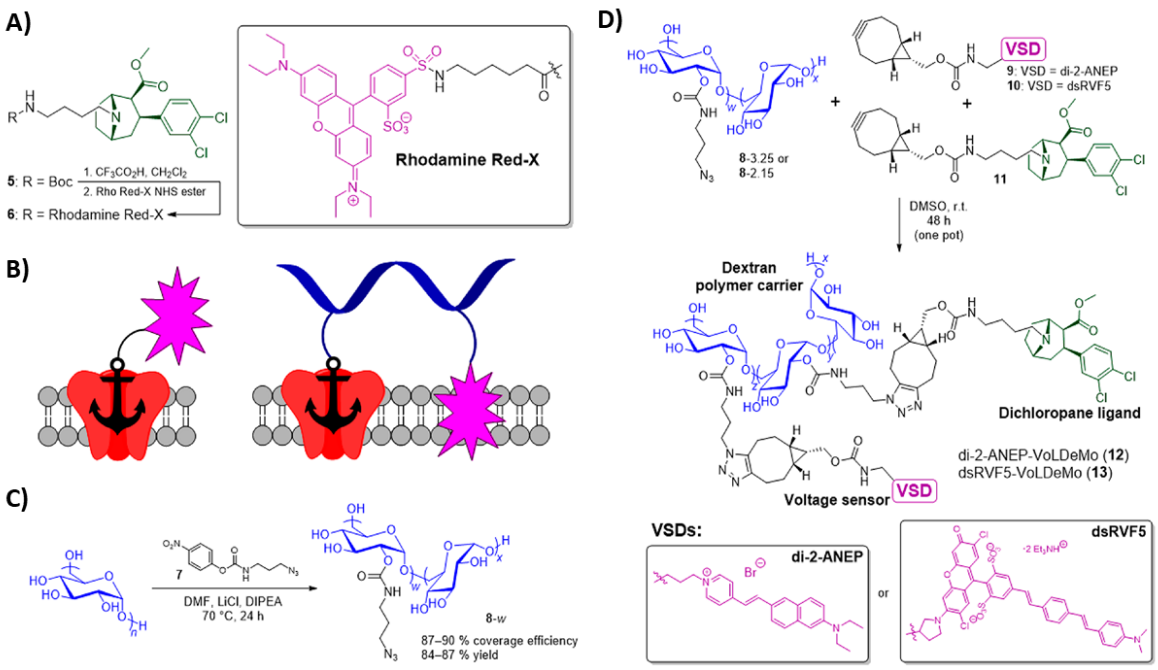

Figure 2. Design and synthesis of DAT/NET-targeted fluorescent probes. **A**) Dichloropane ligand bearing a Boc-4-aminobutyl linker (**5**) and its transformation into probe **6**. **B**) Schematic illustration of ligand–dye fusion concepts. **C**) Synthesis of azidopropyl-carbamate-dextran(6000). **D**) One-pot assembly of VoLDeMo via click chemistry by the reaction of N_3-dextran 8-w (w = 3.25 or 2.15) with a 1:2 mixture of VSD **9** or **10** and ligand **11**.[15]

By using this strategy, cell selective delivery and targeting can be attained due to the different level of receptors and biomarkers in different cell lines. The HER family of receptor tyrosinase kinase which consist of epidermal growth factor receptor (EGFR, also called HER-1 or erbB-1), HER-2 (also called erbB-2 or Neu), HER-3 and HER-4 (also called erbB-3 and erbB-4, respectively) are frequently overexpressed in human carcinomas, primarily breast and squamous cancer. The trans-membrane proteins EGFR are activated upon binding with peptide growth factors of the EGF-family of proteins. Antibody-drug conjugates (ADCs) and antibody-nanoparticle conjugates (ANCs) extensively rely on such

receptors for targeted cell selective delivery as well as for plasma membrane perturbation (**Figure 3**).[16,17]

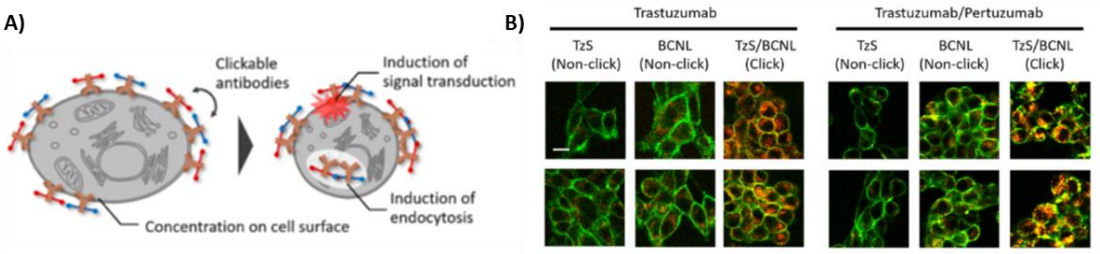

Figure 3. A) Design of Cell Surface Antibody Cross-Linking. B) Confocal fluorescence images of 3T3 $HER2^{+}$ cells indicated mixtures of Tra-TzS, Tra-BCNL, Per-TzS, and PerBCNL.[17]

1.1.3. Fusion of functionalized liposome.

Lipid membrane fusion is a critical process in cell biology which have been intensively investigated and adapted in multiple applications especially in cell engineering. Biologically and chemically functionalized liposomes spontaneously fuse with natural cells to present respective functions on the receiver. By using this approach, ketone or oxyamine groups which originated from palmitoyl-oleoyl phosphatidylcholine, 1,2-dioleoyl-3-trimethylammonium-propane, and either dodecanone or O-dodecyloxyamine was presented on the cell surface. The receivers bearing such moieties can easily be further functionalized with other groups through a covalent oxime ligation.[18,19] Similarly, vesicles containing the biotinylated lipid 1,2-dioleoyl-sn-glycero-3-phosphoethanolamine- N-(biotinyl) (Bio-PE) was used for tagging of biotin on cell membrane which enabled the bridging of biotinylated moiety via streptavidin.[20] Liposome-like particles or extracellular vesicles (EVs) can be collected from pre-conditioned cells based on the nature vesicles induction of the cells. The

parental cells were initially treated with the synthetic receptors (SRs) delivered from lipid-based nanoparticles. Subsequently, the functional components could be further incorporated in the membrane of EVs secreted from the cells. As a result, SRs could be created on neighbouring cells via EV-mediated intercellular lipid transfer (**Figure 4**). Substantial membrane specific spreading of SRs was attained leveraging effective membrane targeted phototherapy because of membrane photodamage.[21]

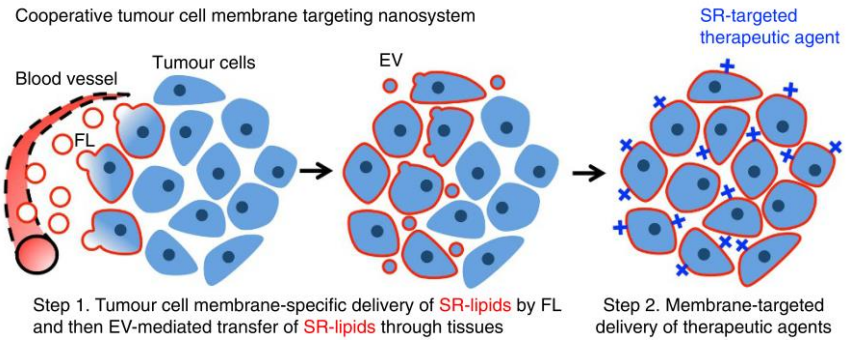

Figure 4. Schematic representation of cooperative tumour cell membrane targeting nanosystem.[21]

1.1.4. Metabolic sugar labelling of glycoproteins on the cell surface

Glycosylation is an important process in monitoring cellular activity, immune response, transportation, and recognition. The process involves post-translational modification of carbohydrate molecules onto specific amino acid residues on proteins which form glycoproteins. The glycoproteins are ubiquitous in cells and are mostly found on the cell membrane. A thick layer of oligosaccharide chain covering the extracellular matrix of the cell is therefore a pivotal target for modification. The metabolic labelling of the cells could be attained by modifying the native metabolic process with unnatural sugar analogs.[22] This method basically relies on the sugar savage pathways of the sugar derivative such as N-

acetylmannosamine (ManNAc) with additional carbons on the N-acetyl position which is transformed to sialic acid derivatives and labelled onto cell surface glycoproteins.[23] Further extending the sugar analogs with biorthogonal moieties could leverage the covalent bonding of adducts with high selective and reactive manner.[24] To this end, multiple monosaccharide analogs were developed to target different subtypes of glycosylation (**Figure 5**). Cell and tissue specific labelling of azide-clad monosaccharides in heterogenous cellular environments expands the utility of the sugar labelling method.

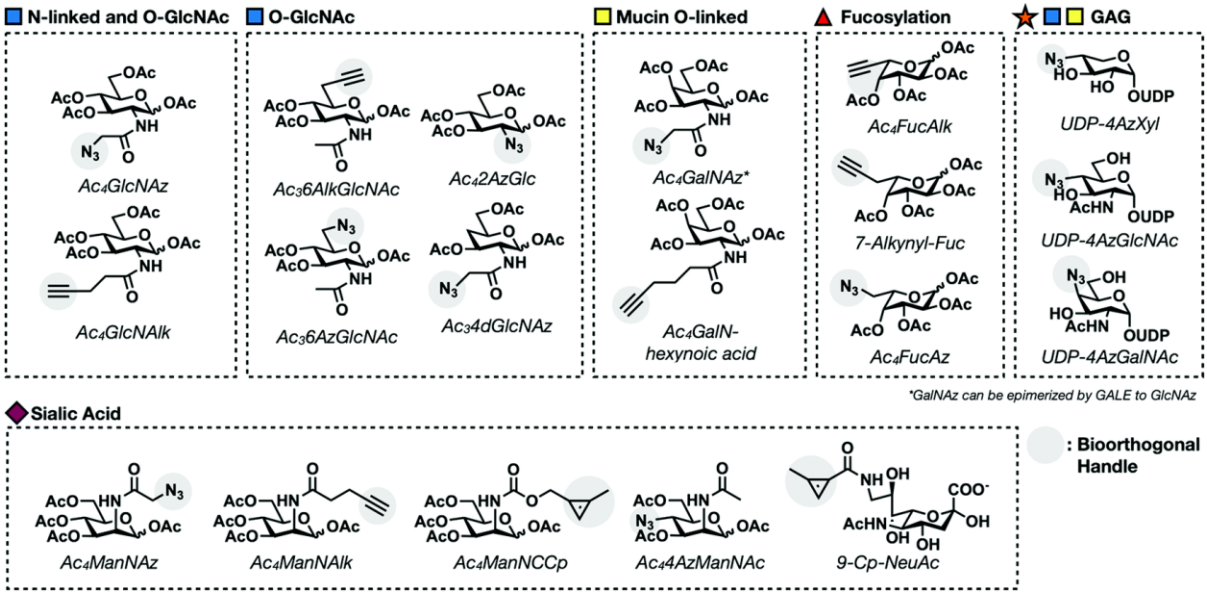

Figure 5. Examples of first generation metabolic chemical reporters for different glycosylation events.[24]

Applying the native metabolic glycol-biosynthesis pathways to conjugate click inducible groups on the cell membrane, multiple biological cargo were introduced for tracking, manipulating and ablating targeted cells. Our group has recently attached 808 nm light responsive upconversion nanoparticles on the membrane through a modified dibenzyl cyclooctyne (DBCO) moiety with the azide sugar in the glycoconjugate after treatment with

peracetylated N-azidoacetylmannosamine (Ac_4ManNAz). Upon NIR light illumination, the upconverted green emission at 480 nm from UCNs could specifically activate the light-gated channelrhodopsins-2 proteins (ChR2), and therefore regulate cation influx (e.g., Ca^{2+}) across the cell membrane. This extracellular conjugation method enhanced the specificity of ion channel activation with alleviated amount of nanoparticle uptake and laser power used to produce physiological impacts which potentially increase cellular toxicity. Directed cell membrane damage could also be attained by generating reactive oxygen species at localized area. An alkyne-functionalized water-soluble bioorthogonal turn-on probe (TPEBAI) with photosensitizing ability was stabilized specifically on the cancer cell membrane. Upon irradiation with light, ROS production was observed to be overexpressed on the cancer cell and increased its toxicity in a precise manner.[25] Immunomodulation of the cell can also be obtained via expressing antibody, ligand, antigen or cytokine specifically on the extracellular surface. Stable and covalent installation of the antibody recruiting moieties was realized through selective delivery of 1,3,4-O-acetyl-Nazidoacetylmannosamine (Ac_3ManNAz) to folate receptor-overexpressing cells via Ac_3ManNAz-folate. Upon close proximity with folate receptors, the cleavable linker was released thereby introducing azido group on the cell surface glycan as a platform to anchor L-rhamnose (Rha), a hapten, via click chemistry with DBCO-Rha. The Rha-attached cells were able to recruit anti-Rhamnose antibody which enhanced the destruction of cancer cell through complement-dependent cytotoxicity and antibody-dependent phagocytosis.[26] Likewise, dendritic cells were tracked and modulated via azido-sugar. Azido-labelled dendritic cells (DCs) were detected in lymph nodes for weeks by monitoring the fluorescence signal from the Cy5 dye which was attached to the DCs via click reaction with DBCO-Cy5. Moreover, DCs could covalently capture DBCO-bearing antigens and adjuvants for improved antigen-specific CD8+ T-cell responses and antitumour efficacy.

In addition, DBCO-cytokine (e.g., DBCO–IL-15/IL-15Rα) was introduced to improve the priming of antigen-specific CD8+ T cells and regulation of DC-T cell interactions *in vivo* (**Figure 6**). [27]

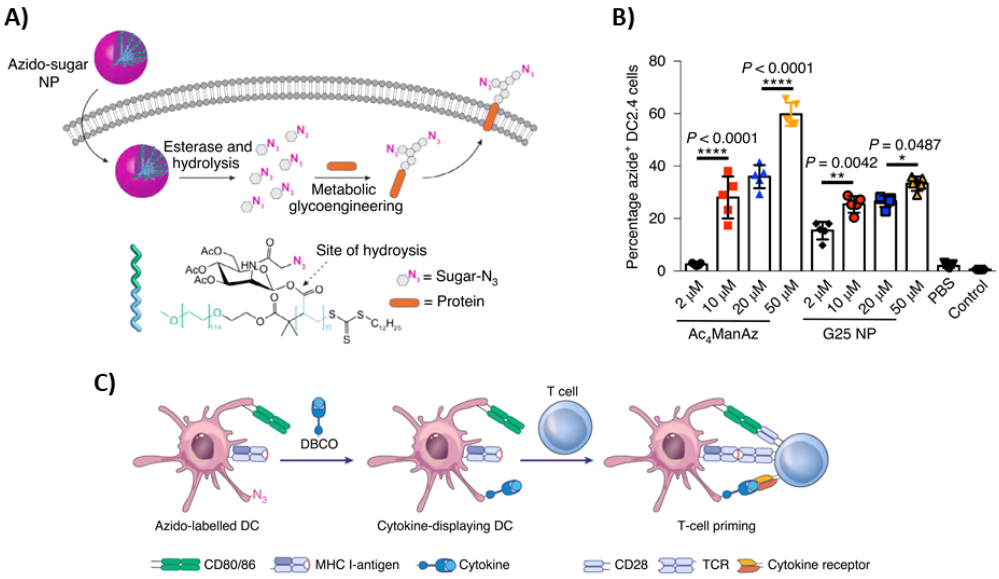

Figure 6. **A**) Illustration of labelling of dendritic cells with azido-sugar nanoparticles under endocytosis disassembling of azide-sugar. **B**) Percentage of azide+ DC2.4 cells after incubation with Ac_4ManAz or G25 NP. **C**) Labelling of DBCO-cytokines to azido-labelled DCs and subsequent T-cell priming.[27]

1.1.5. Membrane protein modification by enzymes

A less common strategy to model the cell membrane is to use enzymes to trigger the labelling of surface protein and glycans. For example, "sortagging" technique was used by exploiting the activity of Staphylococcus aureus enzyme sortase A. The conjugation of LPXTG-tagged probes and LPXTG-proteins to endogenous membrane was attained on the N-terminal glycine of activated CD8 T cell which redirected specific toxicity of the cell with relevant antigen.[28] Proteins could also be recruited to the inner cell membrane by tethering a peptide derived from the protein K-Ras4B to yield a sequence that is a known substrate for protein

farnesyltransferase. After the formation of a farnesylated product, the peptide was able to translocate from the cytosol/ Golgi to the plasma membrane through enzymatic palmitoylation. This migration method relies on the cysteine-containing peptide, opening a plethora of application for activation of proteins signaling pathways.[29]

1.2. Lysosome chemical engineering

Lysosomes are well known as degradation endpoints of intracellular and exogenous cargo. Their catabolic functionality is accomplished by approximately 60 proteases, nucleases, enzymes that are encapsulated in an acidic condition created by ATP-driven pumps, and vacuolar H^+-ATP in harmony with ion channels. Its harsh pH 4.5 condition with multiple enzymes assist the lysosome and its equivalent structures to break down macromolecules into smaller building blocks and metabolites. Some of the products including amino acid, nucleotides, sugars, lipids are exported to the cytoplasm by an array of permeases along the lysosomal membrane which can be readily used by the cell. In addition, it can also be stored for post-usage such as buffering of cytoplasmic environment and regulating interactions with other membrane compartments like the controlled release of calcium ion. Metal ions such as zinc, iron, copper, can also be capped inside lysosome to prevent its uncontrolled harmful accumulation in cytoplasm.[30]

Lysosomal dysfunctions are therefore the root cause of many human diseases originating from its mutations in luminal hydrolase, permease, or storage disorders. Uncontrolled accumulation of digestion products inside the lysosomal lumen may result in pathophysiological consequences including neurodegeneration, growth retardation or metabolic imbalance. Once the basic balance of the lysosome is perturbed, their inter-

organelle communication will also be affected due to their malfunction in trafficking and fusion.

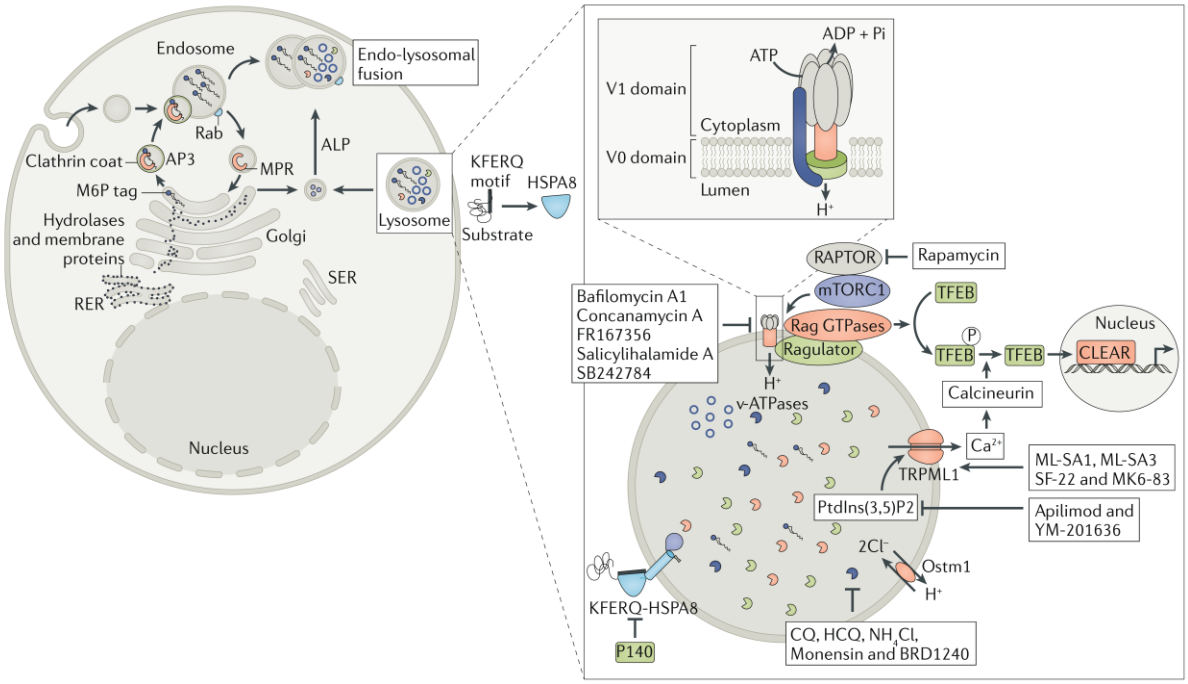

Figure 7. Lysosomal processes and sites as target for chemical engineering. CLEAR, coordinated lysosomal expression and regulation; CQ, chloroquine; HCQ, hydroxychloroquine; mTORC1, mTOR complex 1; PtdIns(3,5)P2, phosphatidylinositol-3,5-bisphosphate; RAPTOR, regulatory-associated protein of mTOR; SER, smooth endoplasmic reticulum; TFEB, transcription factor EB.[31]

Figure 7 illustrates the mechanism in which the substrates are recruited and degraded through the endo-lysosomal pathway. Among the lysosomal enzymatic system that transport cargo from Golgi to lysosome, the most well-known system is the mannose-6-phosphate (M6P) receptor which targets newly synthesized hydrolase and escort them to pre-lysosomal compartments. Some of the components have become major targeting site for lysosomal dysfunction such as membrane proteins (mTOR as mechanistic target of rampamicin),

enzymes, ion channels (TRPML1, Ostm1) and other chaperone-mediated transportation which can be manipulated by many pharmacological antagonists and agonists. When considering lysosomal target, it is necessary to not only target all lysosomes, but also to enhance its specificity in localizing on lysosomal proteins or components of defective lysosomal organelle or cells.[31]

Lysosomal storage diseases and aging cells are normally elevated in acidic lysosomes. Chemically targeting lysosome typically relies on acidotropic compounds that accumulate in the lysosome due to its acidity. Fluorescent dyes that turn-on under acidic condition can be employed to track the lysosome. An example of this labelling method is the use of metabolic glycan labelling such as the metabolic installation of 9-azidosialic acid (AzSia) on lysosomal membrane proteins. Similar to cell membrane, lysosomal membrane contains large number of proteins with highly glycosylated luminal portions. Upon uptake of the AzSia, the glycans collectively form a dense layer on the lysosome. Subsequently, acidity-promoted accumulation of optical probes was conjugated with the glycan specifically in lysosome (**Figure 8**).[32]

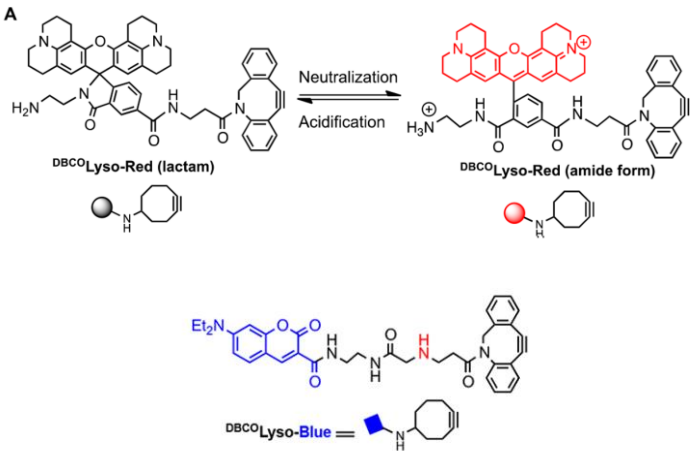

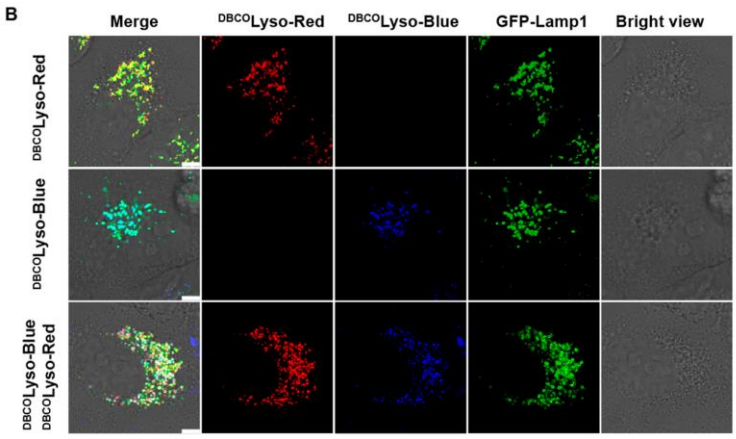

Figure 8. **A)** Acidity-triggered fluorogenic isomerization of ^{DBCO}Lyso-Red and structure of ^{DBCO}Lyso-Blue. **B)** Acidity-mediated accumulation of ^{DBCO}Lyso-Blue and ^{DBCO}Lyso-Red in lysosomes. GFP-Lamp1 was used as a mitochondria tracker (green).

Importantly, lysosomal cell death triggered by lysosomal membrane permeabilization (LMP) which commonly bypasses the caspase-dependent apoptosis pathways have become new opportunity for targeting apoptosis and drug-resistant cancers. Many small molecules that repurpose antimalaria, antihistamine, and anticancers like thioridazine, fluphenazine or toremifene are under clinical trials and are also known to accumulate in lysosomes and cause LMP. Interestingly, mix charge [+/-] nanoparticles show great selectivity in localizing in lysosome, disrupting the integrity of the membrane and eventually inducing selective cancer cell death. Generally, nanoparticles form clusters on the cell surface and are internalized through endosomes. Upon subsequent transportation into the lysosome, the low pH induces mix-charge supracrystals which result in osmotic flow induction and gradual lysosomal swelling. In contrast, normal cell can exclude the mix charge nanoparticles via exocytosis process (**Figure 9**).[33] This differentiative behavior of mix charge nanoparticles make it a great tool for precise cancer intervention.

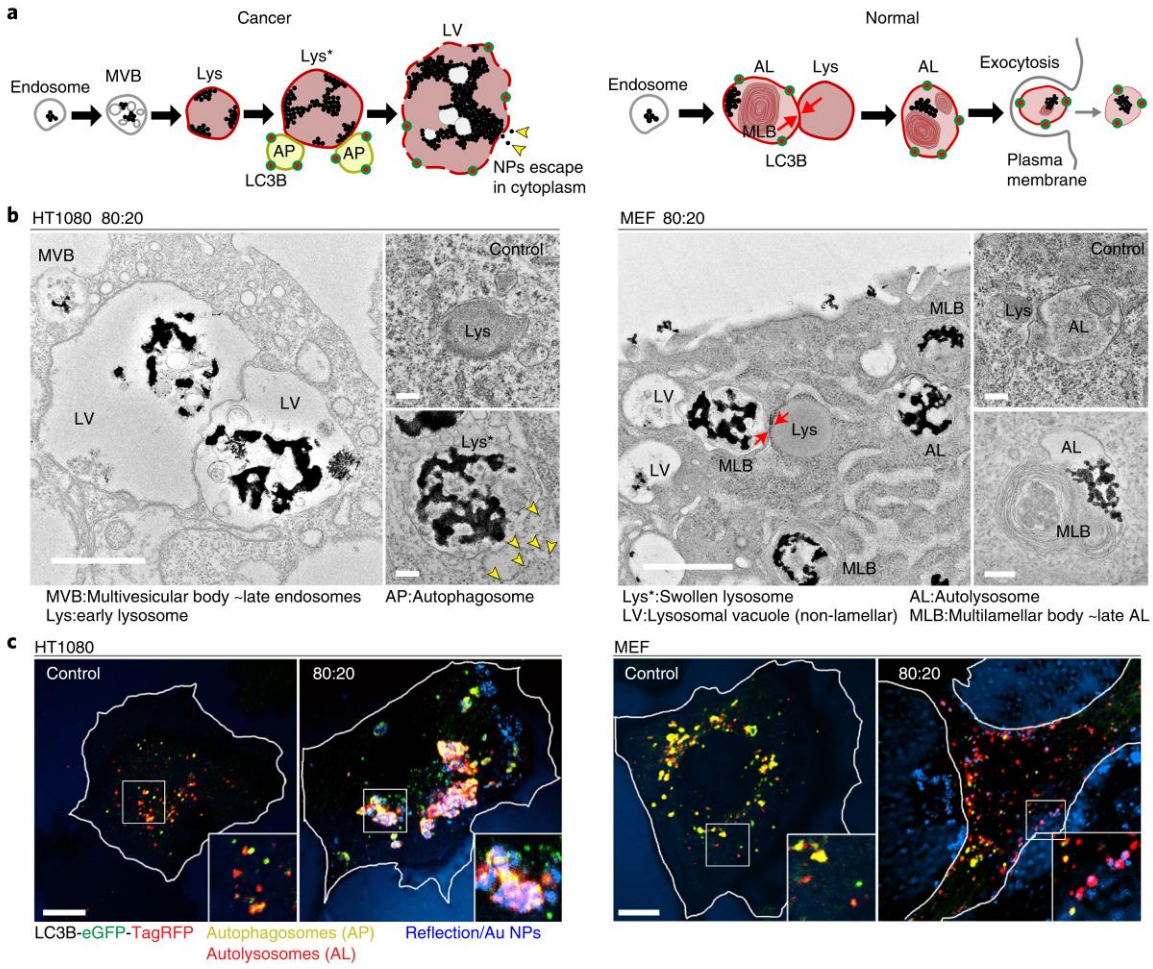

Figure 9. A) Proposed aggregation pathways for cancer (left) versus normal (right) cells. B) Representative TEM images of HT1080 (left) or MEF (right) cells treated with 80:20 NPs for 24 h. C) Merged images. APs and ALs were marked with eGFP-TagRFP-LC3B autophagy sensor, followed by cell incubation with 80:20 [+/−] NPs.

1.3. Mitochondria targeting

Mitochondria are double membrane bound organelles that contain outer membrane, intermembrane space, and a matrix. In each mitochondrion, the differing distribution of proteins, ion channels, and distinct metabolic pathways synchronically maintain the cellular homeostasis. Mitochondria dysfunction is the cause of various diseases namely cancers, metabolic disorders, neurodegenerative, and cardiovascular diseases.[34] Therefore,

development of mitochondria targeting agents to alter and treat diseases have been a popular direction in precise medicine. The most effective mitochondria localized small molecules should present lipophilic features and delocalized positive charges. Triphenylphosphonium (TPP+) lipophilic cation(s) are commonly used to recognize the mitochondria. The function is facilitated by a membrane permeable positive charge which offers highly electrostatic interaction with the negative potential across the mitochondria inner membrane (−150 to −180 mV and hyperpolarized −220 mV for cancer mitochondria). In addition, lipophilicity of the group induces significant accumulation kinetics.[35] However, this family of compound is difficult to monitor because of its nonfluorescent property. The drawback drives the development of fluorescent lipophilic dyes such as Rhodamine derivatives and Mitotrackers. Other than cationic dyes, conjugative mitochondria localization of anionic dye was recently reported with assistance from mix-charge nanoparticle platform.[36] Conventional anionic dyes such as 5-aminofluorescein without targeting specificity was loaded on the gold nanoparticles through noncovalent interaction with the mix-charge alkanethiolates. The nanoparticles functioned as a carrier to deliver the dye linked with asymmetric alkane disulfides. Upon intracellular uptake, the mix-charge NPs went through an endolysosomal process to release the loaded dye near the mitochondria, in which it conjugated with the organelle through disulfide bonds. Gradual release from the lysosome and bonding of dye to the mitochondria matrix resulted in long-term mitochondria labelling (**Figure 10**).

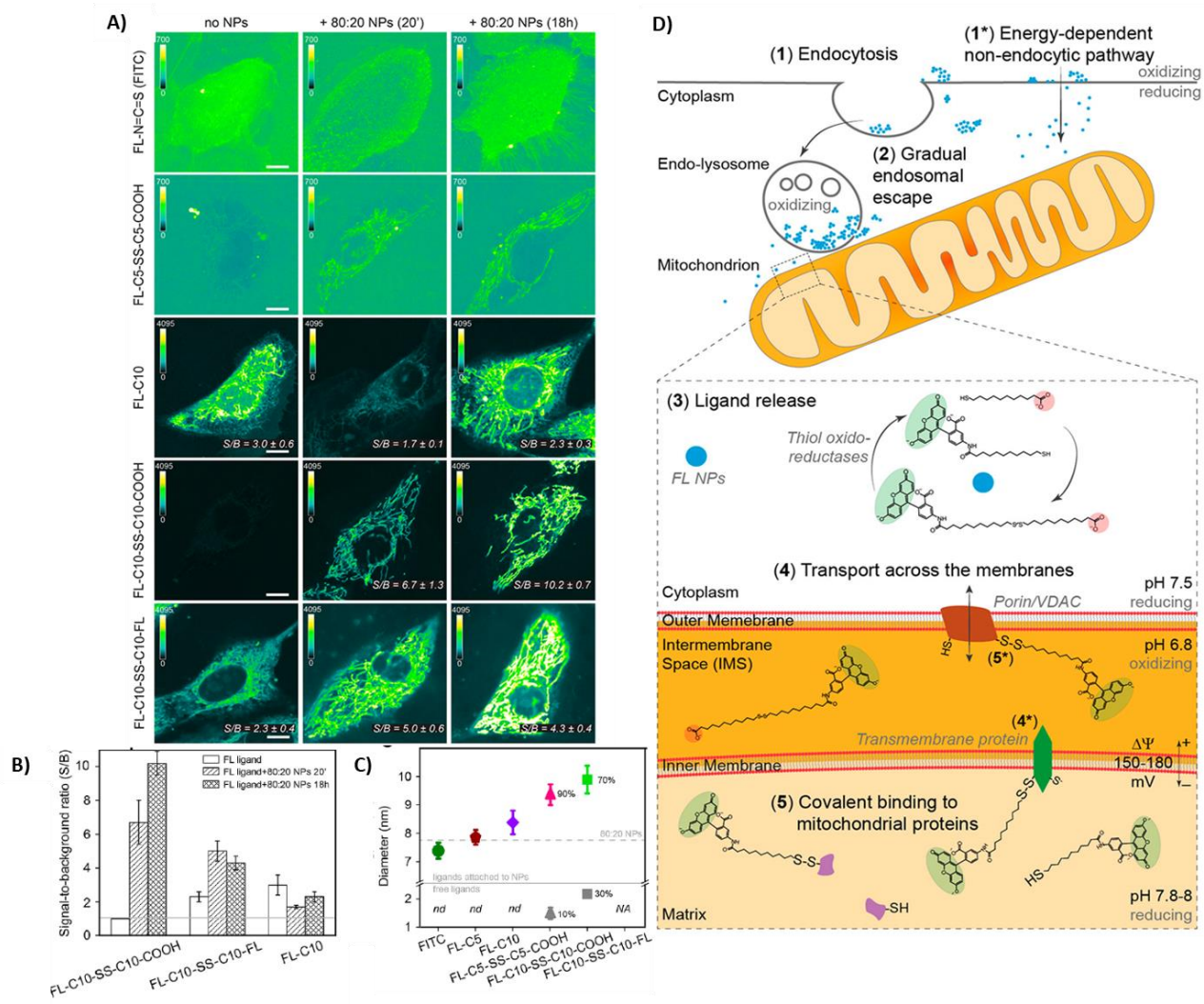

Figure 10. **A**) Confocal microscopy images of various fluorescein nanoparticle assemblies in which nM 80:20 [+/−] NPs were mixed with FL derivatives either for 20 min or 18 h in an aqueous solution. Representative images are shown without background subtraction. **B**) The signal-to-background ratios (S/B) for free fluorescein derivatives (white bars) and sequentially assembled particles. **C**) The sizes of sequentially assembled nanoparticles from fluorescence correlation spectroscopy (FCS) measurements. **D**) Proposed mechanism of mitochondrial targeting of fluorescent ligands with mixed-charge nanocarriers.

Due to its innate characteristic of being rich in oxygen, mitochondria are the most suitable organelle for photothermal dynamic therapy, in which its high concentration of oxygen can be efficiently converted to reactive oxygen species (ROS). However, due to the short lifetime and small diffusion radius, cytotoxic ROS induced by PDT needs to be generated in the vicinity of the targeted organelle or cellular compartments to be effective.

Triphenylphosphonium (TPP) was used to introduce the mitochondrial targeting function of nanoparticles. This highly lipophilic moiety was integrated into poly-(ethylene glycol) (PEG)-modified polydopamine nanoparticles (PDA-PEG) loaded with Dox for properties in overcoming drug resistance for long-term anticancer therapy.[37] These small targeting molecules were also functionalized with coumarin-based fluorescent iron oxide nanoparticles for improved cytotoxicity in Hela cells in comparison with nanoparticles without the mitochondria targeting unit. In agreement with the *in vitro* studies, 740 nm laser irradiation induced tumor suppression in tumor xenograft mouse models through mitochondria-targeted hyperthermia nanoparticles.[38] Recently, Guang et al. reported the fabrication of mitochondria targeted theranostic nanoparticles capable of imaging cancer cells for early-stage diagnostic and mitochondria-specific photothermal therapy. NIR heptamethine cyanine dye (me-IR 825) was encapsulated in the micelle-forming copolymer Pluronic F127 (PF127) to produce nanoparticles with dual channel activatable fluorescent emissions. The emitted 610 nm fluorescence was used for *in vitro* imaging of cancer mitochondria, distinguishing tumor and normal cells, accurately detecting cancer at an early stage. Meanwhile, the 845 nm fluorescence was applied for *in vivo* NIR imaging with high contrast. Furthermore, these nanoparticles exhibited impressive photothermal tumor ablation both *in vitro* and *in vivo*. These highly biocompatible and biodegradable nanoparticles are guaranteed for excellent biosafe mitochondria-targeted cancer theranostics.[39] In addition, mitochondria have similarly shown highly susceptibility to ROS. [40] In a recent study, IR 808 small molecules were anchored on manganese oxide nanoparticles (IR808@MnO NPs) for effective phototherapy of cancer. Particularly, IR808 acted as a tumor cell targeting unit which could relocate nanoparticles in the mitochondria, where MnO reacted with H_2O_2 to continuously produce oxygen (O_2). Under 808 nm laser exposure, the produced O_2 was turned into toxic $^1O_2$ and

hyperthermia was promoted. The highly effective synergistic combination therapy from this nanoplatforms is expected to broaden the application of precise cancer therapy.[41]

Most mitochondrial proteins are synthesized in cytosol before relocating to the mitochondria for functioning. This transportation is largely dependent on mitochondria precursor proteins which generate targeting signals and subsequently direct the mitochondrial protein to the mitochondria. Such precursors are characterized by homologous amino acids (such as arginine) or amphiphilic N-terminal regions. Inspired by this mechanism, dendritic lipopeptide (DLP) was modified with arginine residues to offer a nanoplatform with significant subcellular delivery. The dendritic arginine-rich architecture was designed to enhance the mitochondrial interaction of the delivery system. In addition, stearoyl group was incorporated to increase the lipophilicity. enhancing the affinity of the nanoplatforms. The study revealed a 3.5-fold increase in mitochondrial targeting compared to common TPP-based liposomes.[42]

Other components of the mitochondria also can be specific targets. One of the more promising directions would be mitochondrial DNA. Inhibitors of mitochondria transcription were developed to target human mitochondrial RNA polymerase (POLRMT) which is essential for mtDNA transcription. The small molecule showed impairment of the oxidative phosphorylation (OXPHOS) process. Allosteric binding sites of the compound were demonstrated through cryo-electron microscopy (cryo-EM) structure that the interaction is near the active central cleft of the POLRMT (**Figure 11**). Oral administration of IMT in mice effectively treated the cancer without OXPHOS dysfunction and normal cell toxicity. This study provides a promising paradigm in the physiological investigation of mitochondrial DNA.[43]

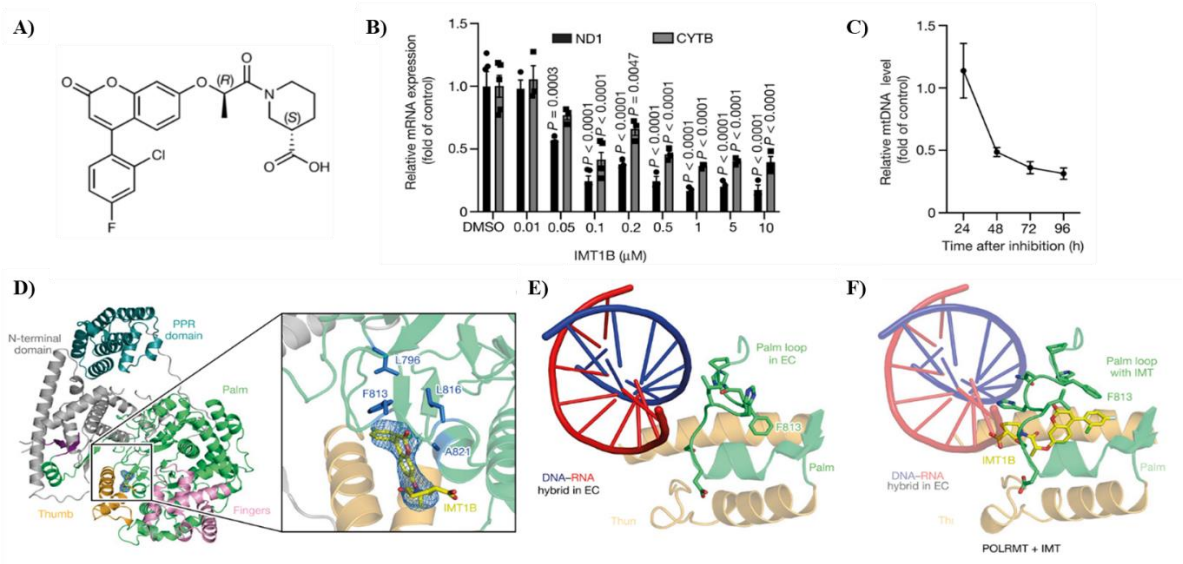

Figure 11. A) Chemical structure of IMT1B (LDC203974). **B**) Transcript levels of mitochondrial gene fragments, NADH dehydrogenase subunit 1 (ND1) and cytochrome b (CYTB), after IMT1B treatment for 6 h in HeLa cells. **C**) mtDNA levels after IMT1B treatment. **D**) Cartoon representation of the cryo-EM structure of POLRMT bound to IMT1B. **E**) Structure of the palm loop in the mitochondrial transcription elongation complex (EC). **F**) Structure of the palm loop in the presence of IMT1B.

1.4. ER and Golgi targeting modulation.

ER and Golgi apparatus gradually gained attention in modulating organelle specific therapeutic agents due to its large surface area and their important role in endocytosis. They have the largest subcellular structure in the cell, containing weakly alkaline membranes in lamellar and tubular cavities with high amount of calcium storage. When activated, the ER releases calcium ions and promotes an apoptotic program through caspase 8 initiation. Similarly, the ER also regulates the biosynthesis of protein and other macromolecules which play pivotal role in cell survival and homeostasis. Meanwhile, Golgi linked with the ER, is responsible for cell secretory pathways that label, modify and transport proteins, polysaccharides, and lipids. Interference of the Golgi integrity might result in the

dysregulation of normal cellular activities during migration, invasion and angiogenesis. Precise localization and manipulation of the ER and Golgi activity have become a new avenue in disease treatment strategies. It has been shown that some biocompatible metal complexes can be used to target ER such as Iridium (III) complex, in which they also stimulate ROS production under PDT.[44] Other than that, KKXX peptide, propylene oxide, the sulfonyl groups have also shown the ability to induce ER accumulation.[45]

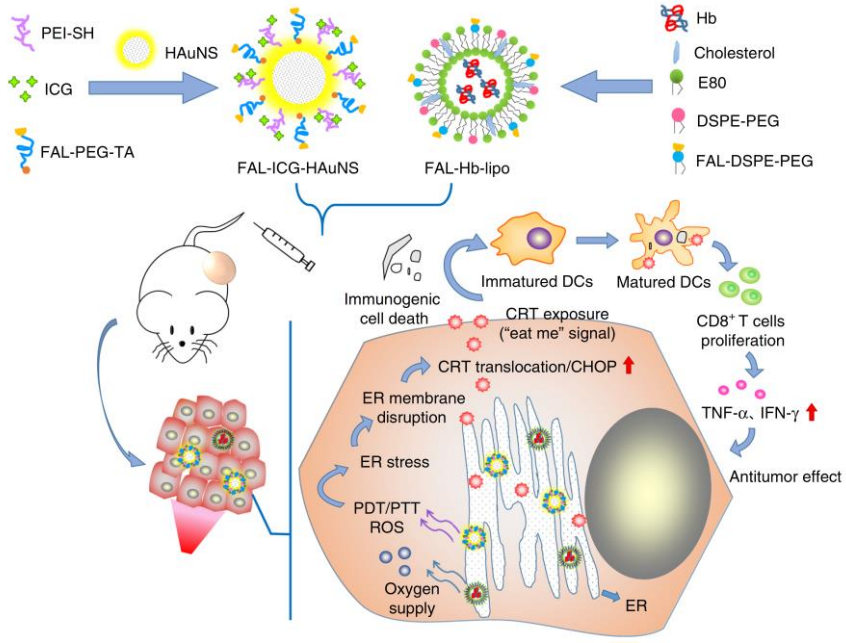

Figure 12. Schematic illustration of FAL-ICG-HAuNS plus FAL-Hb-lipo induce endoplasmic reticulum-targeting PTT/PDT therapy with enhanced immunogenic response.[46]

Interestingly, cell death-associated immunogenicity can be promoted by targeting the PDT and PTT locally in ER. Pardaxin peptides were used as ER targeting agents. ROS specifically stress the ER, causing calreticulin translocation to the cell surface which act as an "eat me" signal to stimulate the dendritic cell inducing antigen. CD8+ T cell proliferation was observed together with the cytotoxic cytokine secretion (**Figure 12**).[46]

To date, Golgi apparatus targeting design strategies still remain in its infancy. L-cysteine was reported to enable the Golgi targeting of carbon quantum dots and silica nanoparticles.[47] Meanwhile, Gong's team proved that chondroitin sulfate (CS) is a specific ligand for glycosyltransferases in the Golgi which makes them a promising candidate for further development of Golgi targeting strategies.[48]

1.5. Nucleus chemical engineering

The nucleus is the largest and stiffest organelle in most cells which contains important genetic materials and controls various cell activities including cell migration, cancer metastasis. It has been shown that governing nuclear deformability or altering the nuclear structure could further mediate cellular functions.[49] For instance, nuclear localization signal (NLS, CGGGPKKKRKVGG) peptide was conjugated to target the AuNPs to the nucleus, hence enhancing nuclear membrane stiffness and improving the inhibition effect on cell migration and invasion.[50] Notably, therapeutic agents such as Doxorubicin are not efficiently activated until they enter the nucleus.[51] This issue places the nucleus as another important subcellular target for consideration. Unfortunately, most of the chemical reagents cannot traverse the nuclear pore complex with a small pore size of around 9 to 12 nm. In order to overcome this barrier, several studies have fabricated positively charged nanoparticles to increase electrostatic interaction with the nucleus.[52] Nuclear localization sequences have been designed to target the nuclear translocation property of importin, which were then integrated with nanocarriers for its effective nuclear localization.[53] Recently, self-assembled nanoparticles (PEG-POSS-RB-NPs denoted as PPR-NPs) were introduced by conjugating multiamine-containing polyhedral oligomeric silsesquioxane (POSS) molecule with a

hydrophilic PEG chain and several hydrophobic photosensitizers such as rose bengal (RB) molecules (Figure 9D). Benefiting from the positive charge given by the amine groups on the surface, these NPs can easily enter the cell and be entrapped by lysosomes. After irradiating with light, $^1O_2$ generation caused significant lysosomal disruption, thereby releasing PPR-NPs into the cytosol. The exposed POSS molecules with polyamine property substantially directed the nanoparticles toward the nuclear membranes. This enhanced production of $^1O_2$ disintegrated the nuclear membrane, encouraging the nuclear entry of the PPR-NPs. Evidently, chemotherapeutics (10-hydroxycamptothecine and docetaxel) and nanomaterials were succesfully delivered without conventional chemical modifications.[54]

Metabolic labeling of the nucleus is one of the more promising methods for conjugation of therapeutic agents and spatially manipulating DNA functions. 5-bromo-2'-deoxyuridine (BrdU) is commonly incorporated into the DNA of dividing cells assisted by an endogenous enzyme, in which newly synthesized DNA is detected by a fluorescent antibody.[55] In general, this labelling method requires cell permeabilization and denaturation of DNA which hinders their application in live cell targeting and manipulation. In addition, antibody labelling suffers from poor tissue permeability. To overcome these hurdles, biorthogonal methods have been developed with 5-ethynyl-2'-deoxyuridine (EdU). The alkyl functional group in the EdU provides possible conjugation of azide-modified reagents and small molecules which renders immunostaining obsolete.[56] Nevertheless, EdU is generally toxic and high amount of staining may cause DNA damage and cell apoptosis. F-ara-EdU was subsequently developed to reduce the toxicity of traditional EdU.[57] However, these Cu^I-mediated azide–alkyne "click" cycloaddition (CuAAC) DNA labelling method is still limited by the usage of catalyst, which is less desirable in multidimensional pulse-chase labelling. Instead, 5-vinyl-2'-deoxyuridine (VdU) can be conjugated through a Diels–Alder (invDA) reaction between electron-deficient

tetrazines and electron-rich dienophiles without catalyst which is compatible with cell media condition.[58]

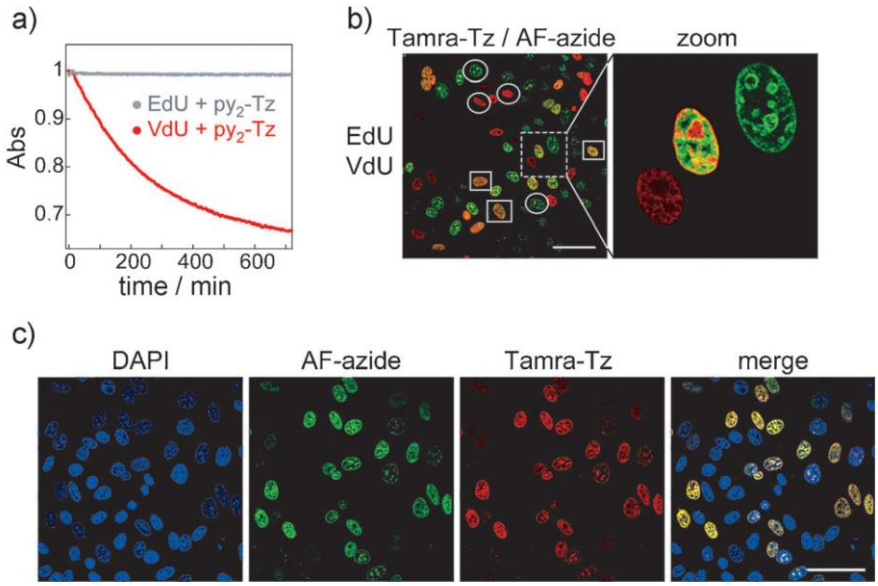

Figure 13. **A**) The consumption of tetrazine according to normalized absorbance changes at 530 nm in the presence of of EdU or VdU. **B**) Confocal fluorescence microscopy images of cells treated sequentially with EdU and VdU. **C**) Confocal fluorescence microscopy images cells treated simultaneously with a mixture of VdU and EdU. Tamra-Tz (red) and AF-azide (green). The overlay of the two color channels reveals both distinctand dual labeling, indicated by circles and squares, respectively. [58]

The conjugation kinetics are comparable to the strain-promoted azide–alkyne cycloaddition "SPAAC" reactions that are widely used for cellular labelling purposes with similar efficiency to EdU with less cytotoxicity and more specific DNA conjugation (**Figure 13**). This labelling method opens a new avenue for drug development and investigation of DNA activity. By carefully designing the targeting agents, highly precise manipulation of DNA can be achieved. For example, BODIPY-tetrazine compounds were developed to introduce photodynamic DNA damage after specific conjugation (**Figure 14**).[59]

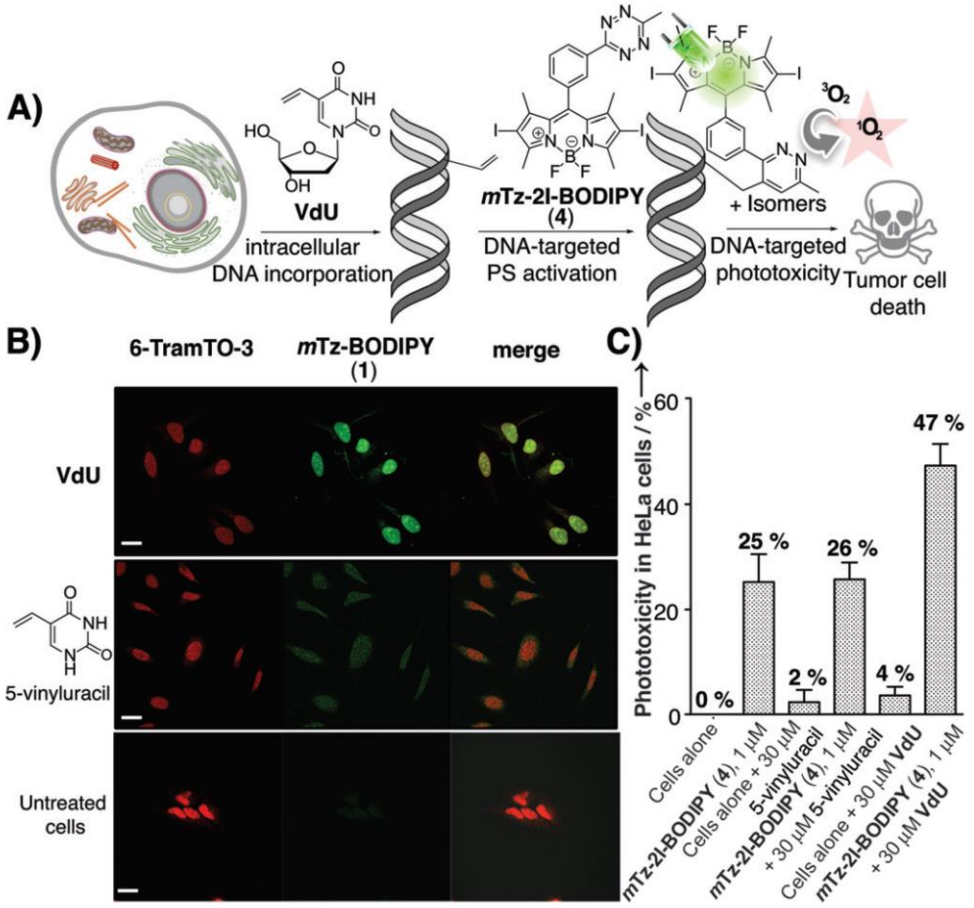

Figure 14. **A**) Schematic illustration of DNA-targeted bioorthogonal strategy for activating the phototoxicity. **B**) ligation of VdU in newly synthesized DNA upon addition of mTz-BODIPY in comparison with the non-incorporated 5-vinyluracil. **C**) Phototoxicity of mTz-2I-BODIPY (4) on HeLa cell viability treated with or without VdU/5-vinyluracil.[59]

1.6. Protein targeting

Proteins are major a class of biosystems which manipulate all the biological activities of living organisms. Therefore, structural and functional investigation of proteins are pivotal in the biological research for enhanced biopharmaceutical systems. Modification of proteins in complex biological systems with site-specificity and targeting-selectivity have become a central research area for protein science in recent years. These non-genetic targeting

strategies offer facial regulation of protein processes in living systems including protein-based biosensors, protein-protein interaction and protein enrichment or depletion.

1.6.1. Chemo-selective protein modification

Chemical and regioselective modification of proteins are one of the essential methods for attaching moieties onto the protein of interest without significant alteration of its activities. In many cases, strict control of the modification needs to be considered since small adjustment of the protein may result in significant changes to its structure integrity, rigidity as well as pharmacodynamics. Generally, chemical targeting of the proteins mainly relies on the natural amino acids in proteins to retain their biofunctions.

One of the most common targeting elements of proteins is cysteine due to its high nucleophilicity among canonical amino acids and low abundance in proteins. Simply using an appropriate electrophilic reagent such as maleimide or α-halocarbonyls can conjugate cysteines via thiol alkylation reactions. However, the linkage is unstable under high concentrations of thiol species that triggers thiol exchange reactions. Therefore, off-target release or decomposing moieties might lead to an unexpected side effect *in vivo*. Advanced organometallic methods have emerged as promising examples of stable cysteine conjugation. Particularly, Aryl palladium (II) complexes with 2−2-dicyclohexylphosphino-2′,6′-diisopropoxybiphenyl (RuPhos) ligands reacted quickly and chemo-selectively with cysteine thiol to generate high yields of conjugates.[60] Nevertheless, the transition metal-based protein modelling may suffer from insolubility and toxicity, hence would require judicious designs and purification of obtained conjugates. Notably, the nucleophilic thiol of cysteine can be converted to dehydroalanine (Dha) as an electrophilic reactive handle by oxidative or bis-alkylation-induced β-elimination of the thiolate. Site-specific protein modification with

nucleophile-tethered reagents can be obtained by a number of methods with Michael-type addition between Dha and thiol nucleophiles although high thiol-containing reagents may perturb the disulfide bonds in proteins.[61]

Lysine side chains with amine group handle is another popular target for the conjugation of proteins due to the rich chemistry available for simple and mild condition reactions. Generally, a pH of around 8 is suitable for efficient conjugation of primary amine with activated esters, sulfonyl chlorides, isocyanates, isothiocyanate, etc. Meanwhile, the high abundance of lysine groups on the protein surface needs to be taken into consideration as multiple labelling sites may interfere, such as off-target modification of highly active lysine around protein active site.[62] Computer assisted calculation and simulation can play a role in predicting the most active lysine on the protein. As such, different reaction conditions and reagents can be used to selectively manipulate the more accessible lysine compare to other nucleophilic amino acids.[63]

On the other hand, modification of aromatic amino acids in proteins is generally less common due to its lower reactivity. However, modern organic chemistry has broadened the toolbox for the selective labelling of proteins through advanced conjugations with tyrosine or tripsine, such as azo coupling of tyrosine with diazonium salts, Manich reaction with aldehyde, aniline or ene-like reaction with cyclic diazodicarboxamides, etc.[64-66] Selective targeting of tyrosine can be obtained by probe-appended boronic acid and rhodium salt inducing tyrosine side chain metalation. This method is applicable with multiple antibodies without interferences from other basic side chains as well as other aryl side chains including phenylalanine, tripsine.[67]

1.6.2. Protein tagging by ligand-directed approach.

Chemically modifying protein through its amino acid is important but the most significant approach is to selectively target the protein of interest (POI). While the underlying chemistry in amino acid reactions mainly focus on the selective site of the protein surface or pockets, ligand-assisted conjugation offers a protein selective pathway for more biological applications in which the protein is present in complex environments. Early affinity labelling methods utilized ligand-directed tosyl chemistry. Typically, after the POI is functionalized with the ligand, the phenylsulfonate (tosylate) ester group is in close proximity with other nucleophilic amino acids on the proteins which generates an SN_2 reaction to release the ligand and conjugate the labelling moiety on the protein. The main challenge of this method is its slow reaction kinetics and low labelling yields, especially for intracellular proteins.[68] Efforts in alleviating the disadvantage is to switch the cleavable reactive group for moderately reactive alkyloxyacyl imidazole, in which can be used for protein acylation, efficiently labelling the folate receptor on the cell membrane. However, these kinds of ligand-directed acyl imidazole reagents are degraded inside the cytoplasm as directed by intracellular enzymes such as esterase, proteases, etc.[69] Therefore, further advancement utilized reactive moieties that are not substrates of cellular enzymes. Dibromophenyl benzoate scaffolds were adopted to increase the steric hindrance of the substrate so that it is less susceptible to enzymatic reactions while maintaining the rapid protein labelling intracellularly.[70] In order to improve reaction kinetics, N-acyl-N-alkyl sulfonamide chemistry with comparable kinetic to those of prevalent self-labeling protein tag methods (e.g., SNAP-tag, Halo-tag) and biorthogonal reactions (e.g., IEDDA cycloadditions between tetrazines and trans-cyclooctenes). For proteins that cannot be targeted by small molecular ligands, catalyst

-mediated traceless protein labelling is a complemented alternative. For instance, affinity-guided 4-dimethylaminopyridine (DMAP) can selectively target the POI and facilitate the transfer of the acyl group from the thiophenyl ester to a nucleophilic amino acid that is in vicinity. Using this method, cell membrane proteins such as glycoprotein, endogenous HER2 and EGFR can also be labelled. Nonetheless, selective conjugation of intracellular proteins are still hindered by the insufficient biorthogonality of acyl donors and multicomponent involvement of the reactions.[71,72]

1.6.3. Activity-based protein modification.

Since the activity of a protein is tightly regulated by post-translational modification and interaction with other components inside the living cell, the tracking of its activity is vital in dissecting the biological functions of the POI. To access the functions of the POI, the most direct method is to target their active site. Activity-based probes generally contain three components, a conjugative moiety which link the active site amino acids, a spacer to reduce steric hindrance and a reporter tag for detection of protein activities. Many protein activities, especially enzymes, have been targeted real-time in living systems.[73] More importantly, this method can also be used to develop POI inhibitors. Proteins treated with the inhibitor can be blocked. Quantitative LC-MS/MS analysis in combination with activity-based conjugation generate simple and robust ways to evaluate the potential efficiency of objective inhibitors.[74]

1.6.4. Small molecular- induced protein degradation.

In order for the cell to function normally, the expression level of proteins is strictly maintained and harmonized. Minimal malfunction of proteins and their interactions may cause severe cell and tissue disorganization which can be lethal to the living system. In contrast, targeted removal, distortion or blocking of a protein plays an essential role in

investigating protein activities, drug development and treatment of multiple diseases at the cellular level. Tremendous efforts have been placed on these primary factors and marvelous achievements have been attained, including molecular inhibitors, gene silencing and editing. However, high dosage of inhibitors is normally required to generate the relevant pharmacological inhibition since efficiency is only attained with > 90% target engagement. Genetic lockdown strategies can monitor protein levels at an early stage before its expression based on antisense oligonucleotides, RNA interference, CRISPR/Cas9 and other methods. Despite its high therapeutic potential, inadequate accumulation at the targeted site with minimum side effects and metabolically unstable properties of the reagents have hindered their systematic gene knockdown applications. Therefore, chemical knockdown strategies are the gold standard for successful protein level mediation. Proteolysis targeting chimeras (PROTACs) and molecular glues are small molecule ligands with the ability to hijack natural protein homeostasis machinery, depleting the POI. Specifically, the bifunctional molecules recruit E3 ubiquitin ligase to the protein and tag the enzyme to ubiquitinate the chosen protein. The ubiquitin chains direct the proteins to the proteasome for unfolding and destruction. Such protein digestion method offers tremendous promise for future drug discovery which can tackle pathologies originating from protein that are previously considered as “undruggable” due to its inaccessibility to small-molecule intervention. PROTACs were first reported in 2001, in which the peptidic degron of hypoxia induced factor 1α is used to recruit protein to the Von Hippel Lindau factor (VHL), a component of the Cul2-Rbx1- EloB/C-VHL E3 ligase. This study is valuable in proving the machinery concept but was limited *in vivo* mainly due to the use of long peptide sequences. Smaller ligands with non-peptidic moieties were subsequently developed with different protein ligands and varied E3 ligase recruiters. For instance, small molecule nutlin was linked with

an androgen-receptor-binding group to recruit the protein to MDM2 E3 ligase.[75] Optimization of the VHL targeting moiety was also possible for *in vivo* protein knockdown (**Figure 15**).[76]

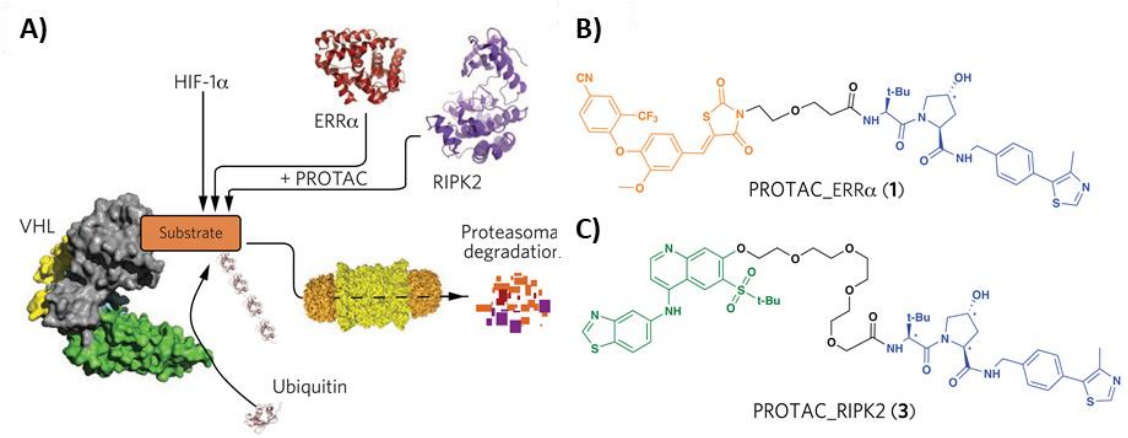

Figure 15. **A**) PROTACs recruit VHL to target proteins to induce their ubiquitination and subsequent proteasome-mediated downregulation. PROTACs were generated to two target proteins: the orphan nuclear receptor ERRa (**B**), and the protein kinase RIPK2 (**C**).[76]

"Molecular glues" are the simplest small molecules that can cause protein destabilization through simultaneously engaging the binding pockets on two separate proteins. For example, Indisulam drives the CRL4 component attachment and causes degradation of RNA Binding Motif Protein 39.[77] Thalidomide analogues including lenalidomide, pomalidomide were discovered to target cereblon (CRBN), an associated factor of DNA-damage binding protein 1 CRL4 E3 ubiquitin ligase. Rather than acting as an inhibitor, the thalidomide analogs bind to the cereblon surface and create a hotspot for protein-protein interaction, recruiting transcription factors, Ikaros and Aiolos for ubiquitination and degradation at the same time.[78,79]

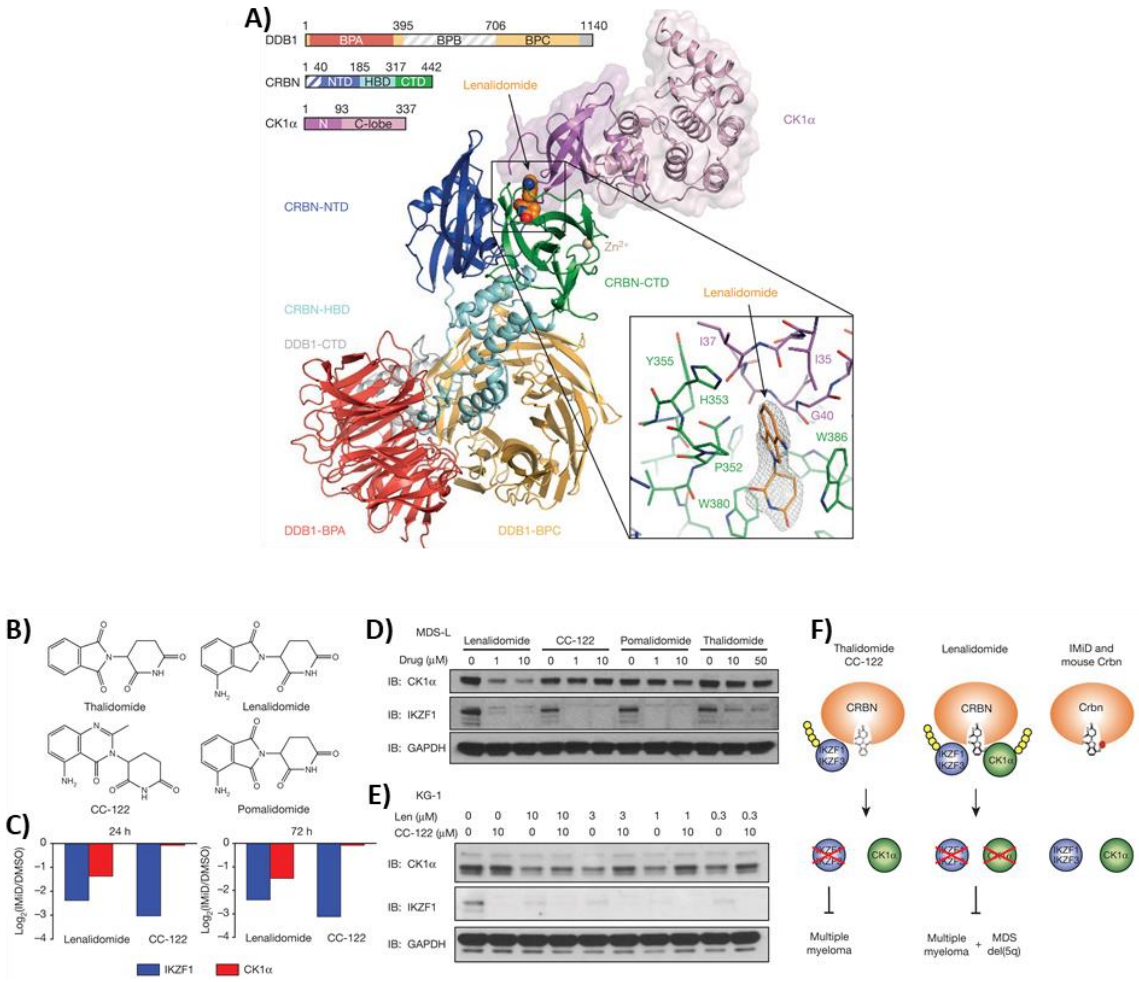

Figure 16. **A)** Overall structure of the DDB1ΔBPB–CRBN–lenalidomide–CK1α complex. [80] **B**) Structures of thalidomide, lenalidomide, pomalidomide and CC-122. **C**) Protein levels of IKZF1 and CK1a assessed by tandem mass tag quantitative proteomics. **D**) Western blot analysis of CK1a and IKZF1 protein levels in MDS-L cells treated with different analogs. **E**) KG-1 cells were treated with DMSO or lenalidomide in the absence or presence of different concentrations of CC-122. **F**) Schematic presentation of the interaction of different thalidomide analogues with CRBN, substrates, and therapeutic indications.[81]

Later studies have shown that lenalidomide itself is also a specific platform to attach casein kinase 1α (CK1α) for degradation of proteins in Myeloma, del(5q) MDS cells (**Figure 16**).[80,81] These findings opened a new avenue for the development of other simpler E3 ligase

targets in PROTACs with thalidomide analogues as CRBN recruiters. It was reported that BRD4 and FKBP12 inhibitors conjugated with pomalidomide are able to produce robust targeted protein degradation.[82] Vast number of reports subsequently demonstrated the universal applicability of this method to degrade different intracellular proteins.

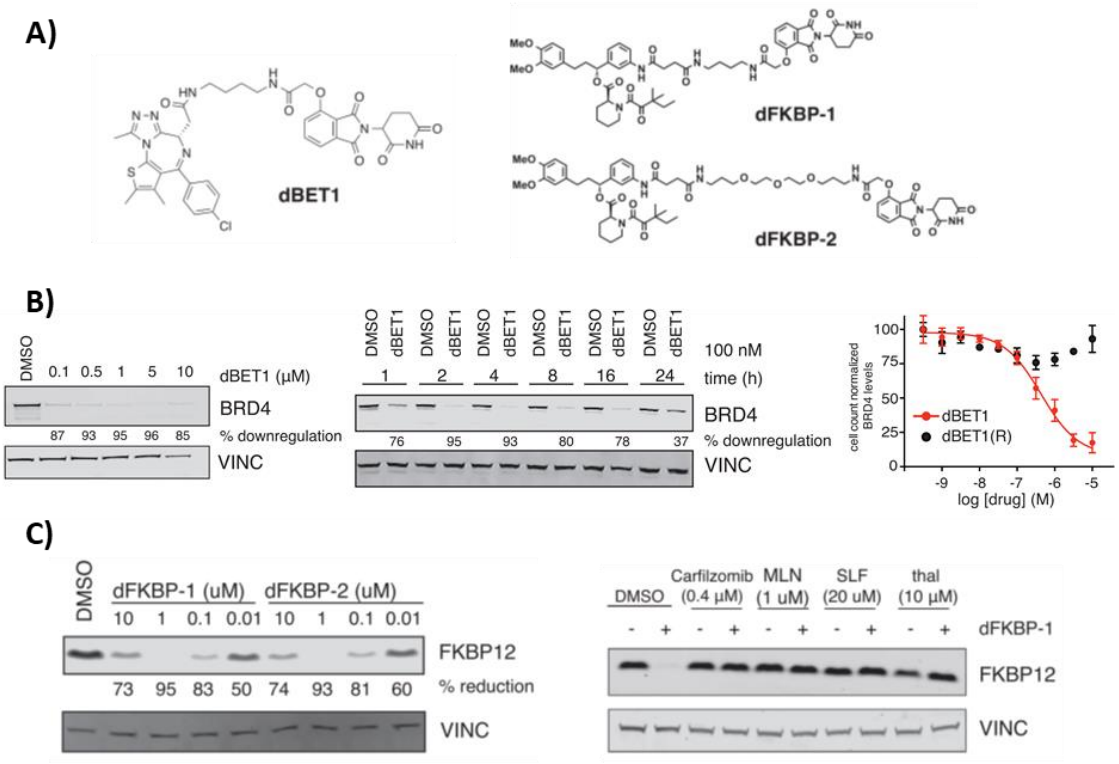

Figure 17. **A**) Chemical structure of pomalidomide conjugation with protein target ligands for as degraders of BRD4 and FKBP12. **B**) Western blot analysis of BRD4 degradation in cells treated with dBET1 in concentration and time controls and the cell viability after drug treatments. **C**) Western blot analysis of FKBP12 degradation after treatment with respective degraders and the inhibitors as controls.[82]

Extracellular or membrane proteins can be targeted and degraded by the complement method developed recently by the Bertozzi group. They reported lysosome targeting chimeras (LYTACs) that bind to both cell-surface lysosome-shutting receptor and endogenous proteins.

Agonists of the lysosome-targeting induction process are glycopeptide ligands that specifically bind to the cation-independent mannose-6-phosphate receptor (CI-M6PR). Upon linkage with the POI, the agonist activates the lysosomal degradation of the proteins via multiple enzymes and its acidic condition. This strategy showed efficient induction of lysosome-assisted degradation of apolipoprotein E4, EGFR, CD71 and PD-L1 which are all therapeutically important.[83]

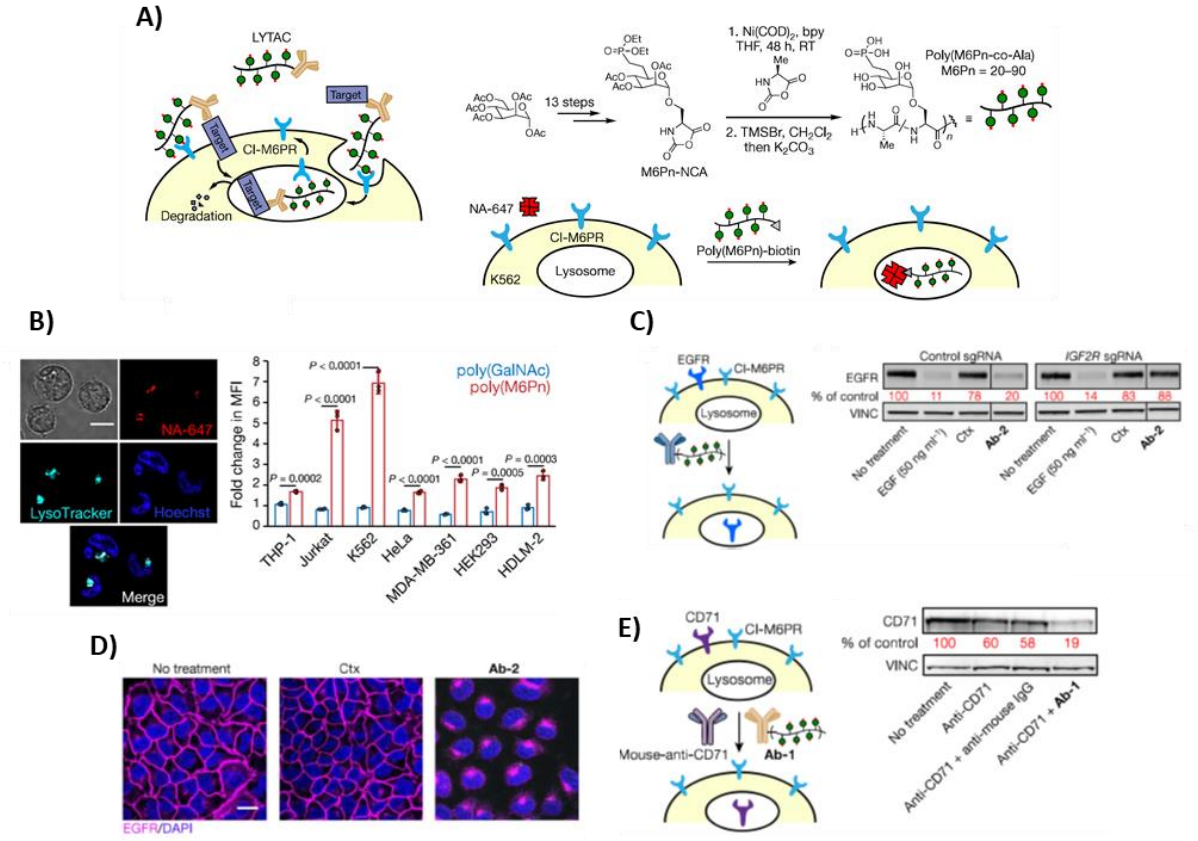

Figure 18. **A**) Lytacs recruit a glycopolupeptide ligand for CI-M6PR to drag targeted protein to lysosome. **B**) Live cell confocal image of NA-647 protein recruited to the lysosome using Lytac.Cell membrane protein such as EGFR (**C**, **D**) and CD71 (**E**) was degraded by Lytacs.[83]

Although substantial advancements have been made in the field of heterobifunctional degraders, considerable degree of skepticism about their clinical translations still exists. To

fulfil the desired physicochemical properties with the prerequisite architecture of the linked ligands, the PROTAC molecules normally deviate from the conventional “rule of five”. Complicated structures with high molecular weight substantially hindered their biophysical performances such as low cellular uptake efficiency or minimum biocompatibility with less stable metabolic characteristics. The clinical validation of this promising group of compounds is therefore still pending, especially their oral availability. Unlike molecular glues that have simultaneous binding of both POI and E3 ligase, heterobifunctional degraders perform differently in pharmacology. As the structure is separately divided into two different moieties, individual binary complexes may be saturated at high concentration, which compete with the formation of E3 ligase-substrate-ligand ternary complexes.[84] This “hook effect” complicates the investigation and drugs activity screening of each PROTAC system since concentration dependence in different compounds and cell lines need to be thoroughly investigated. “Hook effect” might also interfere *in vivo* whereby the concentration at the targeted area fluctuates due to the dosage and pharmacokinetic of each compound in a complex system. Importantly, current PROTAC molecules are mostly unable to induce specific drug targeting. Addition of affinity ligands to selected cell lines with different cellular factors may even hinder their clinical translation since it brings additional complexity to the compound. Tissue-specific degradation is therefore rendered impossible via conventional binding. Improvement of its physicochemical properties and new design considerations are still ongoing to bring back historically undruggable proteins into play for therapeutic benefits.

At present, many breakthroughs have been made in the innovation of subcellular targeting agents for specific disease diagnosis and treatment. These methods offer efficient and highly precise theragnostic results even with lower dosage of therapeutic agents. With intensive investigations on small molecules, macro biomolecules, cellular behaviors as well as the

innovation of optical and nanomaterial techniques, improvements in this area are believed to proliferate in near future for precision treatment.

In this thesis, I would like to provide general insights for the development of precision therapy. Although multiple methods have been intensively investigated for the organelle specific labeling, deeper understandings of the specific localization of the reagents are needed. Typically, subcellular targeted reagents enhanced the efficiency of the therapy with lower used dosage or milder treatment conditions. In fact, concentrating the reagents on an individual location inside the cells, which is the disease origin, can significantly enhance the precision of disease monitoring without affecting other cell functions. However, how much significant it is for the different organelle targeting is not so clear. For example, light responsive nanoparticles can be engineered to target differently into separated cell organelle, but it is not clear whether the efficiency of the photo-stimulated nanoparticles in such separated location is higher than other locations. In the chapter 2 of my thesis, such investigation for the same light treatment condition but different location of photothermal nanoparticles will be proceeded to provide insights for the importance of organelle specific consideration of photothermal nanoparticle applications. In addition, cell specific targeting of the reagents is still the utmost important factor in precision therapy, even though subcellular localization can be achieved. The combination of cell and subcellular specific targeting can ultimately provide ways for the highly accurate manipulation of the cell functions in the complex living condition. A method to provide a cell specific labelling of cell membrane will be provided in chapter 3 of the thesis. Moreover, the direction for precision therapy have been mainly basing on specific delivering of the reagents or drugs into the cell before using external stimulus for activation of the reagents, but other methods using protein-protein interactions or cell-cell interaction after subcellular localization is still limited. In chapter 4,

we will provide a proteolysis method for the depletion of a targeted protein using a small molecular inducing protein-protein integration. The method will be further extended in cell specific development in chapter 5, in which an enzyme-guided pathway provides a cell selective degradation of a specific protein in living cell. These examples in organelle localizations and its application in regulating cellular event manipulations and therapy provide further insight and new directions for the precise medicine.

1.7.References

1. Son, J.; Yi, G.; Yoo, J.; Park, C.; Koo, H.; Choi, H. S. Light-responsive nanomedicine for biophotonic imaging and targeted therapy. *Adv Drug Deliv Rev*. **2019**, *138*, 133-147.
2. Genchi, G. G.; Marino, A.; Grillone, A.; Pezzini, I.; Ciofani, G. Remote control of cellular functions: The role of smart nanomaterials in the medicine of the future. *Adv Healthc Mater*. **2017**; *6*, 1700002.
3. Peoples, J.N.; Saraf, A., Ghazal, N.; Pham, T. T.; Kwong, J. Q. Mitochondrial dysfunction and oxidative stress in heart disease. *Exp. Mol. Med.* **2019**, *51***,** 1–13.
4. Edelmann, M. J.; Maegawa, G. H. B. CNS-Targeting Therapies for Lysosomal Storage Diseases: Current Advances and Challenges. *Front. Mol. Biosci*. **2020**, 7, 559804.
5. Sundukova, M.; Prifti, E.; Bucci, A.; Kirillova, K.; Serrao, J.; Reymond, L.; Umebayashi, M.; Hovius, R.; Riezman, H.; Johnsson, K.; Heppenstall, P. A. A Chemogenetic Approach for the Optical Monitoring of Voltage in Neurons. *Angew. Chem. Int. Ed. Engl*. **2019**, 58, 2341-2344.
6. Mu, J.; Liu, F.; Rajab, M. S.; Shi, M.; Li, S.; Goh, C.; Lu, L.; Xu, Q. H.; Liu, B.; Ng, L. G.; Xing, B. G. A small-molecule FRET reporter for the real-time visualization of cell-

surface proteolytic enzyme functions. *Angew. Chem. Int. Ed. Engl*. **2014**, *53*, 14357-14362.

7. Todhunter, M. E.; Jee, N. Y.; Hughes, A. J.; Coyle, M. C.; Cerchiari, A.; Farlow, J.; Garbe, J. C.; LaBarge, M. A.; Desai, T. A.; Gartner, Z. J. Programmed synthesis of three-dimensional tissues Programmed synthesis of three-dimensional tissues. *Nat. Methods* **2015**, *12*, 975–981.
8. Qiu, L.; Zhang, T.; Jiang, J.; Wu, C.; Zhu, G.; You, M.; Chen, X.; Zhang, L.; Cui, C.; Yu, R.; Tan, W. Cell membrane-anchored biosensors for real-time monitoring of the cellular microenvironment. *J. Am. Chem. Soc.* **2014**, *136*, 13090-13093.
9. Csizmar, C. M.; Petersburg, J. R.; Hendricks, A.; Stern, L. A.; Hackel, B. J.; Wagner, C. R. Engineering Reversible Cell-Cell Interactions with Lipid Anchored Prosthetic Receptors. *Bioconjug. Chem*. **2018**, *29*, 1291-1301.
10. Takeo, M.; Li, C.; Matsuda, M.; Nagai, H.; Hatanaka, W.; Yamamoto, T.; Kishimura, A.; Mori, T.; Katayama, Y. Optimum design of amphiphilic polymers bearing hydrophobic groups for both cell surface ligand presentation and intercellular cross-linking. *J Biomater Sci Polym Ed*. **2015**, *26*, 353-368.
11. Koyfman, A. Y.; Braun, G. B.; Reich, N. O. Cell-targeted self-assembled DNA nanostructures. *J. Am. Chem. Soc.* **2009**, *131*, 14237-14239.
12. Gong, P.; Zheng, W.; Huang, Z.; Zhang, W.; Xiao, D.; Jiang, X. A Strategy for the Construction of Controlled, Three-Dimensional, Multilayered, Tissue-Like Structures. *Adv. Funct. Mater.* **2013**, *23*, 42-46.
13. Cheng, H.; Byrska-Bishop, M.; Zhang, C. T.; Kastrup, C. J.; Hwang, N. S.; Tai, A. K.; Lee, W. W.; Xu, X.; Nahrendorf, M.; Langer, R.; Anderson, D. G.; Stem cell

membrane engineering for cell rolling using peptide conjugation and tuning of cell-selectin interaction kinetics. *Biomaterials* **2012**, *33*, 5004-50012.

14. Amaral, A. J. R.; Pasparakis, G. Macromolecular cell surface engineering for accelerated and reversible cellular aggregation. *Chem. Commun.* **2015**, *51*, 17556–17559.
15. Fiala, T.; Wang, J.; Dunn, M.; Šebej, P.; Choi, S. J.; Nwadibia, E. C.; Fialova, E.; Martinez, D. M.; Cheetham, C. E.; Fogle, K. J.; Palladino, M. J.; Freyberg, Z.; Sulzer, D.; Sames, D. Chemical Targeting of Voltage Sensitive Dyes to Specific Cells and Molecules in the Brain. *J. Am. Chem. Soc.* **2020**, *142*, 9285-9301.
16. Tong, L.; Zhao, Y.; Huff, T. B.; Hansen, M. N.; Wei, A.; Cheng, J. X. Gold Nanorods Mediate Tumor Cell Death by Compromising Membrane Integrity. *Adv. Mater.* **2007**, *19*, 3136-3141.
17. Komatsu, T.; Kyo, E.; Ishii, H.; Tsuchikama, K.; Yamaguchi, A.; Ueno, T.; Hanaoka, K.; Urano, Y. Antibody Clicking as a Strategy to Modify Antibody Functionalities on the Surface of Targeted Cells. *J. Am. Chem. Soc.* **2020**, *142*, 15644-15648.
18. O'Brien, P. J.; Luo, W.; Rogozhnikov, D.; Chen, J.; Yousaf, M. N. Spheroid and Tissue Assembly via Click Chemistry in Microfluidic Flow. *Bioconjug. Chem.* **2015**, *26*, 1939-1949.
19. Rogozhnikov, D.; O'Brien, P.J.; Elahipanah, S.; Yousaf, M.N. Scaffold free bio-orthogonal assembly of 3-dimensional cardiac tissue via cell surface engineering. *Sci. Rep.* **2016**, *6*, 39806.
20. Sarkar, D.; Vemula, P.K.; Zhao, W.; Gupta, A.; Karnik, R.; Karp, J.M. Engineered mesenchymal stem cells with self-assembled vesicles for systemic cell targeting. *Biomaterials* **2010**, *31*, 5266–5274.

21. Kim, H.; Lee, J.; Oh, C.; Park, J. H. Cooperative tumour cell membrane targeted phototherapy. *Nat. Commun*. **2017**, 8, 15880.
22. Agatemor, C.; Buettner, M. J.; Ariss, R.; Muthiah, K.; Saeui, C. T.; Yarema, K. J. Exploiting metabolic glycoengineering to advance healthcare. *Nat. Rev. Chem*. **2019**, *3*, 605-620.
23. Wang, H.; Mooney, D. J. Metabolic glycan labelling for cancer-targeted therapy. *Nat. Chem.* **2020**,*12*, 1102-1114.
24. Pedowitz, N. J.; Pratt, M. R. Design and synthesis of metabolic chemical reporters for the visualization and identification of glycoproteins, *RSC Chem. Biol.* **2021**, *2*, 306-321.
25. Li, J.; Chen, M.; Liu, Z.; Zhang, L.; Felding, B. H.; Moremen, K. W.; Lauvau, G.; Abadier, M.; Ley, K.; Wu, P. A Single-Step Chemoenzymatic Reaction for the Construction of Antibody-Cell Conjugates. *ACS Cent. Sci*. **2018**, *4*, 1633-1641.
26. Li, S.; Yu, B.; Wang, J.; Zheng, Y.; Zhang, H.; Walker, M. J.; Yuan, Z.; Zhu, H.; Zhang, J.; Wang, P. G.; Wang, B. Biomarker-Based Metabolic Labeling for Redirected and Enhanced Immune Response. *ACS Chem. Biol*. **2018**, *13*, 1686-1694.
27. Wang, H.; Sobral, M. C.; Zhang, D. K. Y.; Cartwright, A. N.; Li, A. W.; Dellacherie, M. O.; Tringides, C. M.; Koshy, S. T.; Wucherpfennig, K. W.; Mooney, D. J. Metabolic labelling, and targeted modulation of dendritic cells. *Nat. Mater*. **2020**, *19*, 1244-1252.
28. Swee, L. K.; Lourido, S.; Bell, G. W.; Ingram, J. R.; Ploegh, H. L. One-step enzymatic modification of the cell surface redirects cellular cytotoxicity and parasite tropism. *ACS Chem. Biol.* **2015**, *10*, 460-465.
29. Mahmoodi, M. M.; Abate-Pella, D.; Pundsack, T. J.; Palsuledesai, C. C.; Goff, P. C.; Blank, D. A.; Distefano, M. D. Nitrodibenzofuran: A One- and Two-Photon Sensitive

Protecting Group That Is Superior to Brominated Hydroxycoumarin for Thiol Caging in Peptides. *J. Am. Chem. Soc*. **2016**, *138*, 5848-5859.

30. Zhang, Z.; Yue, P.; Lu, T.; Wang, Y.; Wei, Y.; Wei, X. Role of lysosomes in physiological activities, diseases, and therapy. *J. Hematol. Oncol*. **2021**, *14*, 79.
31. Bonam, S. R.; Wang, F.; Muller, S. Lysosomes as a therapeutic target. *Nat. Rev. Drug. Discov.* **2019**, *18*, 923–948.
32. Zhang, E.; Shi, Y.; Han, J.; Han, S. Organelle-Directed Metabolic Glycan Labeling and Optical Tracking of Dysfunctional Lysosomes Thereof. *Anal. Chem.* **2020**, *92*, 15059-15068.
33. Borkowska, M.; Siek, M.; Kolygina, D. V.; Sobolev, Y. I.; Lach, S.; Kumar, S.; Cho, Y. K.; Kandere-Grzybowska, K.; Grzybowski, B. A. Targeted crystallization of mixed-charge nanoparticles in lysosomes induces selective death of cancer cells. *Nat. Nanotechnol.* **2020**, *15*, 331-341.
34. Suomalainen, A.; Battersby, B. J.; Mitochondrial diseases: the contribution of organelle stress responses to pathology. *Nat. Rev. Mol. Cell. Biol*. **2018**, *19*, 77-92.
35. Zielonka, J.; Joseph, J.; Sikora, A.; Hardy, M.; Ouari, O.; Vasquez-Vivar, J.; Cheng, G.; Lopez, M.; Kalyanaraman, B. Mitochondria-Targeted Triphenylphosphonium-Based Compounds: Syntheses, Mechanisms of Action, and Therapeutic and Diagnostic Applications. *Chem. Rev*. **2017**, *117*, 10043-10120.
36. Kolygina, D. V.; Siek, M.; Borkowska, M.; Ahumada, G.; Barski, P.; Witt, D.; Jee, A. Y.; Miao, H.; Ahumada, J. C.; Granick, S.; Kandere-Grzybowska, K.; Grzybowski, B. A. Mixed-Charge Nanocarriers Allow for Selective Targeting of Mitochondria by Otherwise Nonselective Dyes. *ACS Nano* **2021**.

37. Li, W. Q.; Wang, Z.; Hao, S.; He, H.; Wan, Y.; Zhu, C.; Sun, L. P.; Cheng, G.; Zheng, S. Y. Mitochondria-Targeting Polydopamine Nanoparticles to Deliver Doxorubicin for Overcoming Drug Resistance. *ACS Appl. Mater. Interfaces*. **2017**, *9*, 16793-16802.
38. Jung, H. S.; Han, J.; Lee, J. H.; Lee, J. H.; Choi, J. M.; Kweon, H. S.; Han, J. H.; Kim, J. H.; Byun, K. M.; Jung, J. H.; Kang, C.; Kim, J. S. Enhanced NIR radiation-triggered hyperthermia by mitochondrial targeting. *J. Am. Chem. Soc*. **2015**, *137*, 3017-3023.
39. Guang, Y. P.; Jia, H.; Zhu, Y. X.; Sun, W.; Cheng, X.; Wu, F. G. Cyanine-containing polymeric nanoparticles with imaging/therapy-switchable capability for mitochondria-targeted cancer theranostics. *ACS Appl. Nano. Mater*. **2018**, *1*, 2885-2897.
40. Bae, S. K.; Heo, C. H.; Choi, D. J.; Sen, D.; Joe, E. H.; Cho, B. R.; Kim, H. M. A ratiometric two-photon fluorescent probe reveals reduction in mitochondrial H2S production in Parkinson's disease gene knockout astrocytes. *J. Am. Chem. Soc*. **2013**; *135*, 9915-9923.
41. Zhou, L.; Wu, Y.; Meng, X.; Li, S.; Zhang, J.; Gong, P.; Zhang, P.; Jiang, T.; Deng, G.; Li, W.; Sun, Z.; Cai, L. Dye-anchored MnO nanoparticles targeting tumor and inducing enhanced phototherapy effect via mitochondria-mediated pathway. *Small* **2018**, *14*, e1801008.
42. Jiang, L.; Zhoum, S.; Zhang, X.; Li, C.; Ji, S.; Mao, H.; Jiang, X. Mitochondrion-specific dendritic lipopeptide liposomes for targeted sub-cellular delivery. *Nat. Commun*. **2021**, *12*, 2390.
43. Bonekamp, N. A.; Peter, B.; Hillen, H. S.; Felser, A.; Bergbrede, T.; Choidas, A.; Horn, M.; Unger, A.; Di Lucrezia, R.; Atanassov, I.; Li, X.; Koch, U.; Menninger, S.; Boros, J.; Habenberger, P.; Giavalisco, P.; Cramer, P.; Denzel, M. S.; Nussbaumer, P.;

Klebl, B.; Falkenberg, M.; Gustafsson, C. M.; Larsson, N. G. Small-molecule inhibitors of human mitochondrial DNA transcription. *Nature* **2020**, *588*, 712-716.

44. Nam, J. S.; Kang, M. G.; Kang, J.; Park, S. Y.; Lee, S. J.; Kim, H. T.; Seo, J. K.; Kwon, O. H.; Lim, M. H.; Rhee, H. W.; Kwon, T. H. Endoplasmic reticulum-localized Iridium(III) complexes as efficient photodynamic therapy agents via protein modifications. *J. Am. Chem. Soc*. **2016**, *138*, 10968–10977.
45. Feng, Z.; Wang, H.; Wang, S.; Zhang, Q.; Zhang, X.; Rodal, A. A.; Xu, B. Enzymatic assemblies disrupt the membrane and target endoplasmic reticulum for selective cancer cell death. *J. Am. Chem. Soc*. **2018**, *140*, 9566–9573.
46. Li, W.; Yang, J.; Luo, L.; Jiang, M.; Qin, B.; Yin, H.; Zhu, C.; Yuan, X.; Zhang, J.; Luo, Z.; Du, Y.; Li, Q.; Lou, Y.; Qiu, Y.; You, J. Targeting photodynamic and photothermal therapy to the endoplasmic reticulum enhances immunogenic cancer cell death. *Nat. Commun.* **2019**, *10*, 3349.
47. Li, R. S.; Gao, P. F.; Zhang, H. Z.; Zheng, L. L.; Li, C. M.; Wang, J.; Li, Y. F.; Liu, F.; Li, N.; Huang, C. Z. Chiral nanoprobes for targeting and long-term imaging of the Golgi apparatus. *Chem. Sci*. **2017**, *8*, 6829–6835.
48. Luo, J.; Zhang, P.; Zhao, T.; Jia, M.; Yin, P.; Li, W.; Zhang, Z. R.; Fu, Y.; Gong, T. Golgi apparatus-targeted chondroitin-modified nanomicelles suppress hepatic stellate cell activation for the management of liver fibrosis. *ACS Nano* **2019**, *13*, 3910–3923.
49. Kirby, T. J.; Lammerding, J. Emerging views of the nucleus as a cellular mechanosensor. *Nat. Cell. Biol*. **2018**; *20*, 373-381.

50. Ali, M. R. K.; Wu, Y.; Ghosh, D.; Do, B. H.; Chen, K.; Dawson, M. R.; Fang, N.; Sulchek, T. A.; El-Sayed, M. A. Nuclear Membrane-Targeted Gold Nanoparticles Inhibit Cancer Cell Migration and Invasion. *ACS Nano*. **2017**, *11*, 3716-3726.
51. Lin, X.; Li, Q.; Wang, Y. J.; Ju, Y. W.; Chi, Z. Q.; Wang, M. W.; Liu, J. G. Morphine inhibits doxorubicin-induced reactive oxygen species generation and nuclear factor kappaB transcriptional activation in neuroblastoma SH-SY5Y cells. *Biochem. J.* **2007**, *406*, 215-221.
52. Xu, P.; Van, K. E. A.; Zhan, Y.; Murdoch, W. J.; Radosz, M.; Shen, Y. Targeted charge-reversal nanoparticles for nuclear drug delivery. *Angew. Chem. Int. Ed*. **2007**, *46*, 4999-5002.
53. Han, K.; Zhang, W. Y.; Zhang, J.; Lei, Q.; Wang, S. B.; Liu, J. W.; Zhang, X. Z.; Han, H. Y. Acidity-triggered tumor-targeted chimeric peptide for enhanced intra-nuclear photodynamic therapy. *Adv. Funct. Mater*. **2016**, *26*, 4351-4361.
54. Zhu, Y. X.; Jia, H. R.; Pan, G. Y.; Ulrich, N. W.; Chen, Z.; Wu, F. G. Development of a light-controlled nanoplatform for direct nuclear delivery of molecular and nanoscale materials. *J. Am. Chem. Soc.* **2018**, *140*, 4062-4070.
55. Mühlmann-Díaz, M. C.; Dullea, R. G.; Bedford, J. S. Application of 5-bromo-2'deoxyuridine as a label for in situ hybridization in chromosome microdissection and painting, and 3' OH DNA end labeling for apoptosis. *Biotechniques* **1996**, *21*, 82-86.
56. Salic, A.; Mitchison, T. J. A chemical method for fast and sensitive detection of DNA synthesis in vivo. *Proc. Natl. Acad. Sci. U S A.* **2008**, *108*, 2415-2420.
57. Neef, A. B.; Luedtke, N. W. Dynamic metabolic labeling of DNA in vivo with arabinosyl nucleosides. *Proc. Natl. Acad. Sci. U S A.* **2011**, *108*, 20404-20409.

58. Rieder, U.; Luedtke, N. W. Alkene-tetrazine ligation for imaging cellular DNA. *Angew. Chem. Int. Ed. Engl.* **2014**, *53*, 9168-9172.

59. Linden, G.; Zhang, L.; Pieck, F.; Linne, U.; Kosenkov, D.; Tonner, R.; Vázquez, O. Conditional Singlet Oxygen Generation through a Bioorthogonal DNA-targeted Tetrazine Reaction. *Angew. Chem. Int. Ed. Engl*. **2019**, *58*, 12868-12873.

60. Vinogradova, E.; Zhang, C.; Spokoyny, A.; Pentelute, B.; Buchwald, S. Organometallic palladium reagents for cysteine bioconjugation. *Nature* **2015**, *526*, 687–691.

61. Dadová, J.; Galan, S. R.; Davis, B. G. Synthesis of modified proteins via functionalization of dehydroalanine. *Curr. Opin. Chem. Biol*. **2018**, *46*, 71-81.

62. Nanna, A.R.; Li, X.; Walseng, E.; Pedzisa, L.; Goydel, R. S.; Hymel, D.; Burke Jr., T. R.; Roush, W. R.; Rader, C. Harnessing a Catalytic Lysine Residue for the One-Step Preparation of Homogeneous Antibody-Drug Conjugates. *Nat. Commun.* ***2017****, 8,* 1112.

63. Matos, M. J.; Oliveira, B. L.; Martínez-Sáez, N.; Guerreiro, A.; Cal, P. M. S. D.; Bertoldo, J.; Maneiro, M.; Perkins, E.; Howard, J.; Deery, M. J.; Chalker, J. M.; Corzana, F.; Jiménez-Osés, G.; Bernardes, G. J. L. Chemo- and Regioselective Lysine Modification on Native Proteins. *J. Am. Chem. Soc.* **2018,** *140*, 4004-4017.

64. Hooker, J. M.; Kovacs, E. W.; Francis, M. B. Interior surface modification of bacteriophage MS2. *J. Am. Chem. Soc.* **2004**, *126*, 3718-3719.

65. Joshi, N. S.; Whitaker, L. R.; Francis, M. B. A three-component Mannich-type reaction for selective tyrosine bioconjugation. *J. Am. Chem. Soc.* **2004**, *126*, 15942-15943.

66. Ban, H.; Gavrilyuk, J.; Barbas, C. F. Tyrosine bioconjugation through aqueous ene-type reactions: a click-like reaction for tyrosine. *J. Am. Chem. Soc*. **2010**, *132*, 1523-1525.

67. Ohata, J.; Miller, M. K.; Mountain, C. M.; Vohidov, F.; Ball, Z. T. A Three-Component Organometallic Tyrosine Bioconjugation. *Angew. Chem. Int. Ed. Engl*. **2018**, *57*, 2827-2830.

68. Tamura, T.; Tsukiji, S.; Hamachi, I. Native FKBP12 engineering by ligand-directed tosyl chemistry: labeling properties and application to photo-cross-linking of protein complexes in vitro and in living cells. *J. Am. Chem. Soc*. **2012**, *134*, 2216-2226.

69. Fujishima, S. H.; Yasui, R.; Miki, T.; Ojida, A.; Hamachi, I. Ligand- Directed Acyl Imidazole Chemistry for Labelling of Membrane-Bound Proteins on Live Cells. *J. Am. Chem. Soc*. **2012**, *134*, 3961-3964.

70. Matsuo, K.; Nishikawa, Y.; Masuda, M.; Hamachi, I. Live-Cell Protein Sulfonylation Based on Proximity-driven N-Sulfonyl Pyridone Chemistry. *Angew. Chem., Int. Ed*. **2018**, *57*, 659-662.

71. Hayashi, T.; Sun, Y.; Tamura, T.; Kuwata, K.; Song, Z.; Takaoka, Y.; Hamachi, I. Semisynthetic Lectin-4-Dimethylaminopyridine Conjugates for Labeling and Profiling Glycoproteins on Live Cell Surfaces. *J. Am. Chem. Soc*. **2013**, *135*, 12252-12258.

72. Hayashi, T.; Yasueda, Y.; Tamura, T.; Takaoka, Y.; Hamachi, I. Analysis of Cell-Surface Receptor Dynamics through Covalent Labeling by Catalyst-Tethered Antibody. *J. Am. Chem. Soc.* **2015**, *137*, 5372-5380.

73. Cravatt, B. F.; Wright, A. T.; Kozarich, J. W. Activity-based protein profiling: from enzyme chemistry to proteomic chemistry. *Annu. Rev. Biochem*. **2008**, *77*, 383-414.

74. Lanning, B. R.; Whitby, L. R.; Dix, M. M.; Douhan, J.; Gilbert, A. M.l; Hett, E. C.; Johnson, T. O.; Joslyn, C.; Kath, J. C.; Niessen, S.; Roberts, L. R.; Schnute, M. E.; Wang, C.; Hulce, J. J.; Wei, B.; Whiteley, L. O.; Hayward, M. M.; Cravatt, B. F. A road map to evaluate the proteome-wide selectivity of covalent kinase inhibitors. *Nat. Chem. Biol*. **2014**, *10*, 760-767.

75. Sakamoto, K. M.; Kim, K. B.; Kumagai, A.; Mercurio, F.; Crews, C. M.; Deshaies, R. J. Protacs: chimeric molecules that target proteins to the Skp1-Cullin-F box complex for ubiquitination and degradation. *Proc. Natl. Acad. Sci. USA*. **2001**, *98*, 8554-8559.

76. Bondeson, D. P.; Mares, A.; Smith, I. E.; Ko, E.; Campos, S.; Miah, A. H.; Mulholland, K. E.; Routly, N.; Buckley, D. L.; Gustafson, J. L.; Zinn, N.; Grandi, P.; Shimamura, S.; Bergamini, G.; Faelth-Savitski, M.; Bantscheff, M.; Cox, C.; Gordon, D. A.; Willard, R. R.; Flanagan, J. J.; Casillas, L. N.; Votta, B. J.; den Besten, W.; Famm, K.; Kruidenier, L.; Carter, P. S.; Harling, J. D.; Churcher, I.; Crews, C. M. Catalytic in vivo protein knockdown by small-molecule PROTACs. *Nat. Chem. Biol.* **2015,** *11*, 611–617.

77. Han, T.; Goralski, M.; Gaskill, N.; Capota, E.; Kim, J.; Ting, T. C.; Xie, Y.; Williams, N. S.; Nijhawan, D. Anticancer sulfonamides target splicing by inducing RBM39 degradation via recruitment to DCAF15. *Science.* **2017**, *356*, eaal3755.

78. Krönke, J.; Udeshi, N. D.; Narla, A.; Grauman, P.; Hurst, S. N.; McConkey, M.; Svinkina, T.; Heckl, D.; Comer, E.; Li, X.; Ciarlo, C.; Hartman, E.; Munshi, N.; Schenone, M.; Schreiber, S. L.; Carr, S. A.; Ebert, B. L. Lenalidomide causes selective degradation of IKZF1 and IKZF3 in multiple myeloma cells. *Science* **2014**, *343*, 301–305.

79. Lu, G.; Middleton, R. E.; Sun, H.; Naniong, M.; Ott, C. J.; Mitsiades, C. S.; Wong, K. K.; Bradner, J. E.; Kaelin, W. G. Jr. The myeloma drug lenalidomide promotes the cereblondependent destruction of Ikaros proteins. *Science* **2014**, *343*, 305–309.

80. Petzold, G.; Fischer, E. S.; Thomä, N. H. Structural basis of lenalidomide-induced CK1α degradation by the CRL4(CRBN) ubiquitin ligase. *Nature*. **2016**, 532, 127-130.

81. Krönke, J.; Fink, E. C.; Hollenbach, P. W.; MacBeth, K. J.; Hurst, S. N.; Udeshi, N. D.; Chamberlain, P. P.; Mani, D. R.; Man, H. W.; Gandhi, A. K.; Svinkina, T.; Schneider, R. K.; McConkey, M.; Järås, M.; Griffiths, E.; Wetzler, M.; Bullinger, L.; Cathers, B. E.; Carr, S. A.; Chopra, R.; Ebert, B. L. Lenalidomide induces ubiquitination and degradation of CK1α in del(5q) MDS. *Nature* **2015**, *523*, 183-188.

82. Winter, G. E.; Buckley, D. L.; Paulk, J.; Roberts, J. M.; Souza, A.; Dhe-Paganon, S.; Bradner, J. E. Phthalimide conjugation as a strategy for in vivo target protein degradation. *Science* **2015**, *348*,1376-1381.

83. Banik, S. M.; Pedram, K.; Wisnovsky, S.; Ahn, G.; Riley, N. M.; Bertozzi, C. R. Lysosome targeting chimeras for degradation of extracellular proteins. *Nature* **2020**, *584*, 291-297.

84. Douglass, E. F. Jr.; Miller, C. J.; Sparer, G.; Shapiro, H.; Spiegel, D. A. A comprehensive mathematical model for three-body binding equilibria. *J. Am. Chem. Soc.* **2013**, *135*, 6092-6099.

Chapter 2. Manifestation of Nanoheater's Position Effect on Cellular Photothermal Responses

2.1 Introduction

Within the three-dimensional cell structure, subcellular compartments possess a substantial implication in locally activating signal transduction, trafficking essential components and conveying bio-molecules to manipulate cell events as well as downstream stress effectors.[1,2] Comprehension on how to specifically monitor organelles functions, and to spatiotemporally regulate the unique signaling pathways in a sophisticated cell environment offers great possibility for in-depth understanding of the etiology of disease procession. These conceptions can be fully employed for the facilitation of targeted theranostics with maximum efficacy.[3-9] Among the various endeavors for such high accuracy, the strategy based on light irradiations, especially utilizing the near-infrared (NIR) spectral window, represents an extraordinary option to achieve deep-tissue penetration and minimize side effects of ever-present biomolecules and endogenous chromophores.[10-13]

As one typical light-responsive therapeutic modality, photothermal treatment (PTT) directly utilizes the photo absorbing components in nanostructures that are capable of absorbing and converting photon energy to heat. Such light-transduced thermal effect can ablate targeted diseases cells, thus engendering their promising applications in precision nanomedicine.[14-19] Thus far, a plethora of photothermal nano-absorbers have been developed with a main focus on the strategies to improve biocompatibility, specific diseases affinity and photoconversion efficiency for maximal thermal regulation.[20-23] However, the biological basis conferring the cellular response to PTT is still under controversy. In spite of the possibility of heat response through the expression of heat shock proteins (HSPs) as an intrinsic cytoprotective effect, their cochaperone interactions and molecular mechanism remain

elusive.[24] Moreover, the cell death pathways including apoptosis or uncontrolled cell dying, namely necrosis, occurred in photothermal response to severe heat stress have also been intensively investigated but are mostly dependent on the temperature controls by the different light treatment settings including irradiation duration, laser types and the power intensity.[25,26]

Considering the importance of subcellular compartments in cell function mediations, organelle specific localization of thermal-induced nanomaterials is critical for PTT precision with ultimate efficacy. Furthermore, attributed to the biological diversity in molecule components, native physiological properties and their relative proximity to heat-sensors, subcellular compartments can be affected divergently by localized thermal stress which might cause varied cellular responses.[27-29] However, despite the abundant designs of photothermal nano-heaters with the significant efficiency, studies on their subcellular distribution and distinguishable effects on photothermolysis are still unconceivably scarce.

Herein, we selected the rare-earth upconversion nanoparticles with surface coated polydopamine (termed as UPDAs) as a representative model of tissue penetrable NIR light-activated nano-heaters for dissecting intracellular behaviors to heat shock responses, mostly due to their unique photoluminescence properties.[30-35] Different intracellular recognition of UPDAs can be achieved by selective modification of particles surface with poly-ethylenimine (PEI) and membrane-associated bioorthogonal moieties. Typically, UPDAs were coated with PEI to provide enhanced cell uptake for efficient cytoplasm localization. We incorporated a monosaccharide precursor, peracetylated N-azidoacetylmannosamine (Ac_4ManNAz) modified with a bioorthogonal azido tag, N_3, on cell surface through the process of intrinsic glycan metabolism. Meanwhile, nanoparticles functionalized with DBCO (dibenzyl cyclooctyne) were conjugated with the pre-treated N_3-tagged glycans *via* copper-free click reaction, achieving specific surface localization of UPDAs onto live cells.[10] Upon 808 nm

laser excitation, heat released from specifically localized UPDAs was monitored to comparatively study the heat shock response in cells, thus disclosing their molecular modes of cell death (Scheme 1).

Scheme 1. Specific localization of photothermal upconversion nanoparticles dissect distinguished cellular responses to heat stress.

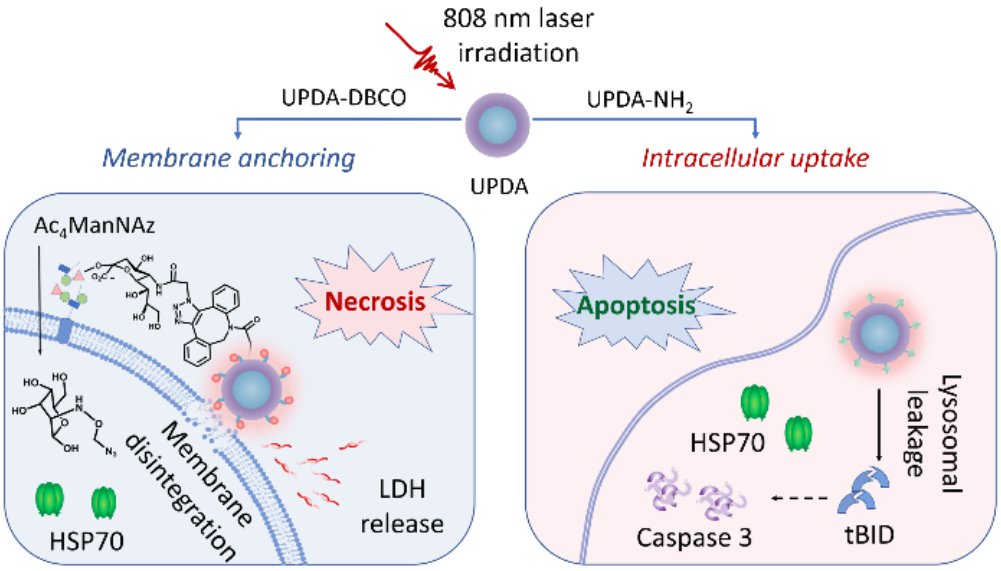

2.2 Results and discussions.

2.2.1. Rational designs and characterizations of upconversion nanoheaters.

Figure 1A presented the design of our NIR light responsive nano-heaters, in which biocompatible polydopamines with high NIR spectral absorbance[36] were coated on $NaYF_4$:Yb/Tm/Nd (30/0.5/1%) @$NaYF_4$:Nd (20%) core-shell upconversion nanoparticles (UPDA) to produce promising photothermal effect after 808 nm laser excitation. TEM images showed the homogeneous coating of polydopamine on UCNs with a thickness of 8 nm (Figure 1A). The hydrodynamic diameter in buffer solution was determined as 100.5 ± 19.13 nm through dynamic light scattering (DLS) analysis (Figure S1A). Meanwhile,

upconversion luminescence characterized by blue emission peaked at 460 nm (highest intensity emission among the emission peaks) facilitates the applicable tracking of UPDA position in live cells (Figure S1B). We then modified UPDA with different chemical moieties on the particle surface using DBCO-NH_2 by typical Michael addition and/or Schiff-based reaction with catechol and amine groups on UPDA or using PEI polymer coating (Figure S1C). The successful conjugation of DBCO on UPDA and effective click chemistry with N_3 group was confirmed by the fluorescent conjugation through 5-carboxyfluorescein-azide (FAM-N_3) with the optimal amount of DBCO of ~ 363 nmol/mg (Figure S2). Moreover, PEI was coated on UPDA for increasing the efficiency of cellular uptake, which further enhanced the subsequent localization in cytoplasm. There was no obvious morphology and shape difference observed among the modified nanoparticles (Figure S1D, E). Zeta potential measurement indicates a negative value of -10 mV for UPDA-DBCO. Meanwhile, a positive potential was found for UPDA-NH_2 (+16 mV) (Figure S1F), indicating its great possibility for cell uptake of the UPDA-NH_2.

The obtained nano-heaters demonstrated the time and concentration dependent heat effects (Figure 1B, C) upon 808 nm light illumination of the nanoparticle solution, which was also observed even under deep tissue depth (Figure S19). Importantly, the UPDAs showed great stability in different pH condition with minimum change in the absorbances, PDA thickness, nanoparticle morphology (Figure S3, 4) and repeated cycles of photothermal treatment with ΔT of around 24 ℃ (Figure S5). Moreover, these particles indicated similarity in heating and natural cooling cycles in their photothermal performance (Figure 1D) as well as calculated to have comparable photothermal conversion efficiencies (Figure S6). These properties enable a reasonable comparison of heat response through different localization of UPDA in cells by introducing equal amount of nanoparticle in each position of interest.

2.2.2. Specific cellular localization of nanoheaters.

For conjugation of nanoparticles on the cell membrane, the covalent glycan labelling approach was first conducted by introducing the N_3-tagged glycans onto human lung adenocarcinoma epithelial (A549) cells. Upon feeding with Ac_4ManNAz precursor (50 μM) for 48 hours, the A549 cells were incorporated with azido groups on the membranes through ubiquitous cellular metabolism (Figure S7). The N_3-tagged cells were further incubated with UPDA-DBCO and dynamic imaging was performed, revealing the gradual localization of UPDA on cell membrane (Figure S8). The membrane accumulation of nanoparticles reached plateau after 1 h. Notably, extended incubation time (*e.g.* 2 h) resulted in slow cellular internalization, while majority of UPDA were still anchored on the cell membrane. Moreover, control studies by unmodified UPDA alone or untagged cells revealed negligible number of nanoparticles on the cell surface, which further consolidated the specificity of the labelling through the metabolic glycol-biosynthesis (Figure S9). During this process, care needs to be taken to maximize the quantity of UPDA on the cell surface with minimum internalization by optimizing the incubation time (*e.g.* 1 h) to make sure that the specific thermal response mainly originates from the membrane localized nano-heaters (Figure S8).

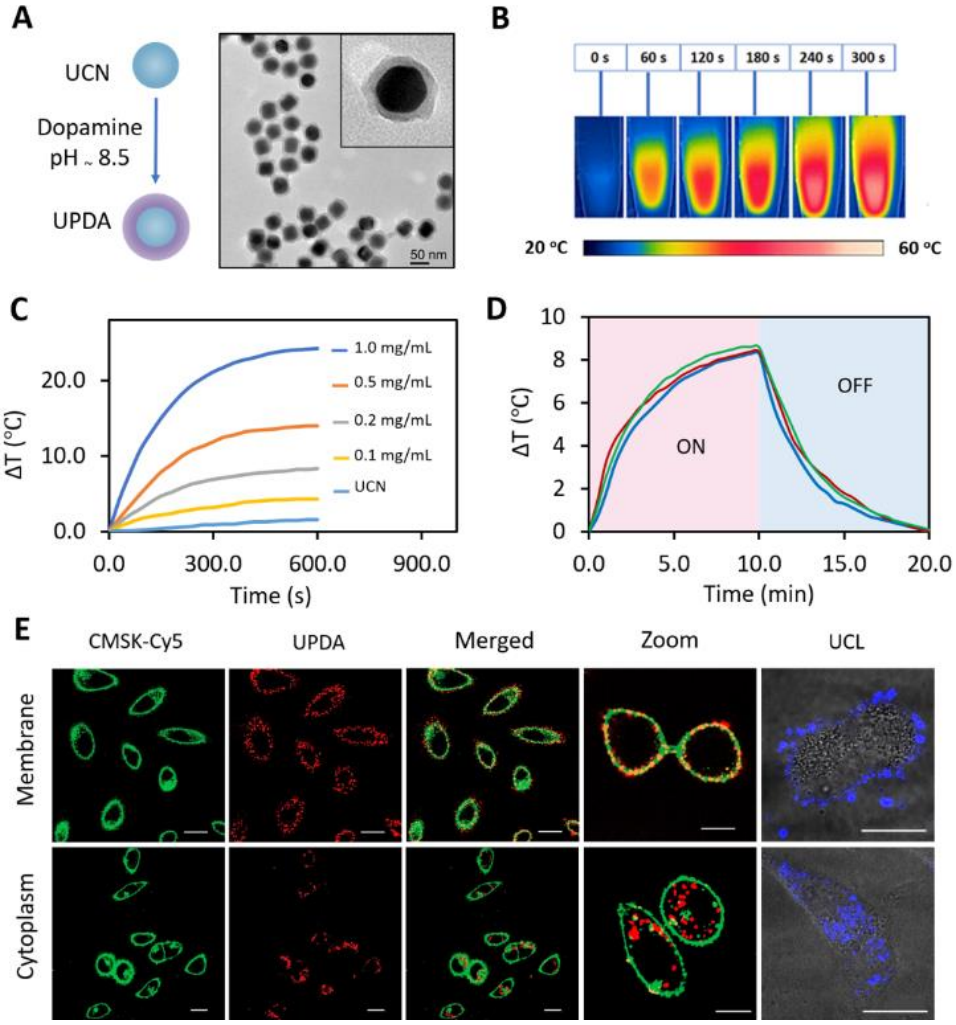

Figure 1. Fabrication and characterization of nano-heaters and the specific localization in cells. A) Polydopamine coating scheme and TEM image of polydopamine coated on upconversion nanoparticles. (B) Thermal images of irradiation-time dependent temperature increase (1 mg/mL UPDA) in aqueous solution. C) Temperature curves of UPDA under different concentrations upon 808 nm irradiation for 10 min (1.3 W/cm^2), UCNs without surface coating as a control. D) Heating curves of UPDA, UPDA-NH_2 and UPDA-DBCO (200 µg/mL) during laser irradiation and natural cooling process. E) Confocal fluorescence and upconversion luminescence (UCL) of membrane conjugation of UPDA-DBCO (top) and cytoplasm distribution of UPDA-NH_2 (down). Green: CMSK-Cy5 (λ_{ex}: 640 nm, λ_{em}: 670/50 nm), red: UPDAs (λ_{ex}: 543 nm, λ_{em}: 580/50 nm), UCL imaging at λ_{em}: 460/50 nm. Scale bar: 20 µm.

In addition, we examined the possibility for different localization of upconversion nanoheaters in live cells. Typically, the effective cellular distribution of nanoparticles inside cells can be obtained by incubation of A549 cells with UPDA-NH_2. The time-dependent cellular uptake was monitored by confocal and upconversion imaging analysis to optimize the comparable quantity of nanoparticles internalized as contrast to those UPDA-DBCO counterparts located on the membrane upon different time incubation (*e.g.* 6h, Figure S10). Indeed, as shown in Figure 1E, different from the UPDA-DBCO labelled on the plasma membrane, the UPDA-NH_2 could be taken up efficiently and almost no membrane-located interference was observed in cell imaging. In order to monitor their contribution to cellular thermal response, we individually localized UPDA-DBCO and UPDA-NH_2 into different compartments, and then carried out ICP measurement to quantify the amount of incubated UPDA in live cells.[37,38] The relatively same number of nano-absorbers (*e.g.* a ratio of ~ 1 : 1.05) were precisely maintained on the cell membrane and cytoplasm, respectively (Figure S11), which promise a rational strategy for further comparative investigations.

2.2.3. Heat shock proteins expression upon photothermal stimulation.

Upon the localization of UPDA on the different positions in the cells, both the nanoheaters on membrane and cytoplasm were irradiated with 808 nm laser (1.3 W/cm^2 at the irradiated area) for thermolysis analysis. The heat effect was carefully monitored through the NIR thermograph to optimize the proper concentration (*e.g.* 200 μg/mL) and temperature increment (*e.g.* ~ 8.5 ℃ from 37 ℃) (Figure 1C, S12) for effective photothermal response in live cells.[39] Prior to NIR light irradiation, there was no obvious thermolysis observed in the nanoparticle localized cells without laser illumination, suggesting negligible cell perturbation even under high concentration of nanoparticles (Figure S12A). After laser irradiation, cells

with specific UPDA localization experienced significant thermolysis effect (Figure S12B), suggesting suitable concentration and light treatment for further photothermal study.

Notably, soon after the heat stress was exposed, the cells started to produce heat shock protein (HSP), as a cytoprotective response against the detrimental increase of temperature (Figure S13).[40] Three hours after the heat stress triggered by NIR laser irradiation, both groups of cells with different subcellular nano-heaters localization induced the significant production of HSP70, as indicated in green fluorescence from Alexa Fluor 488 labelled anti-Hsp70 antibody (Figure 2A, B). Controlled experiments showed the minimum expression of HSP70 in cells that lack UPDA treatment or without laser irradiation (Figure S14). Quantitative fluorescence-activated cell sorting (FACS) analysis demonstrated relatively equal amount of HSP70 expression at both 1 h and 3 h post-irradiation in each group of cells (Figure 2D, E, F). Although the detailed mechanism of such stimulated protection remains controversial, the heat induced native protein denaturation could be a possible driving force to stimulate the transcription of heat shock proteins upon binding to the promotor of the specific HSP gene.[41] Additionally, recent studies also indicated the possibility of membrane perturbation for cytoprotective HSP70 expression, in which cell surface disruption could compromise the membrane integrity and give rise in bulky membrane hyperfluidization.[42] To this end, we treated the live cells with benzyl alcohol (BA), one typical membrane perturbation reagent. Indeed, as shown in Figure 2C, the effective activation of HSP70 clearly suggested the possible involvement of membrane function and the integrity in cellular response to the stimulated stress. In our case, the accumulation of UPDA on membrane concentrated heat onto a confined area, which possesses low thermal conductivity, and may therefore contribute to larger temperature gradients and membrane disruption.[43,44] Apparently, UPDA membrane conjugated A549 cells indicated the well-organized surface structure with a

specific residing of nanoparticles before NIR light exposure. However, 15 min post laser irradiation, the membrane tracker signal was disturbed, and the signal showed the releasing of cytoplasm components after 30 min (Figure S15). These results confirmed the occurrence of membrane perturbation during stimulation of UPDA localized on cell surface. Although the detailed processes involving HSPs expression require further investigation, the potential disruption of membrane integrity triggered by heat stimulation would be one noticeable perspective (Figure 2G).

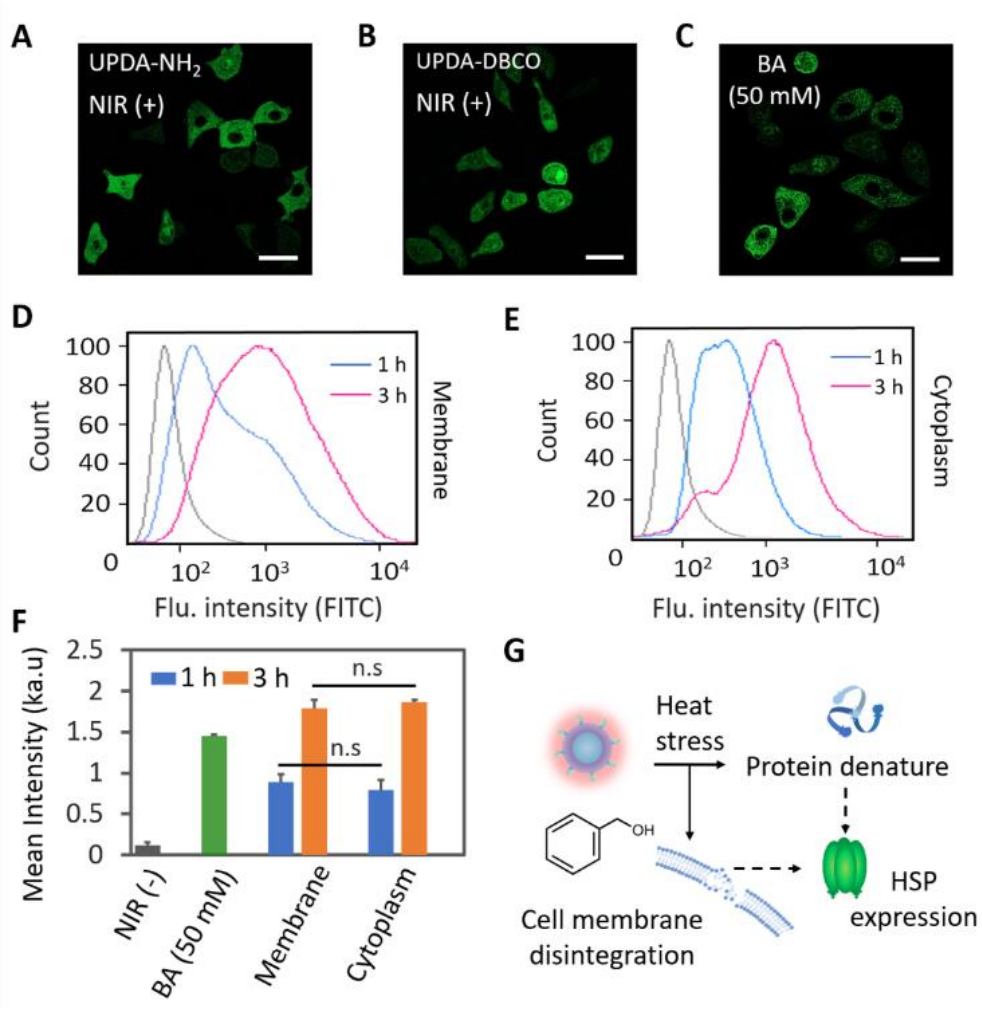

Figure 2. Cellular analysis of photothermal effect and heat shock response. **A**) Confocal images of HSP70 expression in A549 cells treated with localized UPDA-NH_2, **B**) UPDA-DBCO, 3 h after photothermal stimulation, and **C**) Benzyl alcohol (50 mM). Scale bar in

images: 40 μm. (λ_{ex}: 488 nm, λ_{em}: 515/30 nm). **D**, **E**) Flow cytometry analysis of HSP70 expression in different time points post-irradiation of cell with membrane and cytoplasm localized UPDA, respectively. Treated cells were stained with Alexa Fluor 488 labelled anti-Hsp70 antibody. **F**) Mean intensity of HSP70 levels. **G**) Potential mechanism of heat-shock protein expression.

2.2.4. Distinguishable photothermolysis at different subcellular locations.

We further examined the possible mode of cell death after NIR irradiation of nano-heaters located at different cellular compartments. Typically, cells with site-specific labelling of UPDA were irradiated and the standard AnnexinV/propidium iodide (AnnV/PI) co-staining were recruited to compare the cell death pathways. As shown in Figure 3A, heat from cytoplasm located UPDA stimulates outer membrane translocation of phosphatidylserine (PS) at early time duration after irradiation, as detected by green emission from FITC-AnnV binding protein. Upon further incubation, PI molecules were gradually permeated into the nucleus. As contrast, cells with membrane conjugated UPDA experienced rapid intracellular uptake of PI molecule. Moreover, the level of apoptosis and necrosis were analysed by FACS. Figure 3B and S16 showed similar trends of cell death pathways as observed from confocal imaging. Particularly, at 1 h and 3 h post irradiation, cells that internalized the UPDA encountered 4.96 % and 16.12 % of apoptosis at early stage, respectively. This group of cells faced secondary necrosis with approximately 31.15 % of total cells after 5 h incubation. Meanwhile, the membrane localized UPDA induced gradual increase in necrosis level from initial stage after illumination (4.48 % in 1 h to 47.09 % after 5 h) and minimum amount of early apoptosis was detected. Such different thermal response revealed that UPDA internalized cells experienced apoptotic process which remained membrane integrity at the primary stage after illumination. In contrast, membrane localized UPDA obviously caused

membrane perturbation which allows prompt internalization of PI molecules, and therefore likely to proceed the cell death pathway to necrosis.

To further validate the distinguished cellular lethality, the molecular basis associated with light triggered thermolysis was investigated. First, we employed LDH leakage as an indicative assay for membrane integrity. As indicated in Figure 3C, irradiation of cell surface distributed UPDA could lead to a time dependent LDH release. Specifically, at 5 h post-irradiation, there were nearly 3 times increase in LDH level as compared to the initial amount observed in the same culture medium. Differently, LDH content in medium was found to rise up slightly in cytoplasm localized with UPDA and the rate of leakage was much slower than the former case of UPDA on the cell surface. These different outcomes further confirmed the presence of necrosis in cells with the membrane located by UPDA.

Secondly, we investigated the activation of caspase 3, a standard biomarker for apoptosis, after locally triggered heat stress by NIR light irradiation. The fluorescent signal from caspase 3 probes was analyzed to monitor caspase 3 activity. As shown in Figure 3D, the level of caspase 3 enzyme in live cells with cytoplasm accumulation of nano-heaters uplifted to around 2 times within 3 h post laser irradiation. Whereas, in the cells with particles conjugated on the plasma membrane, less enzyme activity was detected even prolonging the incubation time, up to 5 h post laser irradiation.

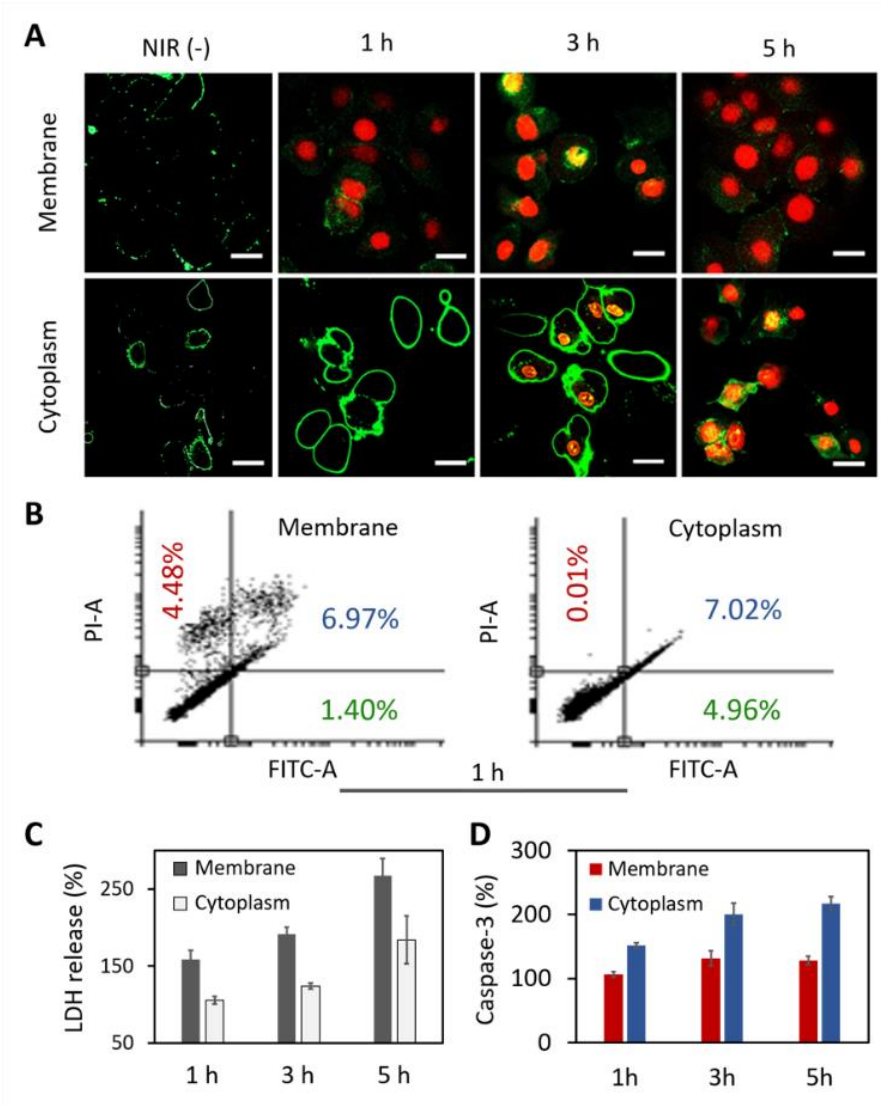

Figure 3. Cell death pathway analysis. **A**) Confocal images of AnnV-PI co-staining of the cells with specific nano-heater localization after heat stress, Green: FITC (λ_{ex}: 488 nm, λ_{em}: 515/30 nm), red: PI (λ_{ex}: 543 nm, λ_{em}: 580/50 nm). Scale bar: 20 μm. **B**) FACS analysis of apoptosis and necrosis by AnnV-PI staining of different groups of cells after 1 h irradiation. **C**) LDH release and **D**) Caspase 3 activity at 1, 3, 5 h after laser irradiation of cell with the UPDAs on membrane and in cytoplasm.

So far, apoptosis has well been recognized as one of standard pathways in the heat-stimulated cell dying, and lysosomal leakage of nano-heaters would be one critical step that

initiates chain of events before activating caspase 3 in apoptosis (Figure 4A).[45,46] Such initial step of cell death was also observed in our cells with cytoplasmic UPDA localization under NIR light exposure. After being internalized, UPDAs were mostly loaded in the lysosome as confirmed by co-localization of lysosome tracker (green) and UPDA (red) with the yellow colour in the merged image (Figure S17). Nanoparticles were released from lysosome presenting as a single red colour signal after 10 minutes NIR light illumination while negligible lysosomal escape was observed in the cell without laser irradiation (Figure 4B, S18). Principally, heat stress from nano-heaters disrupts the integrity of lysosomal membranes, resulting in lysosomal membrane permeability (LMP) that triggers cathepsin-mediated cell death pathway. At early stage of this process, a pro-apoptotic protein, Bid, can be cleaved to its truncated tBid and initialize the intrinsic mitochondria apoptosis pathway.[47] Herein, we evaluated the level of tBid in two groups of cells with site specific localization of UPDA on membrane and in cytoplasm, respectively. Typically, immunofluorescence analysis exploiting tBid antibody and fluorescent secondary antibody were applied to label tBid protein. As indicated in Figure 4C, tBid was activated in cytoplasmic UPDA containing cells, revealed by the green fluorescence, while the membrane accumulated one showed lower intensity. Western blot experiment was also performed, and the results clearly indicated the decreased amount of the full-length Bid and the enhanced quantity of tBid in the UPDA internalized cells in response to photothermal stress. Meanwhile, the similar irradiation of membrane located UPDA cells resulted in an insignificant tBid expression in comparison with the control without laser treatment (Figure 4D). These distinctive observations demonstrated that the localization of UPDA in lysosome organelle and their subsequent liberation can convert the Bid protein to its activated form, tBid, which thus functions as a key factor to initialize apoptosis. These fundamental biological assays clearly indicated the

importance of subcellular position of nano-stimulators for their differentiated heat response which will therefore affect further cell lethality significantly.

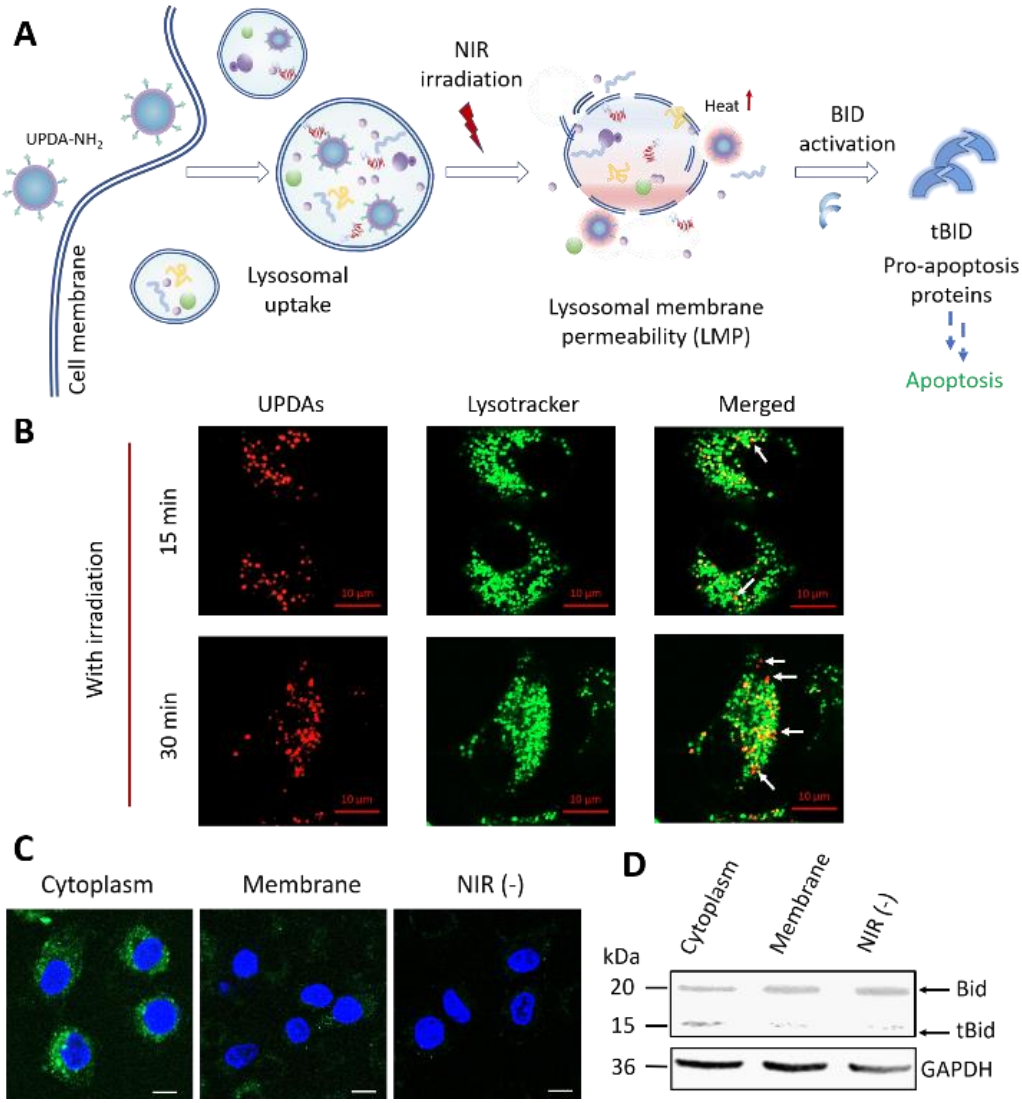

Figure 4. Lysosomal permeability to activate pro-apoptosis protein. A) Scheme of lysosomal leakage induced apoptotic cell death. B) Confocal images indicating lysosomal escape of UPDA-NH_2 at 15 and 30 min after 10 min 808 nm irradiation (1.3 Wcm^{-2}). White arrows indicate location of UPDA-NH_2 after lysosomal release. Green: Lysosomal tracker, Alexa Fluor 488 (λ_{ex}: 488 nm, λ_{em}: 515/30 nm), red: UPDA (λ_{ex}: 543 nm, λ_{em}: 580/50 nm). C) Images of tBID expression in cells with site-specific nanoparticle localization at 5 h post-irradiation. Blue: Hoechst 33342 (λ_{ex}: 405 nm, λ_{em}: 460/50 nm), green: Alexa Fluor 488 (λ_{ex}:

488 nm, λ_{em}: 515/30 nm). Scale bar: 20 μm. D) Western-blot analysis of Bid activation after irradiating the site-specific located UPDA. GAPDH was used as internal control.

2.3 Conclusion

In summary, NIR light responsive upconversion nano-heaters positioned at different cellular location can differently affect the process of cell responses on the photothermal stress. On one hand, we employed the intrinsic glycan metabolic process to introduce azido group on cell surface which subsequently conjugated the DBCO modified UPDA onto the cell membrane. Upon 808 nm laser irradiation, temperature elevation caused by UPDA-DBCO promoted the destruction of the plasma membrane, thus stimulating the expression of HSP70 and directing the cell death to necrosis. Whereas, UPDA-NH_2 were internalized by cells, where these cytoplasm localized nanoparticles not only induced HSP70 expression upon light-triggered temperature increment as those UPDAs on the cell surface, but more significantly, they can also promote lysosomal membrane permeability upon photothermal treatment, thereby inducing the activation of tBid cleavage and resulting in a differentiated cell death, apoptosis. Our study specifically revealed the molecular basis of the critical importance of photothermal nanoparticles with organelle-specific localization in manipulating cellular responses. With the ubiquitous properties of these organelles responsible for multiple cellular pathways, we expect that the integration with innovative nanotechnology designs could offer great opportunity to precisely regulate other cell functions and better understand the cellular basis of photothermal responses. Prospectively, this strategy could render optimized practical conditions for future personalized nanomedicine.

2.4. Experimental details

2.4.1. Materials

$Y(CH_3CO_2)_3$, $Yb(CH_3CO_2)_3$, $Tm(CH_3CO_2)_3$, $Nd(CH_3CO_2)_3$, oleic acid, 1-octadecene, NH_4F, NaOH, peracetylated N-azidoacetylmannosamine ($Ac_4ManNAz$), in vitro toxicology assay kit (TOX8, resazurin based), Hoechst 33342 (bisBenzimideH 33342 trihydrochloride), Dibenzylcyclootyne-amine (DBCO-NH_2), DBCO-Cy3), 5-carboxyfluorescein-azide (FAM-N3), dopamine hydrocloride, branched polyethylenimine (PEI25000), and Annexin V-PI detection kit, caspase-3 fluorometric assay kit were purchased from Sigma-Aldrich. CytoTox 96 nonradioactive cytotoxicity assay kit were purchased from Promega. Rabbit monoclonal [Y8] to Bid, Goat Anti-Rabbit IgG H&L (Alexa Fluor 488) were purchased from Abcam. BID p15 Polyclonal Antibody was purchased from Thermal Fisher. Dulbecco's Modified Eagle Medium (DMEM), Minimum Essential Medium (MEM), fetal bovine serum (FBS), penicillin-streptomycin and trypsin-EDTA, Cell Mask™ deep red plasma membrane stain kit (CMSK-Cy5). All the commercially reagents were used as received unless otherwise noted. The human lung adenocarcinoma epithelial cell line (A549) was cultured in Dulbecco's modified eagle medium (DMEM) medium with 10% fetal bovine serum (FBS) at 37 ℃ in a humidified atmosphere with 5% CO_2.

2.4.2. Characterization and measurement.

Transmission electron microscope (TEM) images were obtained using a FEI EM208S TEM (Philips) operated at 100 kV. Dynamic light scattering (DLS) and zeta potential measurements were performed by Brookhaven 90 Plus Nanoparticle Size Analyzer. Fluorescence emission spectra were recorded on a RF-5301PC Spectro fluorophotometer (Shimadzu, Japan) at room temperature. Photothermal performance was monitored by FLIR

E60 thermal imaging camera. The cell viabilities were measured by a Tecan's Infinite M200 microplate reader. Confocal imaging of cells was carried out on Carl Zeiss LSM 800 confocal laser microscopes (Germany). Photo-irradiation experiments were performed with an 808 nm NIR diode laser (Changchun New Industries Optoelectronics Technology Co., Ltd., China). Flow cytometry analysis was performed using BD LSRFortessa™ X-20 flow cytometer.

2.4.3. Synthesis of PDA-coated UCNP (UPDA)

The synthesis of $NaYF_4$:Yb/Tm/Nd (30/0.5/1%) @$NaYF_4$:Nd (20%) core-shell upcoversion nanoparticles were synthesized based on the standard method published by our group previously.[10] Subsequently, in a flask containing 5 ml of cyclohexane, 5 mg of the prepared core-shell UCNs were added together with 0.4 ml of Igepal CO-520 and sonicated for 30 min. Then, 40 μL (28 wt % in water) ammonium hydroxide was carefully added into the solution and stirred for 30 min. The aqueous solution of dopamine hydrochloride was prepared from 16 mg of dopamine hydrochloride in 100 μL of deionized water (for 8 nm polydopamine shell thickness) before slow addition of the above mixture under ultrasonication at a rate of 5 $\mu L min^{-1}$. The reaction mixture was stirred for an additional 24 h. The UPDAs were precipitated by adding ethanol, collected by centrifugation and washed several times with ethanol and water.

2.4.4. Synthesis of UPDA-DBCO, UPDA-NH_2 and Rhodamine-UPDA

The polydopamine coated UCNs were covalently modified with DBCO-NH_2 by typical Michael addition and/or Schiff-based reaction with catechol and amine groups on UPDA. Briefly, the as-prepared UPDA (5 mg) were dissolved in Tris buffer solution (pH 8.5) with a mixture of deionized water and ethanol (2:1) as solvent. DBCO-NH_2 (5 mg) was dissolved in ethanol before carefully added into the prepared mixture. After 24 h magnetic stirring at room

temperature, the DBCO-UPDA was obtained by centrifugation (14,000 rpm, 10 min) and washed by ethanol three times to remove excess reactant. The precipitate was stored in fridge before use. The amount of DBCO moiety on the surface of UCNs was determined based on the fluorescence of conjugated 5-carboxyfluorescein-azide (FAM-N_3) molecules by copper-free click chemistry reaction. Generally, the as-prepared DBCO-UPDA (1 mg) were dissolved in DMSO (200 uL) containing FAM-N_3 (0.2 mg, 43.6 μmol) and stirred in the dark for 2 h. The nanoparticle was centrifuged (14,000 rpm, 10 min) and washed by ethanol three times to remove excess reactant. The precipitate was re-dispersed in 1 mL DMSO for later determination of the DBCO binding efficiency by measuring the fluorescence at 540 nm, excitation: 488nm.

The synthesis of UPDA-NH_2 was conducted by dispersing the UPDA (5 mg) in a 1 mg/ml branched polyethylenimine (PEI25000) solution, stirred for 12 h. The obtained UDPA-NH_2 was collected by centrifugation (14,000 rpm, 10 min) and washed with ethanol and water.

For UPDA to be tracked from confocal imaging, Rhodamine B-UPDAs were synthesized. Specifically, 1 mg of Rhodamine B was activated by EDC/NHS (1:1 molar ratio) in DMSO at room temperature for 2 h. The mixture was then added dropwise into the UPDA aqueous solution (5 mg UPDA) and stirred vigorously overnight. The obtained nanoparticles were collected by centrifuging at (14,000 rpm, 10 min) and washed with ethanol 3 times for removing unbound dyes.

2.4.5. Photothermal performance measurement

0.2 mL aqueous dispersion of different concentration of UPDA nanocomposites were irradiated with an 808 nm laser at 1.3 W cm^{-2} for 10 min and monitored the temperature changes by an infrared thermal camera (E60, FLIR).

2.4.6. Cell membrane conjugation of DBCO-functionalized agents

The human lung adenocarcinoma epithelial (A549) cell line was cultured in Dulbecco's Modified Eagle Medium (DMEM) supplemented with 10 % fetal bovine serum (FBS), 100 units mL^{-1} penicillin and 100 μg mL^{-1} streptomycin and maintained in a humidified incubator with 5% CO_2 at 37 ℃. The cells were subsequently incubated with a density of 5×10^5 cells in an ibidi dish (35 mm, plastic bottom) in 1 mL DMEM medium with Ac_4ManNAz (50 μM) for 48 hours. The resulted azido-labelled cell membrane was then stained with DBCO-Cy3 (10 μM, 30 min), CMSK-Cy5 (5 μM, 10 min) and Hoechst 33342 (1 μM, 30 min) separately. The cells without azido sugar treatment and azido-labelled cell membrane blocked with DBCO-NH_2 (50 μM, 30 min) were used as control experiments.

2.4.7. Conjugation of UPDA-DBCO on cell membrane

5×10^5 A549 cells were cultured in an ibidi dish (35 mm, plastic bottom) and incubated with Ac_4ManNAz (50 μM) in DMEM medium at 37 ℃, 5% CO_2 for 48 h. The cells were then washed with PBS (pH 7.4) three times before adding 200 μg/ml of UPDA-DBCO in 1 mL DMEM medium. After further 1-hour incubation, the cells were washed carefully with PBS three times and the specific localization of nanoparticles was monitored by a confocal microscope with CMSK-Cy5 as a membrane tracker.

2.4.8. UPDA-NH_2 localization in the cytoplasm

5×10^5 A549 cells were cultured in an ibidi dish (35 mm, plastic bottom) in DMEM medium. After 48 h, the cells were washed with PBS three times before adding 200 μg/ml UPDA-NH_2 and further incubated for 6 h. The specific distribution of nanoparticles inside the cells was monitored using a confocal microscope with CMSK-Cy5 as a membrane tracker.

2.4.9. ICP quantification of UPDA

Two groups of cells after specific localization of UPDA (using optimized condition for each localization) was washed three time with PBS. After that, the cells were collected by 0.25% trypsin-EDTA, centrifuged at high-speed (10, 000 rpm, 10 min) and treated with 70% nitric acid for 24 h. The clear solution was diluted in water (2% nitric acid), filtered with 0.22 μm filter and analyzed for yttrium (Y^{3+}) concentration by ICP-OES.[37,38]

2.4.10. Cell viability test

The A549 cells were seeded with a density of 1×10^4 cells per well in 200 μL DMEM in the 96-wells plate and incubated with 50 μM of Ac_4ManNAz for another 48h before adding UPDA-DBCO with different concentration in 1h for membrane conjugation and incubated for 24h. Meanwhile, other A549 cells were seeded with a density of 1×10^4 cells per well in 200 μL DMEM in the 96-wells plate and incubated for 48 h before washed carefully with PBS and incubated with different concentration of UPDA-NH_2 in culture medium for internalization during 24 h. After that, the cell treated with different nanoparticles were washed with PBS and fresh cell culture medium containing TOX8 was added to the wells, and the plate was incubated for another 3 h. The fluorescence at 590 nm was measured by a Tecan's Infinite M200 microplate reader with 560 nm excitation. Cell viability was expressed by the ratio of the fluorescence of cells conjugated with nanoparticles to that of control.

For photothermal cell viability test, A549 cells with specific conjugation of UPDA was monitored with previous mentioned incubation time to have equal number of nanoparticles in each group of cells before being irradiated with 1.3 Wcm^{-2} 808 nm laser for 10 minutes. The photothermal treated cells was then further incubated for 24 h before being washed with PBS and measured the viability using the same TOX8 based method described above.

2.4.11. Hsp70-expression analysis

UPDA membrane conjugated and UPDA cytoplasm localization of A549 cells were seeded on the 8-well ibidi dishes containing 5×10^4 cells per well in 200 μL DMEM media. After 10 min irradiation with 1.3 Wcm^{-2} 808 nm laser irradiation, the media was removed, and cells were washed with PBS 3 times. After additional incubation for 5 min, 1 h, 3 h, 5 h, A549 cells were washed and fixed with 4% paraformaldehyde solution for 15 min at room temperature. After that A549 cells were washed with PBS before staining with anti-Hsp70 antibody conjugated with Alexa Fluor 488 (Biolegend Alexa Fluor 488 anti-Hsp70) at room temperature for 15 min. Stained A549 cells were washed with PBS and observed with confocal microscope.

For flow cytometry (FCM) analysis, A549 cells was seeded in 6 well dishes in 2 mL DMEM cell culture media with density of 1×10^6 cells per well and allowed for site-specific localization of UPDA-DBCO and UPDA-NH_2 (200 ug/mL for each). After photothermal treatment as above-mentioned method, cells were further incubated for 1 h or 3 h before collected by 0.25% trypsin-EDTA, fixed with 4% paraformaldehyde solution for 15 min at room temperature. The collected cells of each group were washed with PBS before staining with anti-Hsp70 antibody conjugated with Alexa Fluor 488 (Biolegend Alexa Fluor 488 anti-Hsp70) at room temperature for 15 min. Stained A549 cells were washed with PBS and analysed with BD LSRFortessa™ X-20 flow cytometer.

For benzyl alcohol induced HSP70 expression, 1×10^6 in ibidi dished (35 mm) was incubated with 50 mM of BA in cell culture DMEM media for 1 hour. After that, the cells were carefully washed with PBS and fixed with 4% paraformaldehyde solution for 15 min at room temperature before staining with anti-Hsp70 antibody conjugated with Alexa Fluor 488

(Biolegend Alexa Fluor 488 anti-Hsp70) at room temperature for 15 min. Stained A549 cells were washed with PBS and observed with confocal microscope, using 488 nm laser and 480 ± 25 nm filter. For FCM analysis, cells with the same BA treatment condition were collected by 0.25% trypsin-EDTA, fixed with 4% paraformaldehyde solution for 15 min at room temperature. The collected cells were then washed and stained with anti-Hsp70 antibody before analysed with BD LSRFortessa™ X-20 flow cytometer.

2.4.12. Apoptosis/ necrosis imaging and FCM analysis

Double-stain molecular probe consisting of Annexin V-Alexa Fluor 488 (AnnV) for detecting apoptosis cells and propidium iodide (PI) staining necrotic cells was used to investigate the membrane integrity as well as cell necrosis and apoptosis. Typically, 5 µL volume of AnnV (100 µg/mL) and a 1 µL volume of PI (100 µg/mL) were added to each group of cells with different site-specific UPDA localization after photothermal treatment in 100 µL of 1× annexin-binding buffer. After staining, fluorescence images were taken using a Carl Zeiss LSM 800 confocal laser microscope and the quantity of early apoptosis, late apoptosis and necrosis cells was analysed by BD LSRFortessa™ X-20 flow cytometer.

2.4.13. LDH release assay

For investigation of necrosis, Cyto Tox 96 assay (Promega) was carried out according to the manufacturer's instructions. Generally, each group of site-specific UPDA localization cells was grown in 96 well-plates with 1×10^4 cells/well density. Cells was washed with PBS before photothermal treatment. After 1-, 3-, and 5-hours additional incubation, the sample solution was incubated with LDH substrate buffer solution in dark for 30 minutes. Then, stop solution was added before measuring the absorbance at 490 nm a Tecan's Infinite M200

microplate reader. Each experiment was repeated three times and the results was reported in average values and standard deviations.

2.4.14. Caspase 3 activity assay

Caspase 3 activity assay (Caspase 3 Assay Kit, Fluorimetric, Sigma-Aldrich) was carried out according to the manufacturer's instructions. Typically, 1×10^4 site-specific UPDA localization cells were grown in each well of 96 well plate. After photothermal treatment, cells were washed with PBS and lysis buffer was added. The cells were then allowed to be lysed in 0 ℃ for 20 min. Consequently, assay buffer containing caspase 3 probe was added and further incubated for 30 min. The increase in fluorescence at 460 nm under 360 nm excitation of each sample solution was recorded by a Varian Cary Eclipse Fluorescence Spectrophotometer. Each experiment was repeated three times and the results was reported in average values and standard deviations.

2.4.15. Immunofluorescence analysis of tBid protein

Each group of site-specific localization of UPDA cell with density of 5×10^4 cells in each well of 8-well ibidi-dishes was experienced photothermal treatment as described above. After 5 h, the cells were fixed with 4% paraformaldehyde for 15 minutes, permeabilized with 0.25% Triton™ X-100 for 10 minutes and blocked with 5% BSA for 1 hour at room temperature. The cells were then labelled with BID (p15) Rabbit polyclonal Antibody in 1% BSA and incubated for 3 hours at room temperature. Subsequently, Alexa Fluor 488-Goat Anti-Rabbit IgG secondary antibody was stained for 30 minutes at room temperature. Nucleus was stained with Hoechst 33342. The induction of Bid cleavage site (p15 tBID) was visualized with Carl Zeiss LSM 800 microscopes. (Hoechst 33342: Ex = 405 nm, Em = 460/50 nm; Alexa Fluor 488: Ex = 488 nm, Em = 515/30 nm).

2.4.16. Western-blot analysis of Bid protein activation

The lysates of each group of site-specific localization UPDA at 5 h after photothermal treatment were collected and centrifuged at 12,000 × g for 10 min at 4 ℃. Protein levels in supernatants were determined using Nanodrop and equalized to the same concentration and boiled for 10 min with SDS-PAGE sample loading buffer before being separated using SDS-PAGE and transferred to the PVDF membrane. The membrane was then blocked with 5% BSA-TBST blocking buffer overnight at 4 ℃. Subsequently, full length BID primary antibody (1:2000) (Rabbit monoclonal [Y8] to Bid, abcam) and p15 Bid cleavage site-specific antibody (1:1000) was incubated at room temperature for 2 hours in 2% BSA-TBST buffer. After series of washing, the goat-anti rabbit IGG (H&L) secondary antibody was added and incubated for 1 hour in 2% BSA-TBST. All signals were developed using Super Signal West Femto kit, visualized using myECL imager.

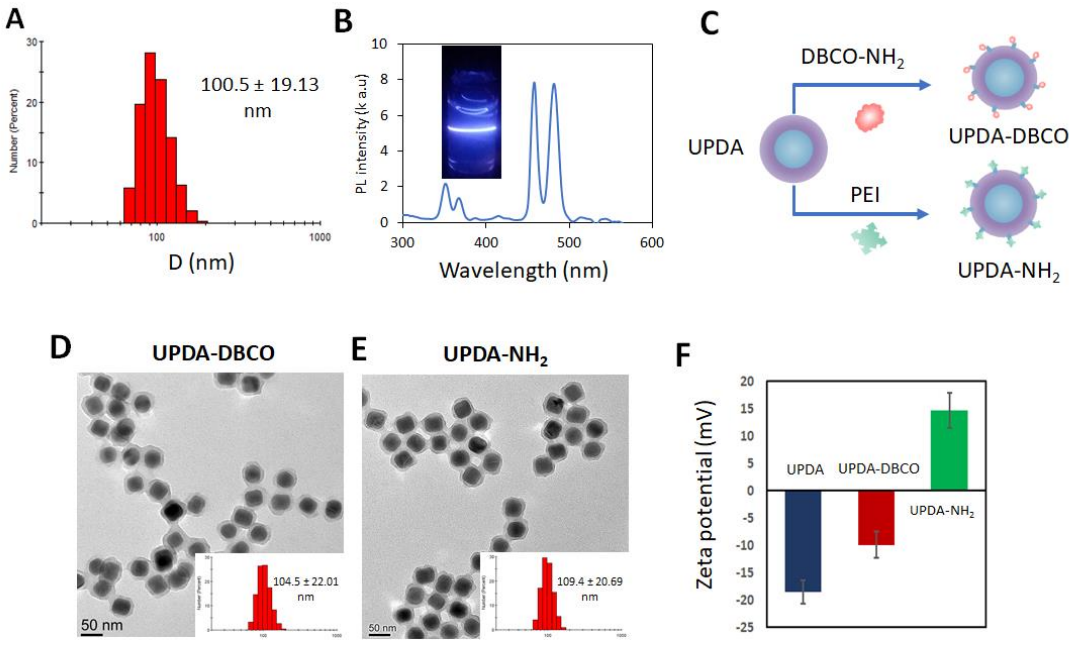

Figure S1. A) DLS measurement of hydrodynamic size of UPDA. B) Upconversion luminescence spectra (inset: photoluminescence image) of UPDA (1 mg/ml) at λ_{ex} = 808 nm. C) Scheme of UPDA modification for site-specific localization of UPDA. D, E) TEM images of UPDA-DBCO and UPDA-NH_2. Insets are DLS of hydrodynamic sizes. F) Zeta potential of UPDA, UPDA-DBCO, UPDA-NH_2.

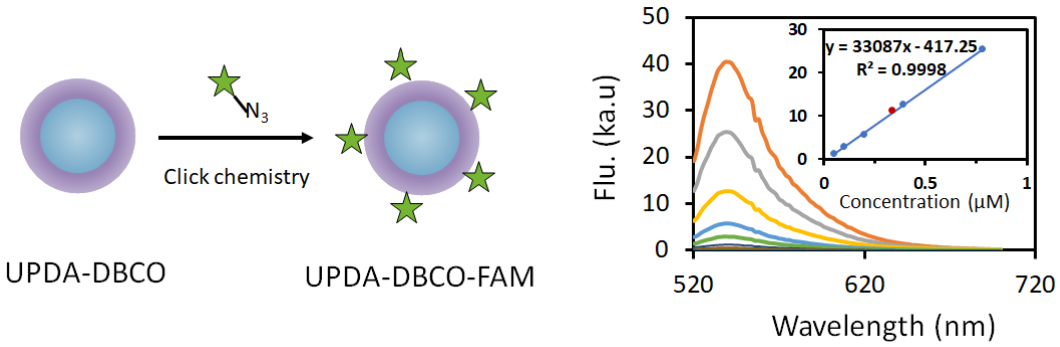

Figure S2. A) Schematic illustration for detecting the DBCO moiety on the UPDA. B) Fluorescence spectra of FAM-N_3 and the standard curve for quantifying the amount of DBCO in 1 mg/mL UPDA-DBCO. (λ_{ex}: 488 nm, λ_{em}: 540 nm).

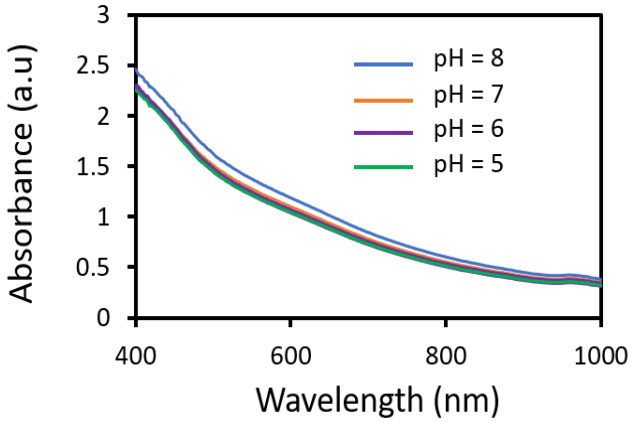

Figure S3. Absorbance of UPDAs in varied pH buffer solutions after 24 h storage at room temperature.

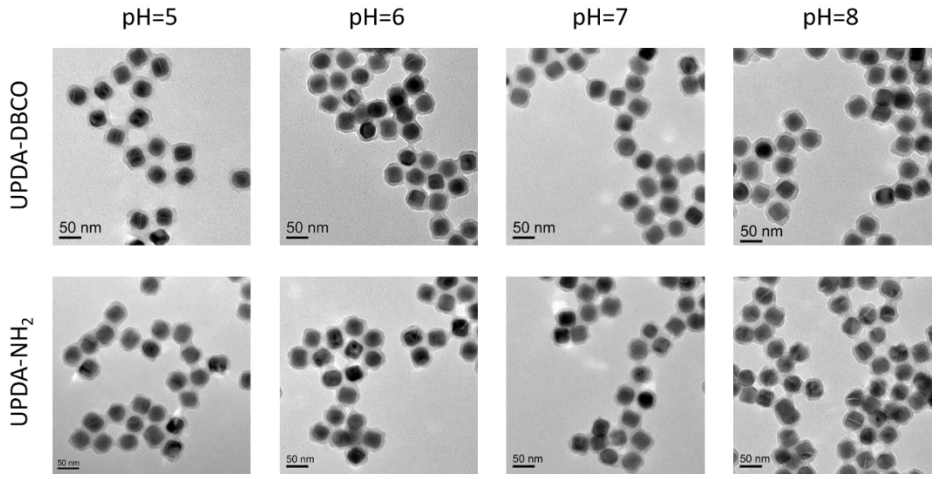

Figure S4. TEM images of UPDA-DBCO and UPDA-NH_2 after 24 h storage in different pH buffers.

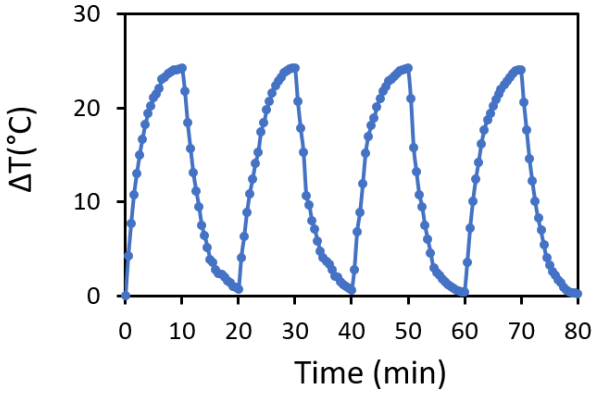

Figure S5. Measurement of photostability by monitoring temperature performance of UPDA aqueous solution (1 mg/ml) upon laser on/off cycles.

A

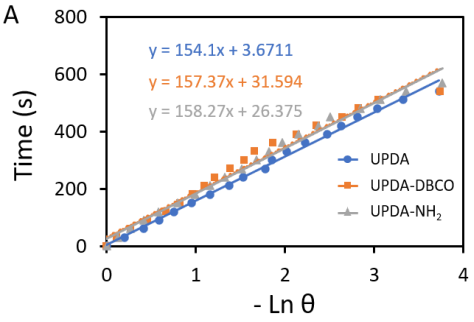

B

Nanoparticle	τ_s (S)	Photothermal conversion efficiency
UPDA	154.10	48.81%
UPDA-DBCO	157.37	48.28%
$UPDA-NH_2$	158.27	49. 31%

Figure S6. A) Time constant for heat transfer from the system is determined by applying the linear time data from the cooling period *versus* negative natural logarithm of driving force temperature. B) Table of calculated photothermal conversion efficiencies.

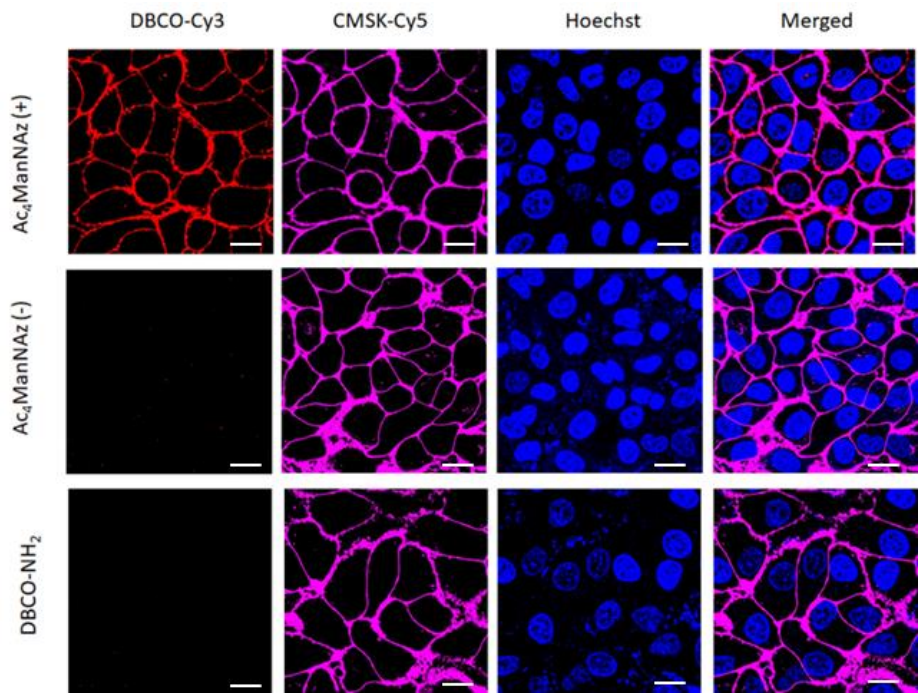

Figure S7. Imaging azido groups on A549 cell membrane stained by DBCO-Cy3 (10 μM) after feeding with (top) or without (middle) Ac_4ManNAz (50 μM) for 48 h. DBCO-NH_2 was also added in Ac_4ManNAz treated cells (bottom) as a control. Blue: Hoechst 33342 (λ_{ex}: 405 nm, λ_{em}: 460/50 nm), red: DBCO-Cy3 (λ_{ex}: 543 nm, λ_{em}: 580/50 nm), violet: CMSK-Cy5 (λ_{ex}: 640 nm, λ_{em}: 670/50 nm). Scale bar: 60 μm.

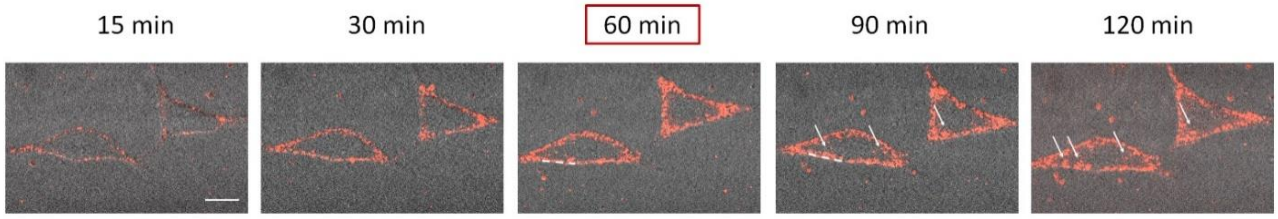

Figure S8. Confocal images of conjugation of UPDA-DBCO on A549 cell membrane at different incubation times (red: UPDA-DBCO, λ_{ex}: 543 nm, λ_{em}: 580/50 nm). Scale bar: 20 μm.

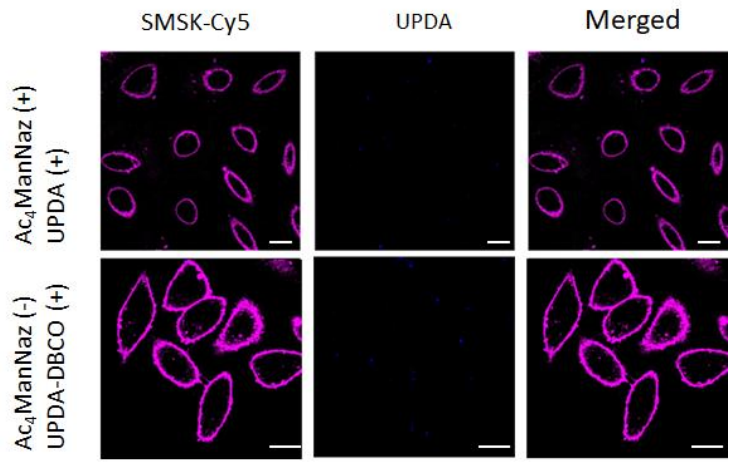

Figure S9. Confocal images of UPDA distribution in A549 cells with Ac_4ManNaz feeding and UPDA incubation (top) and with UPDA-DBCO but without Ac_4ManNaz treatment (bottom). The cells were incubated with UPDAs for 1 h. Violet: CMSK-Cy5 (λ_{ex}: 640 nm, λ_{em}: 670/50 nm), blue: UPDAs (λ_{ex}: 543 nm, λ_{em}: 580/50 nm). Scale bar: 40 μm.

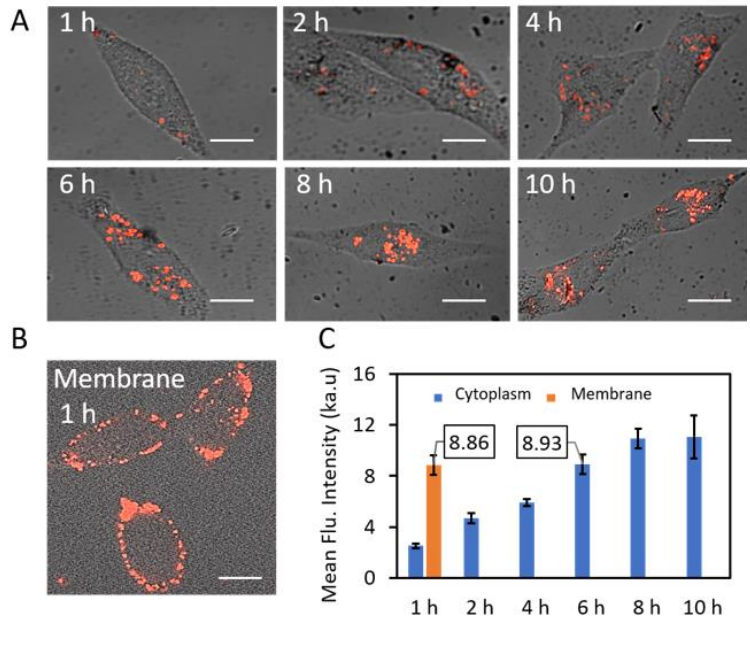

Figure S10. A) Time-lapsed cytoplasm localization of UPDA-NH_2. B) Images of cell membrane conjugation of UPDA-DBCO with optimized treatment condition (200 μg/ml, 1 h incubation). C) Mean fluorescence intensity of the uptake UPDAs during different time

controls in comparison with that of membrane located UPDAs after optimum treatment condition.

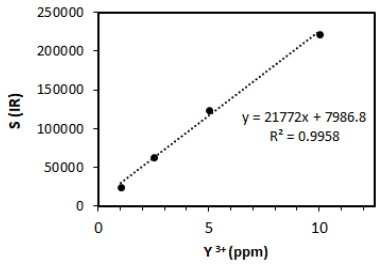

	Membrane	Cytoplasm
Concentration (ppm)	3.2910 ± 0.0244	3.4540 ± 0.0237
Relative ratio	1.00	1.05

Figure S11. ICP analysis of Y element in site-specific UPDA conjugation cells. Graph: calibration curve for quantification of Y. Table: quantification of Y in real sample of cells with membrane bounded-UPDA and cytoplasm located UPDA.

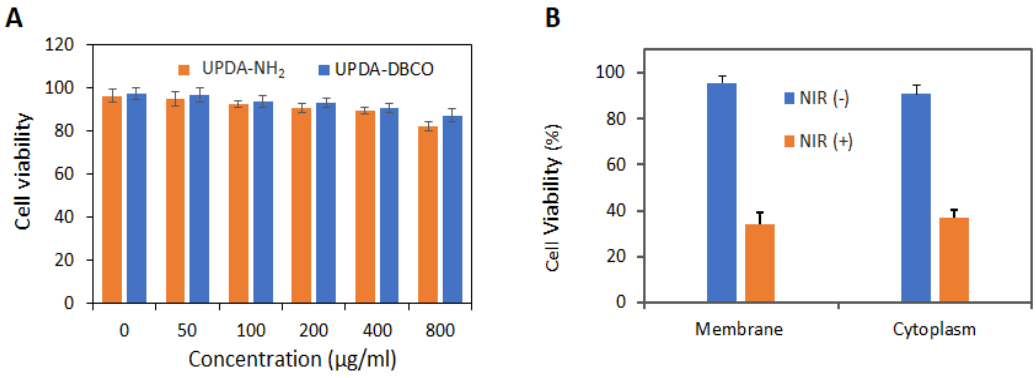

Figure S12. A) Cytotoxicity test of A549 cells after treatment with different concentration of UPDA-DBCO and UPDA-NH_2. B) Cell viability of cells treated with UPDA-DBCO and UPDA-NH_2 (200 µg/ml) before and after photothermal treatment with 10 minutes of 808 nm laser irradiation (1.3 Wcm^{-2}).

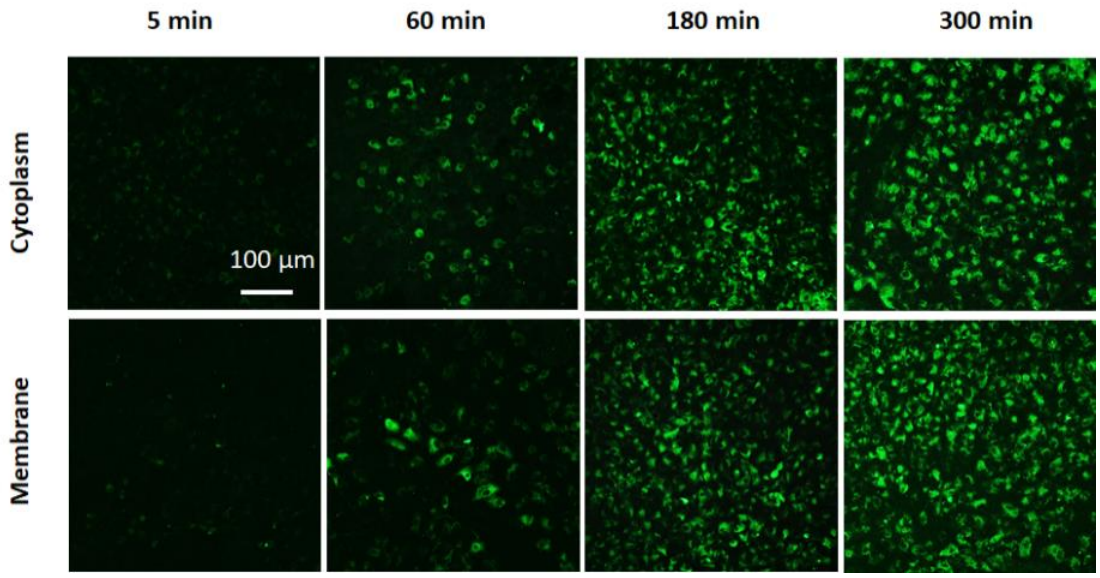

Figure S13. Confocal images of HSP70 expression of cells with different location of UPDA at different time points after 10 minutes of 808 nm laser irradiation (1.3 Wcm^{-2}). Green: Alexa Fluor 488 (λ_{ex}: 488 nm, λ_{em}: 515/30 nm).

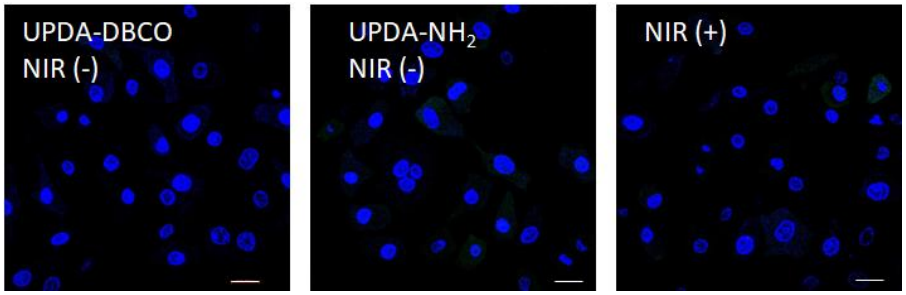

Figure S14. Confocal images of HSP70 expression of A549 cells in controlled experiments. Hoechst was used for nucleus tracking. Green: Alexa Fluor 488 (λ_{ex}: 488 nm, λ_{em}: 515/30 nm), blue: Hoechst 33342 (λ_{ex}: 405 nm, λ_{em}: 460/50 nm). Scale bar: 20 μm.

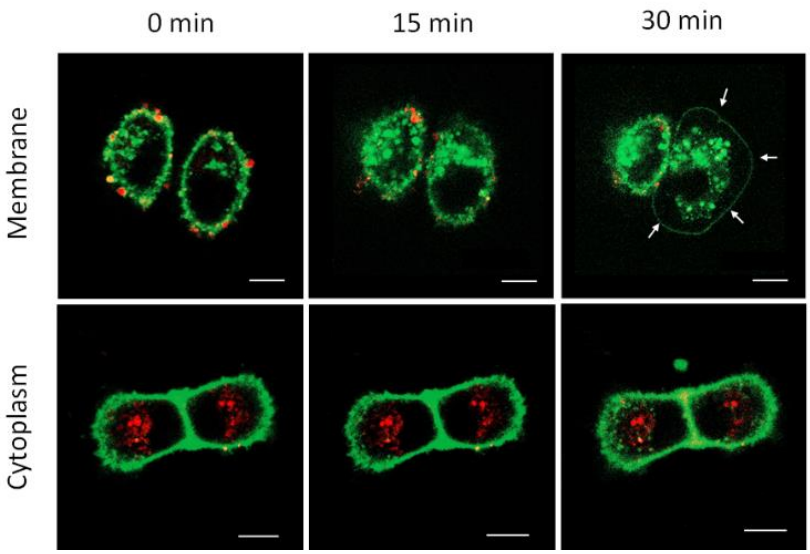

Figure S15. Confocal images of membrane and cytoplasm specific located UPDA in A549 cells before and after 10 minutes of 808 nm laser irradiation (1.3 Wcm^{-2}). Green: CMSK-Cy5 (λ_{ex}: 640 nm, λ_{em}: 670/50 nm), red: UPDAs (λ_{ex}: 543 nm, λ_{em}: 580/50 nm). Scale bar: 10 µm.

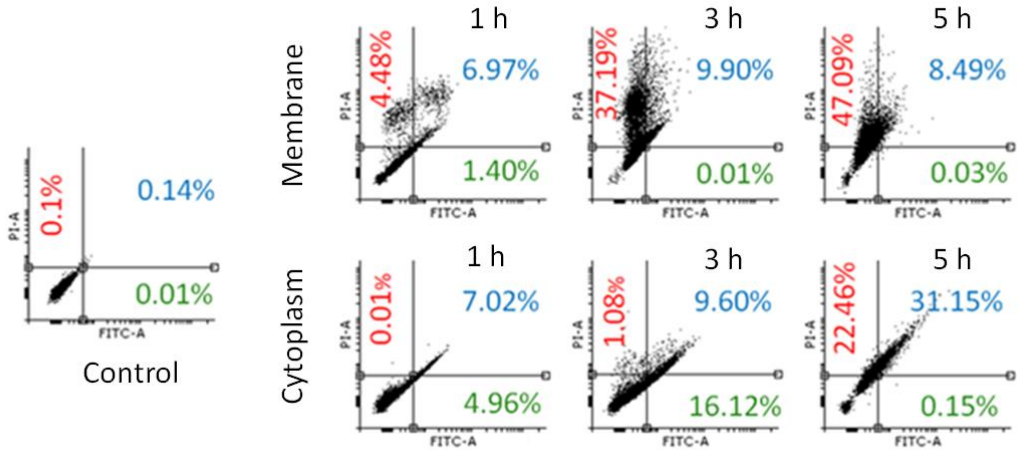

Figure S16. Flow cytometry analysis of AnnV/PI staining cells with membrane and cytoplasm specific UPDA localization 1 h, 3 h, 5 h after 10 minutes 808 nm laser irradiation (1.3 Wcm^{-2}). Red numbers indicate necrosis, blue numbers secondary necrosis/ late apoptosis and green numbers indicate early apoptosis.

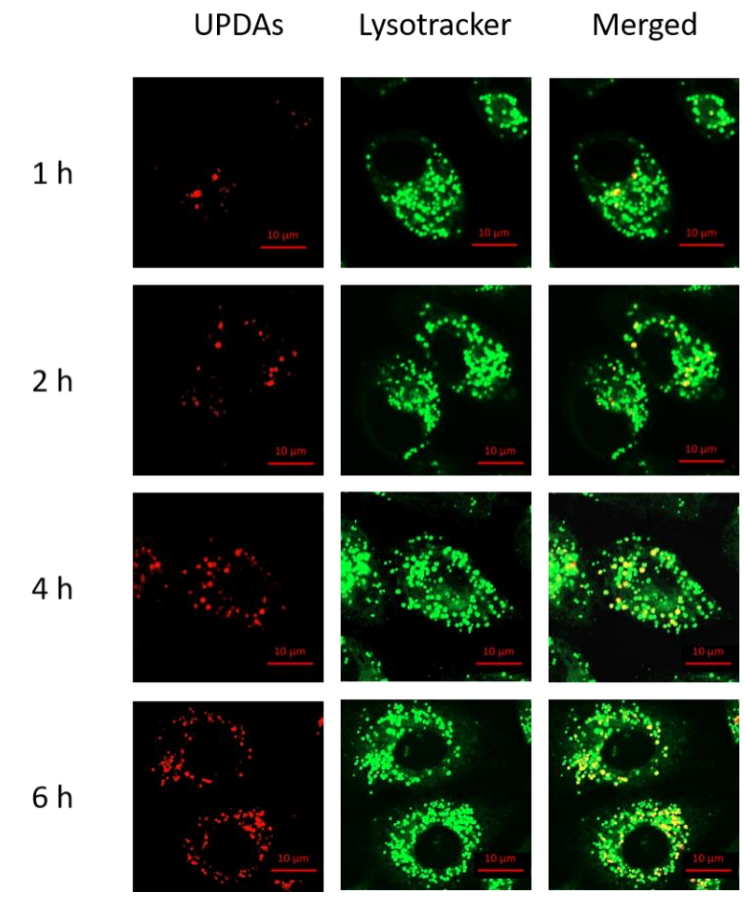

Figure S17. Time-dependent lysosomal uptake of UPDA-NH_2. Green: lysosomal tracker, Alexa Fluor 488 (λ_{ex}: 488 nm, λ_{em}: 515/30 nm); red: UPDA (λ_{ex}: 543 nm, λ_{em}: 580/50 nm).

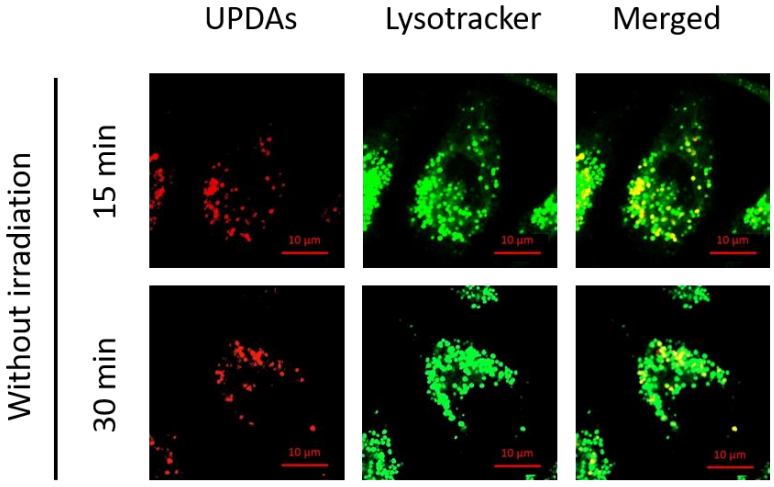

Figure S18. Confocal images of cells without laser irradiation show minimum lysosomal escape. Green: lysosomal tracker, Alexa Fluor 488 (λ_{ex}: 488 nm, λ_{em}: 515/30 nm); red: UPDA (λ_{ex}: 543 nm, λ_{em}: 580/50 nm).

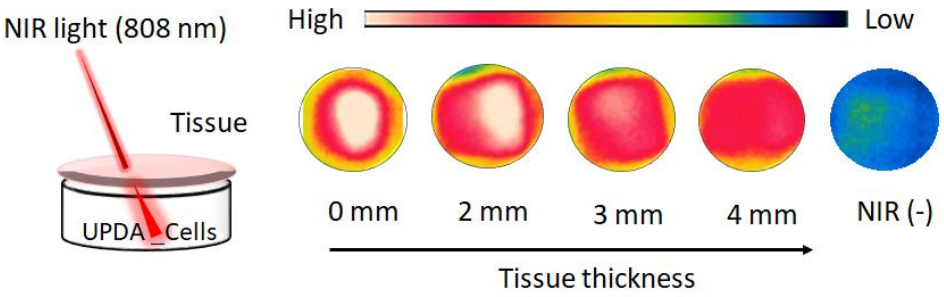

Figure S19. Deep tissue penetration properties of 808 nm light. Cells that uptake UPDA were covered with chicken tissue in different thicknesses and irradiated with 808 nm light (1.3 Wcm^{-2}). Thermal images of cell dishes (after removing chicken tissue) were then taken after 10 minutes irradiation.

2.5. References

1. Galluzzi, L.; Bravo-San Pedro, J. M.; Kroemer, G. Organelle-Specific Initiation of Cell Death. *Nat. Cell Biol.* **2014**, *16*, 728.

2. Lundberg, E.; Borner, G. H. Spatial Proteomics: A Powerful Discovery Tool for Cell Biology. *Nat. Rev. Mol. Cell Bio.* **2019**, *20*, 285-302.

3. Ali, M. R.; Wu, Y.; Tang, Y.; Xiao, H.; Chen, K.; Han, T.; Fang, N.; Wu, R.; El-Sayed, M. A. Targeting Cancer Cell Integrins Using Gold Nanorods in Photothermal Therapy Inhibits Migration through Affecting Cytoskeletal Proteins. *Proc. Natl. Acad. Sci.* **2017**, *114*, E5655-E5663.

4. Lyu, Y.; Cui, D.; Sun, H.; Miao, Y.; Duan, H.; Pu, K. Dendronized Semiconducting Polymer as Photothermal Nanocarrier for Remote Activation of Gene Expression. *Angew. Chem. Int. Ed.* **2017**, *56*, 9155-9159.

5. Feng, Z.; Wang, H.; Wang, S.; Zhang, Q.; Zhang, X.; Rodal, A. A.; Xu, B. Enzymatic Assemblies Disrupt the Membrane and Target Endoplasmic Reticulum for Selective Cancer Cell Death. *J. Am. Chem. Soc.* **2018**, *140*, 9566-9573.

6. Zhu, H.; Fan, J.; Du, J.; Peng, X. Fluorescent Probes for Sensing and Imaging within Specific Cellular Organelles. *Acc. Chem. Res.* **2016**, *49*, 2115-2126.

7. Ma, X.; Gong, N.; Zhong, L.; Sun, J.; Liang, X.-J. Future of Nanotherapeutics: Targeting the Cellular Sub-Organelles. *Biomaterials* **2016**, *97*, 10-21.

8. Wang, H.; Feng, Z.; Wang, Y.; Zhou, R.; Yang, Z.; Xu, B. Integrating Enzymatic Self-Assembly and Mitochondria Targeting for Selectively Killing Cancer Cells without Acquired Drug Resistance. *J. Am. Chem. Soc.* **2016**, *138*, 16046-16055.

9. Chen, H.; Wang, J.; Feng, X.; Zhu, M.; Hoffmann, S.; Hsu, A.; Qian, K.; Huang, D.; Zhao, F.; Liu, W. Mitochondria-Targeting Fluorescent Molecules for High Efficiency Cancer Growth Inhibition and Imaging. *Chem. Sci.* **2019**, *10*, 7946-7951.

10. Ai, X.; Lyu, L.; Zhang, Y.; Tang, Y.; Mu, J.; Liu, F.; Zhou, Y.; Zuo, Z.; Liu, G.; Xing, B. Remote Regulation of Membrane Channel Activity by Site-Specific Localization of Lanthanide-Doped Upconversion Nanocrystals. *Angew. Chem. Int. Ed.* **2017**, *56*, 3031-3035.

11. Gao, W.; Li, S.; Liu, Z.; Sun, Y.; Cao, W.; Tong, L.; Cui, G.; Tang, B. Targeting and Destroying Tumor Vasculature with a Near-Infrared Laser-Activated “Nanobomb” for Efficient Tumor Ablation. *Biomaterials* **2017**, *139*, 1-11.

12. Zhang, R.; Cheng, K.; Antaris, A. L.; Ma, X.; Yang, M.; Ramakrishnan, S.; Liu, G.; Lu, A.; Dai, H.; Tian, M. Hybrid Anisotropic Nanostructures for Dual-Modal Cancer Imaging and Image-Guided Chemo-Thermo Therapies. *Biomaterials* **2016**, *103*, 265-277.

13. Yu, N.; Huang, L.; Zhou, Y.; Xue, T.; Chen, Z.; Han, G. Near-Infrared-Light Activatable Nanoparticles for Deep-Tissue-Penetrating Wireless Optogenetics. *Adv. Healthc. Mater.* **2019**, *8*, 1801132.

14. Huang, X.; El-Sayed, I. H.; Qian, W.; El-Sayed, M. A. Cancer Cell Imaging and Photothermal Therapy in the Near-Infrared Region by Using Gold Nanorods. *J. Am. Chem. Soc.* **2006**, *128*, 2115-2120.

15. Chan, M.-H.; Chen, S.-P.; Chen, C.-W.; Chan, Y.-C.; Lin, R. J.; Tsai, D. P.; Hsiao, M.; Chung, R.-J.; Chen, X.; Liu, R.-S. Single 808 nm Laser Treatment Comprising Photothermal and Photodynamic Therapies by Using Gold Nanorods Hybrid Upconversion Particles. *J. Phys. Chem C.* **2018**, *122*, 2402-2412.

16. Wang, Z.; Zhen, X.; Upputuri, P. K.; Jiang, Y.; Lau, J.; Pramanik, M.; Pu, K.; Xing, B. Redox-Activatable and Acid-Enhanced Nanotheranostics for Second Near-Infrared Photoacoustic Tomography and Combined Photothermal Tumor Therapy. *ACS Nano* **2019**, *13 (5)*, 5816-5825.

17. Chan, M. H.; Pan, Y. T.; Lee, I. J.; Chen, C. W.; Chan, Y. C.; Hsiao, M.; Wang, F.; Sun, L.; Chen, X.; Liu, R. S. Minimizing the Heat Effect of Photodynamic Therapy Based on Inorganic Nanocomposites Mediated by 808 nm Near-Infrared Light. *Small* **2017**, *13*, 1700038.

18. Liu, G.; Zhu, J.; Guo, H.; Sun, A.; Chen, P.; Xi, L.; Huang, W.; Song, X.; Dong, X. Mo_2C-Derived Polyoxometalate for NIR-II Photoacoustic Imaging-Guided Chemodynamic/Photothermal Synergistic Therapy. *Angew. Chem. Int. Ed.* **2019**, 58, 18641-18646.

19. Dong, Q.; Wang, X.; Hu, X.; Xiao, L.; Zhang, L.; Song, L.; Xu, M.; Zou, Y.; Chen, L.; Chen, Z.; Tan, W. Simultaneous Application of Photothermal Therapy and an Anti-Inflammatory Prodrug Using Pyrene-Aspirin-Loaded Gold Nanorod Graphitic Nanocapsules. *Angew. Chem. Int. Ed.* **2018**, *57*, 177-181.

20. Kenneth, K. Ng.; Misa, T.; Cheng, C.S. Jin.; Zheng, G., Self-Sensing Porphysomes for Fluorescence-Guided Photothermal Therapy. *Bioconjugate. Chem.* ***2015***, 26, 345-351.

21. Valcourt, D. M.; Dang, M. N.; Day, E. S. IR820-Loaded PLGA Nanoparticles for Photothermal Therapy of Triple-Negative Breast Cancer. *J. Biomed. Mater. Res. Part A.* **2019**, 107, 1702-1712

22. Feng, W.; Han, X.; Wang, R.; Gao, X.; Hu, P.; Yue, W.; Chen, Y.; Shi, J. Nanocatalysts-Augmented and Photothermal-Enhanced Tumor-Specific Sequential Nanocatalytic Therapy in Both NIR-I and NIR-II Biowindows. *Adv. Mater.* **2019**, *31*, 1805919.

23. Yuan, H.; Fales, A. M.; Vo-Dinh, T. TAT Peptide-Functionalized Gold Nanostars: Enhanced Intracellular Delivery and Efficient NIR Photothermal Therapy Using Ultralow Irradiance. *J. Am. Chem. Soc.* **2012**, *134*, 11358-11361.

24. Delbecq, S. P.; Rosenbaum, J. C.; Klevit, R. E. A Mechanism of Subunit Recruitment in Human Small Heat Shock Protein Oligomers. *Biochemistry* **2015**, *54*, 4276-4284.

25. Pérez-Hernández, M.; del Pino, P.; Mitchell, S. G.; Moros, M.; Stepien, G.; Pelaz, B.; Parak, W. J.; Gálvez, E. M.; Pardo, J.; de la Fuente, J. s. M. Dissecting the Molecular Mechanism of Apoptosis during Photothermal Therapy Using Gold Nanoprisms. *ACS Nano* **2014**, *9*, 52-61.

26. Zhu, X.; Feng, W.; Chang, J.; Tan, Y.-W.; Li, J.; Chen, M.; Sun, Y.; Li, F. Temperature-Feedback Upconversion Nanocomposite for Accurate Photothermal Therapy at Facile Temperature. *Nat. Commun.* **2016**, *7*, 10437.

27. Li, W.; Yang, J.; Luo, L.; Jiang, M.; Qin, B.; Yin, H.; Zhu, C.; Yuan, X.; Zhang, J.; Luo, Z. Targeting Photodynamic and Photothermal Therapy to the Endoplasmic Reticulum Enhances Immunogenic Cancer Cell Death. *Nat. Commun.* **2019**, *10*, 1-16.

28. Li, N.; Sun, Q.; Yu, Z.; Gao, X.; Pan, W.; Wan, X.; Tang, B. Nuclear-Targeted Photothermal Therapy Prevents Cancer Recurrence with Near-Infrared Triggered Copper Sulfide Nanoparticles. *ACS Nano* **2018,** *12*, 5197-5206.

29. Pramanik, S. K.; Sreedharan, S.; Singh, H.; Green, N. H.; Smythe, C.; Thomas, J. A.; Das, A. Imaging Cellular Trafficking Processes in Real Time Using Lysosome Targeted Up-Conversion Nanoparticles. *Chem. Commun.* **2017**, *53*, 12672-12675.

30. Lu, S.; Tu, D.; Hu, P.; Xu, J.; Li, R.; Wang, M.; Chen, Z.; Huang, M.; Chen, X. Multifunctional Nano-Bioprobes Based on Rattle-Structured Upconverting Luminescent Nanoparticles. *Angew. Chem. Int. Ed.* **2015**, *54*, 7915-7919.

31. Li, L. L.; Zhang, R.; Yin, L.; Zheng, K.; Qin, W.; Selvin, P. R.; Lu, Y. Biomimetic Surface Engineering of Lanthanide-Doped Upconversion Nanoparticles as Versatile Bioprobes. *Angew. Chem. Int. Ed.* **2012,** *51*, 6121-6125.

32. Fan, W.; Bu, W.; Shi, J. On the Latest Three-Stage Development of Nanomedicines Based on Upconversion Nanoparticles. *Adv. Mater.* **2016**, *28*, 3987-4011.

33. Li, W.; Wang, J.; Ren, J.; Qu, X. Near-Infrared Upconversion Controls Photocaged Cell Adhesion. *J. Am. Chem. Soc.* **2014**, *136*, 2248-2251.

34. Liu, X.; Deng, R.; Zhang, Y.; Wang, Y.; Chang, H.; Huang, L.; Liu, X. Probing the Nature of Upconversion Nanocrystals: Instrumentation Matters. *Chem. Soc. Rev.* **2015**, *44*, 1479-1508.

35. Yang, Y.; Aw, J.; Xing, B. Nanostructures for NIR Light-Controlled Therapies. *Nanoscale* **2017**, *9*, 3698-3718.

36. Liu, F.; He, X.; Lei, Z.; Liu, L.; Zhang, J.; You, H.; Zhang, H.; Wang, Z. Facile Preparation of Doxorubicin-Loaded Upconversion@ Polydopamine Nanoplatforms for Simultaneous *In Vivo* Multimodality Imaging and Chemophotothermal Synergistic Therapy. *Adv. Healthc. Mater.* **2015**, *4*, 559-568.

37. Xu, J.; Kuang, Y.; Lv, R.; Yang, P.; Li, C.; Bi, H.; Liu, B.; Yang, D.; Dai, Y.; Gai, S.; He, F.; Xing, B.; Lin, J. Charge Convertibility and Near Infrared Photon Co-Enhanced Cisplatin Chemotherapy Based on Upconversion Nanoplatform. *Biomaterials* **2017**, *130*, 42-55.

38. Ai, X. Z.; Ho, C.; Aw, J.; Attia, A.; Mu, J.; Wang, Y.; Wang, X.; Wang, Y.; Liu, X.; Chen, H.; Gao, M.; Chen, X.; Yeow, E. K.; Liu, G.; Olivo, M.; Xing, B. *In Vivo* Covalent Cross-Linking of Photon-Converted Rare-Earth Nanostructures for Tumor Localization and Theranostics. *Nat. Commun.* **2016**, *7*, 10432.

39. Zhang, Y.; Zhan, X.; Xiong, J.; Peng, S.; Huang, W.; Joshi, R.; Cai, Y.; Liu, Y.; Li, R.; Yuan, K. Temperature-Dependent Cell Death Patterns Induced by Functionalized Gold Nanoparticle Photothermal Therapy in Melanoma Cells. *Sci. Rep.* **2018**, *8*, 8720.

40. Parsell, D.; Lindquist, S. The Function of Heat-Shock Proteins in Stress Tolerance: Degradation and Reactivation of Damaged Proteins. *Annu. Rev. Genet.* **1993**, *27*, 437-496.

41. Åkerfelt, M.; Morimoto, R. I.; Sistonen, L. Heat Shock Factors: Integrators of Cell Stress, Development and Lifespan. *Nat. Rev. Mol. Cell Bio.* **2010**, *11*, 545.

42. Nagy, E.; Balogi, Z.; Gombos, I.; Åkerfelt, M.; Björkbom, A.; Balogh, G.; Török, Z.; Maslyanko, A.; Fiszer-Kierzkowska, A.; Lisowska, K. Hyperfluidization-Coupled Membrane Microdomain Reorganization Is Linked to Activation of the Heat Shock Response in a Murine Melanoma Cell Line. *Proc. Natl. Acad. Sci.* **2007**, *104*, 7945-7950.

43. Urban, P.; Kirchner, S. R.; Mühlbauer, C.; Lohmüller, T.; Feldmann, J. Reversible Control of Current across Lipid Membranes by Local Heating. *Sci. Rep.* **2016**, *6*, 22686.

44. Palankar, R.; Pinchasik, B.-E.; Khlebtsov, B. N.; Kolesnikova, T. A.; Möhwald, H.; Winterhalter, M.; Skirtach, A. G. Nanoplasmonically-Induced Defects in Lipid Membrane Monitored by Ion Current: Transient Nanopores *versus* Membrane Rupture. *Nano. Lett.* **2014**, *14*, 4273-4279.

45. Koide, R.; Nishimura, S. I. Antiadhesive Nanosomes Facilitate Targeting of the Lysosomal GlcNAc Salvage Pathway through Derailed Cancer Endocytosis. *Angew. Chem. Int. Ed.* **2019**, *131*, 14655-14660.

46. Pérez-Hernández, M.; del Pino, P.; Mitchell, S. G.; Moros, M.; Stepien, G.; Pelaz, B.; Parak, W. J.; Gálvez, E. M.; Pardo, J.; de la Fuente, J. s. M. Dissecting the Molecular Mechanism of Apoptosis during Photothermal Therapy Using Gold Nanoprisms. *ACS Nano* **2015**, *9*, 52-61.

47. Cirman, T.; Orešić, K.; Mazovec, G. D.; Turk, V.; Reed, J. C.; Myers, R. M.; Salvesen, G. S.; Turk, B. Selective Disruption of Lysosomes in HeLa Cells Triggers Apoptosis Mediated by Cleavage of Bid by Multiple Papain-Like Lysosomal Cathepsins. *J. Biol. Chem.* **2004**, *279*, 3578-3587.

Chapter 3. Specific Cell Membrane Metabolic Staining Through Proteolytic Furin Response

3.1 Introduction

Cell surface receptors are the key regulators of cellular interaction with the microenvironment, cell-cell communication, and intracellular signaling pathways. Different cell types with distinguishable genome sequences display variation in cell surface components. These membrane receptors have been extensively targeted for specific recognition of particular diseases, precise therapeutic agent delivery, and minimum side effect treatment strategies. Popular receptors such as human epidermal growth factor receptor 2 (HER2/neu), which is overexpressed on some breast cancer cell membrane has been used for the development of cancer targeting drugs or nanoparticles.[1, 2] However, solely relying on the different levels of such receptors sometimes constrains their applications since higher natural expression of them only can observed in some cell lines and some normal cells also expressed certain populations of the similar receptors. To enable significant targeted cell monitoring, an artificial method needs to involve in constructing the cell membrane with amplified receptors using gene transfection method.[3,4] However, such a stringent technical method hurdles the translational application of therapeutic agents which normally also come with many potential detrimental effects and nonspecific gene delivery.[5] Instead of increasing the level of receptors, protein modification with additional functional moieties can also be introduced into the cell by using mutant aminoacyl-tRNA synthetases and suppressor tRNAs.[6] Subsequently, extracellular materials can be recruited into the cell membrane by chemical reactions, mimicking the receptors interaction. Nevertheless, this strategy normally confronts with sophisticated insertion of gene and tRNA synthetase conduction. Although promising and

pivotal, efficient modification of the extracellular membrane still meets bundle of challenges, requiring further investigation and developments.

In addition, other cell surface components can also be considered to provide innovative cell surface modification. Glycoengineering is one of prominent candidates employing the abundance of sugars covering almost all over the cell surface.[7] The metabolic glycoengineering technique exploits process of the unnatural glycans mimicking mannosamine, galactosamine, fucose, and sialic acid as precursors for the exogenous generation of chemically targeted cell surface.[8,9] Particularly, *N*-acetylmannosamine (ManNAc) undergoes the sialic acid biosynthesis pathways which is linked at the non-reducing termini of cell-surface glycans. *N*-acetylgalactosamine (GalNAc), and *N*-acetylglucosamine (GlcNAc) participate in uridine diphosphate (UDP) Golgi compartment transportation for eventual conjugation on glycoconjugates. Fucose shares the similar process after being conjugated to guanosine diphosphate (GDP) by fucokinase and fucose-1-P guanylyltransferase. Straightforward tagging of the live cell can subsequently be achieved by applying bioorthogonal moieties for reagent-free click chemistry. Compared to conventional active targeting strategies, metabolic sugar labelling with dynamic process of unnatural sugars internalizing, metabolizing, and expressing continuously offers many advantages. First, the higher density of chemically mediated tags can be obtained from the ubiquitous and abundance of glycans on the glycoproteins covering thick layer outside the cell which is much higher than the normal receptor proteins. Secondly, small molecules for simple bioorthogonal reactions generate a site-specific targeting with minimum impairment of the natural protein properties compared to large-sized antibodies. Together, it offers opportunities to conveniently construct and deliver the drugs or nanoparticles into targeted cells by varying the ligand density and linker chemistries. Thirdly, the method is considered as less

immunogenic compared with other methods, especially when applying *in vivo*. Additionally, the click chemistry for covalent bondings between the cell surface and therapeutic agents makes the system more stable and promises long term cell membrane mediation, suitable for the time-resolve investigations and applications.

One of the prominent unnatural sugars that are popularly used for the cell metabolic labelling is Tetraacetyl-*N*-azidoacetylmannosamine (Ac_4ManAz).[10] The formation of the open chain aldehyde form of azidomannosamine at the C1 position is critical in the metabolic process since it directly determines subsequent downstream reactions. Replacing the anomeric acetyl group (C1–OAc) of Ac_4ManAz with a protective ether bond can inhibit the labelling of the sugar with the cell membrane glycoproteins. Therefore, release of the ether bond caged Ac_4ManAz analogs can be monitored for the controllable trigger-responsive targeting.[11-13] This uncaging strategy is to eliminate the biggest drawback of the metabolic glycoengineering and offer cell selective targeting of therapeutic reagents.

Herein, we developed a furin cleavable peptide-substrate caged metabolic precursor that can be specifically cleaved in the cytoplasm of the targeted cells. Furin is ubiquitously expressed within the endocytic, Golgi complex as well as the cellular surface which functions as an activator of multiple proproteins and triggers various pathological conditions and progressions of the cells.[14-16] Especially in degenerative disease such as cancer, furin was found to be overexpressed in the head, neck, breast and non-small cell lung carcinomas.[17,18] The furin specific peptide caged for metabolic precursors consist of three components, a furin specific peptide moiety (Arg-Val-Arg-Arg, RVRR) with enhanced cellular uptake functions, a self-immolative linker (paminobenzyloxycarbonyl) which plays as a spacer linker, and a metabolic precursor of triacetylated N-azidoacetyl-d-mannosamine (Ac_3ManNAz). As shown in **Scheme 1**, the targeted cells uptake and cleavage the furin peptide moiety and release the

free azide sugar after self-immolation of the linker. The unnatural sugars are subsequently go through metabolic processes to express the clickable azide functional group on the cancer cell surface. The conjugated N_3 can therefore easily be labelled with DBCO-Cy3 which offer efficient, stable and uptake-caring free of therapeutics agent on selective cell manner.

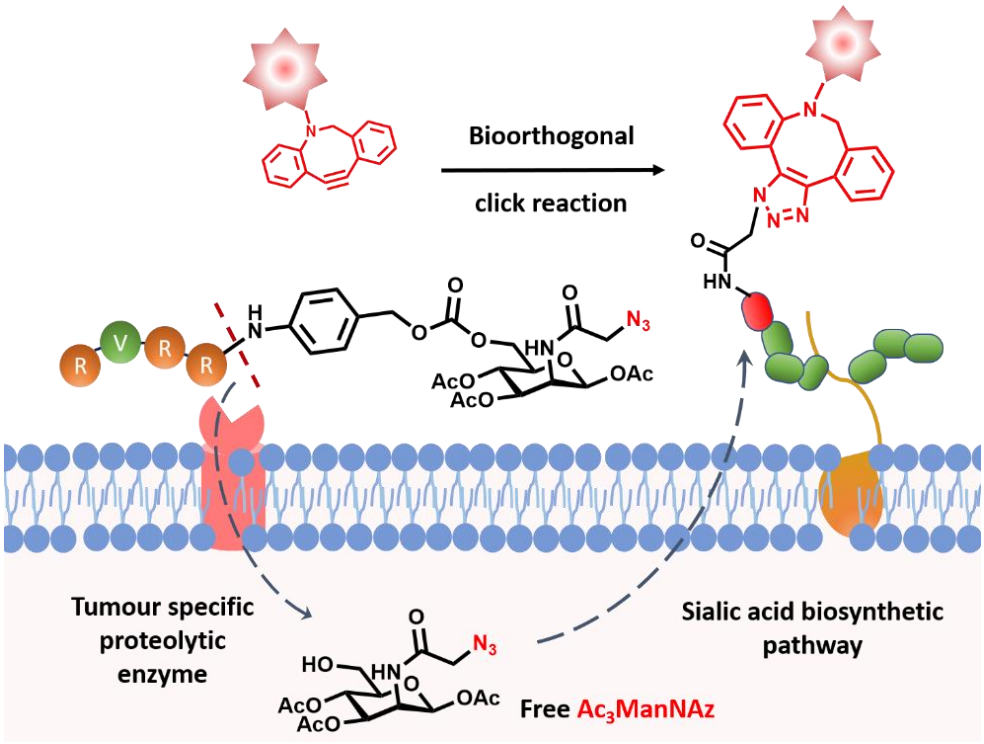

Scheme 1. Illustration of furin-specific hydrolysis and intrinsic metabolism of the precursor (PMAz) in tumor cell, followed by staining of exogenous unnatural glycan with DBCO-Cy3 via bioorthogonal 'click' reaction.

3.2 Results and discussion

To obtain tumour specific metabolic precursor for the cell membrane targeting, we prepared furin cleavable peptide by solid phase synthesis with a self-immolative linker conjugated on the metabolite, Ac_3ManNAz (**Scheme 2**). The product was purified by reverse phase HPLC

with gradient mobile phase and characterized by LC-MS with the electrospray ionization mass spectrometry.

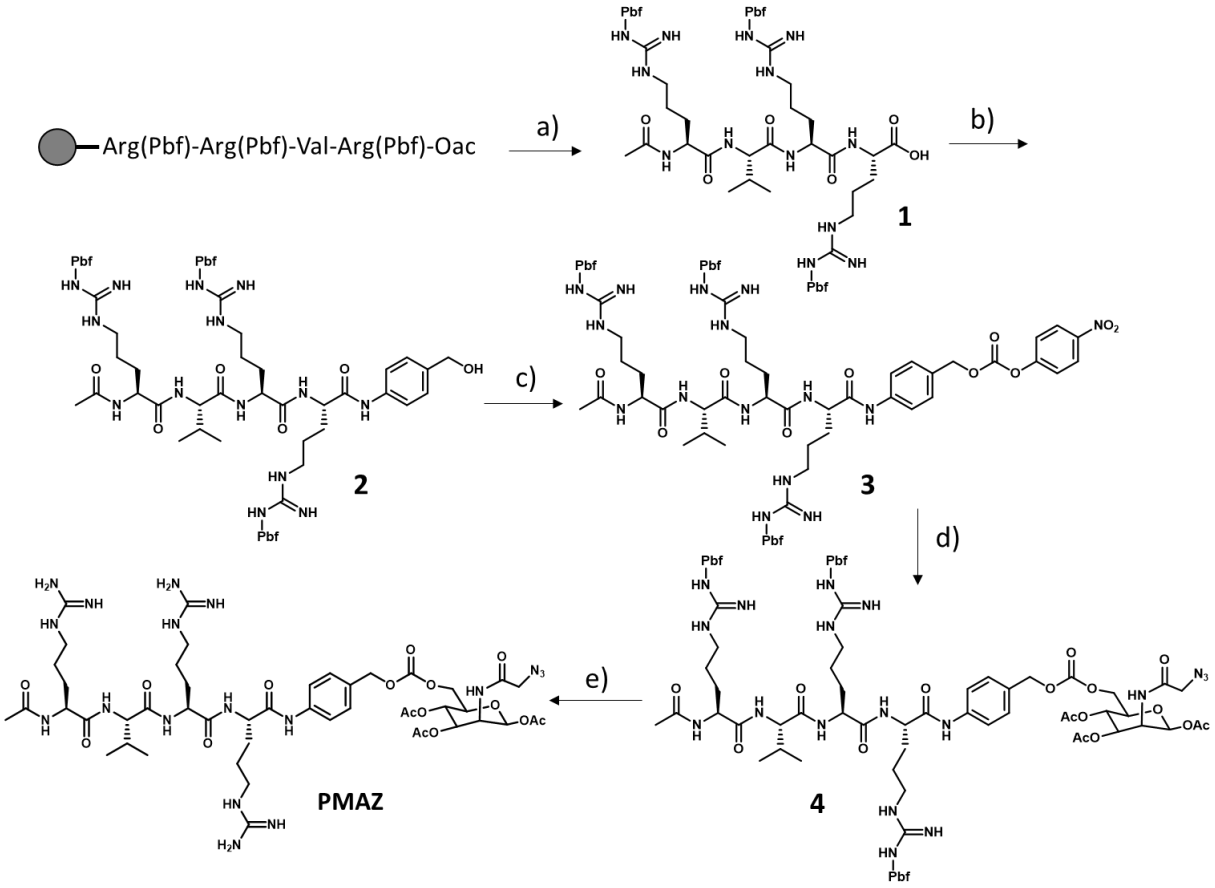

Scheme 2: Synthetic route for PMAz. a) 2% TFA in CH_2Cl_2; b) *p*-aminobenzyl alcohol, EEDC in DMF, 4 h; c) *p*-Nitrophenyl chloroformate/TEA, overnight in DCM; d) Ac3ManNAZ, DMAP, overnight; e) 95% TFA/2.5% TIPS/2.5% H_2O.

Subsequently, the furin responsive properties of the PMAZ was examined using LC-MS analysis method. After incubation of the compound with furin enzyme at 37 ℃ for 12 h, a new peak of free Ac_3ManNAz was observed, confirming by LC-MS (**Figure 1A**). For enzyme responsive metabolic sugar labelling of the furin-overexpressed cancer cells, the PMAZ was incubated with the breast cancer cells, MDA-MB-468, at 12 h, 24 h, 48 h, 96 h at

the concentration of 5 μM. After that, the treated cells were washed and incubated with DBCO-Cy3, a click moiety fluorescent dye. Due to specific activity of the DBCO with the azide functional group, successful expression of azide sugar on the tumour cells surface was detected by monitoring emission from the fluorescent dye. Results from **Figure 1B** have shown that, conjugations of the unnatural sugars on the cell membrane gradually increased in time dependent manner which peaked up at 48 h with the highest fluorescence intensity. Longer incubation of the labelling reagent did not show higher expression intensity. Possibly because of the continuous cell growth and division which reduced the azide sugar content in each individual cell. The expression of the artificial sugar on the cancer cell membrane was concentration dependent. As illustrating in **Figure 1C**, after incubating with different concentrations of our compound for 48 h, the number of azide group on the cell membrane increased with increasing concentration of PMAZ. From the screening results for the incubation condition, we conclude that the period of 48 h under concentration 10 μM is optimal for maximum cellular labelling of the unnatural sugar with our designed substance.

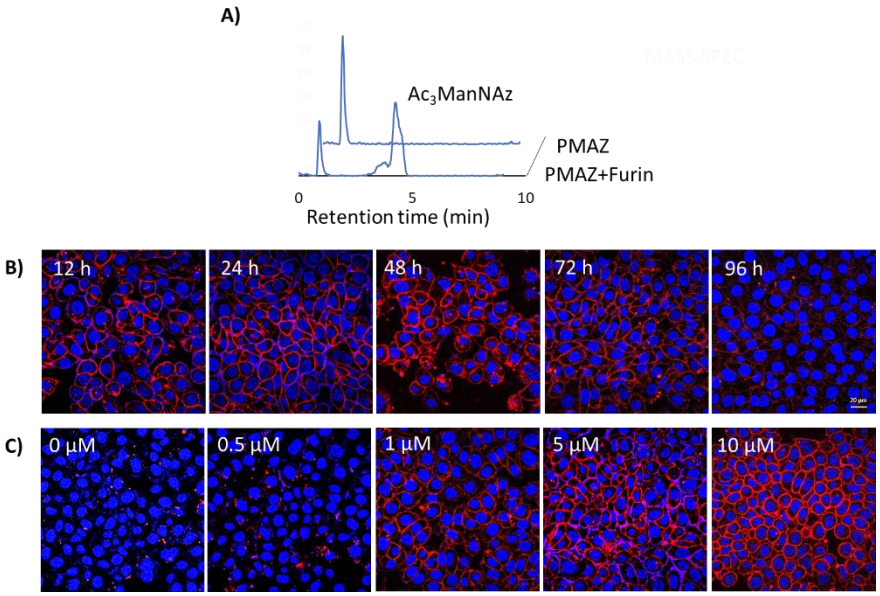

Figure 1: **A**) Enzyme cleavage of PMAZ to release free Ac_3ManNAz. **B**) Time-dependent confocal microscopy fluorescence imaging of azide groups on the surface of cells in vitro (t = 0 when starting to add PMAZ). The MDA-MB-468 cells were treated with PMAZ (5 μm) followed by DBCO-Cy3 (1μM). **C**) Dose-dependent fluorescence imaging experiments. MDA-MB-468 cells were treated with PMAZ at different concentrations. Red=DBCO-Cy3 channel (λ_{ex}: 560 nm, λ_{em}: 610/50 nm; blue=Hoechst channel (λ_{ex}: 401 nm, λ_{em}: 450/50 nm)

Specificity of the furin responsive sugar labelling precursors was carefully examined using a furin inhibitor. The inhibitor with a peptidyl chloromethylketone structure binds irreversibly to the catalytic site of furin and blocks its activities. We pre-treated the MDA-MB-468 cells with the inhibitor for 24 h. After that, the cells were incubated with PMAZ for another 48 h and expression of the azide sugar on the cell membrane was tested by staining with DBCO-Cy3 dye. Results from confocal images showed low fluorescent signals compared to cells without the inhibitor treatment (**Figure 2A**). Meanwhile cells treated with free Ac_3ManNAz in the presence of the inhibitor showed minimum interference of the expression which was confirmed by the similar level of fluorescence signals detected from confocal microscope. It was consolidated by the flow cytometry method for quantifying the fluorescence signal in large number of cells with around 10-fold higher in intensity (**Figure 2B**). This observation further confirmed that the furin enzyme overexpression is necessary for the cleavage and release of the metabolic sugar for eventual labelling the cell membrane.

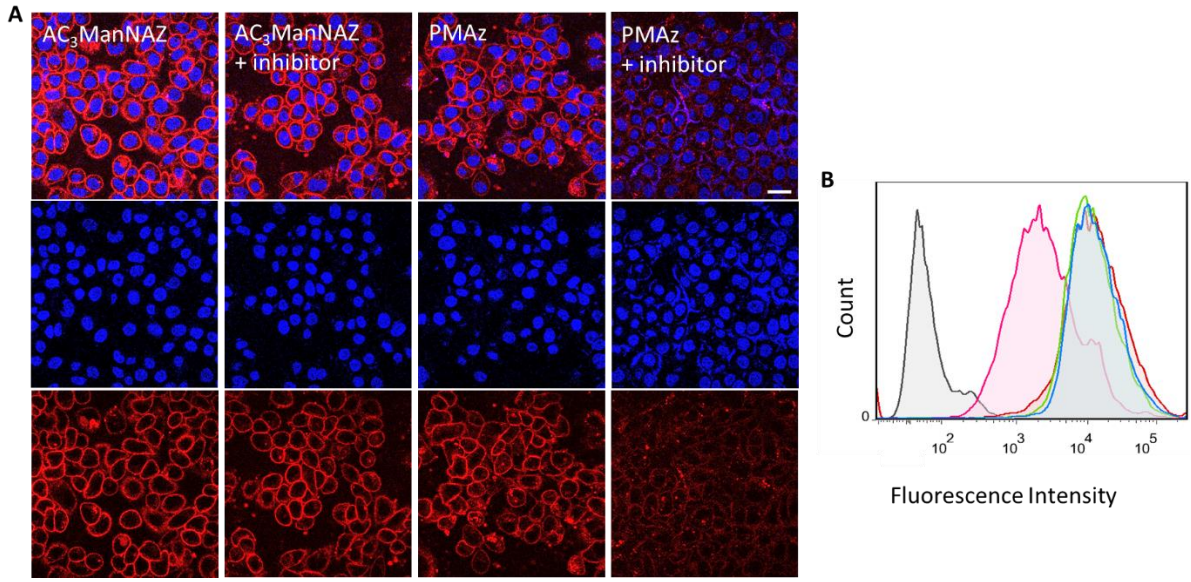

Figure 2. Furin-specific incorporation of azide as a chemical receptor on MDA-MB-468 cells M. A) Confocal microscopy images of PMAZ, Ac_3ManNAz and furin inhibitor treated MDA-MB-468. Azide groups were labelled with DBCO-Cy3 for visualization. The MDA-MB-468 cells were treated with Furin inhibitor for 24 h before treatment with PMAZ and Ac_3ManNAz for the inhibition of Furin enzyme activity. Red=DBCO-Cy3 channel (λ_{ex}: 560 nm, λ_{em}: 610/50 nm; blue=Hoechst channel (λ_{ex}: 401 nm, λ_{em}: 450/50 nm) Scale bar: 20 µm. B) Flow cytometric analysis of Cy3 incorporation amount on MDA-MB-468 cells after metabolic labeling with PMAZ, Ac_3ManNAz with or without furin inhibitor.

To further evaluate the specificity of cancer cell targeting, we tested the compound activities in different cell lines that overexpressed the furin enzyme such as U251, MCF-7 as well as cell with minimum furin expression namely Lovo. It is obvious from **Figure 3** that, free Ac_3ManNAz induces relatively similar intensity after staining the azide sugars with DBCO-Cy3. These results indicate that the sugar metabolic process is ubiquitous in all the tested cell lines. However, the caging PMAZ only induced strong fluorescent signal in the Furin-overexpressed cell lines, but not in Lovo. From the results we can conclude that the expression of the unnatural sugar is strongly corelated with the expression and activity of the

furin enzyme in the living cells. Therefore, the PMAZ can offer specific method to generate the free Ac_3ManNAz with chemical receptor that can facilely visualized by biorthogonal click reaction of the DBCO-fluorescent dye.

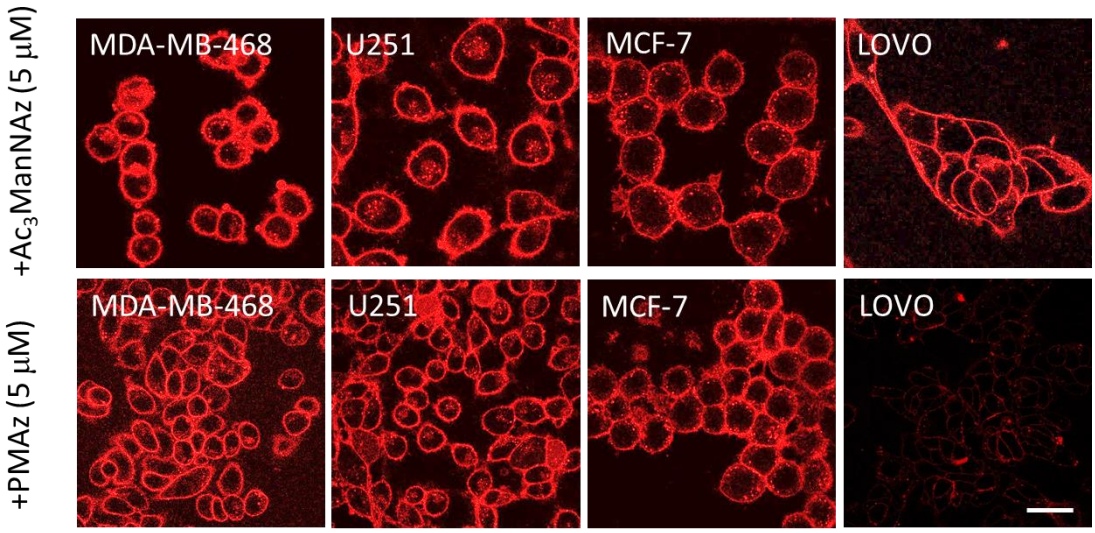

Figure 3. Confocal microscopy images of PMAZ-treated MDA-MB468, MCF7, U251, Lovo cells. Azide groups were labelled with DBCO-Cy3 for visualization. Red=Cy3 channel. Scale bar: 20 μm.

Importantly, the targeted labelling of the sugar on the exogenous cell membrane induced a stable labelling of targeted reagents due to conjugated linkages via a click chemistry. This stability was examined through a post-labelling time control test in the MCF-7 cells (**Figure 4**). The fluorescence imaging showed that the linked Cy3 dye can stain the membrane for 24 h with subsequent uptake which may be resulted from the normal cell endocytosis pathway. This labelling strategy therefore can be employed to study the long-term observation and activation of the cell functions after recruiting the therapeutics agent specifically to the cell membrane. As the cell membrane components harness significant roles in cell signaling and cellular interaction with environment and other cells, this stable and convenient method with

the assistance of enzyme specificity as illustrated with Furin enzyme can enhance the development of cellular precision investigation and therapy.

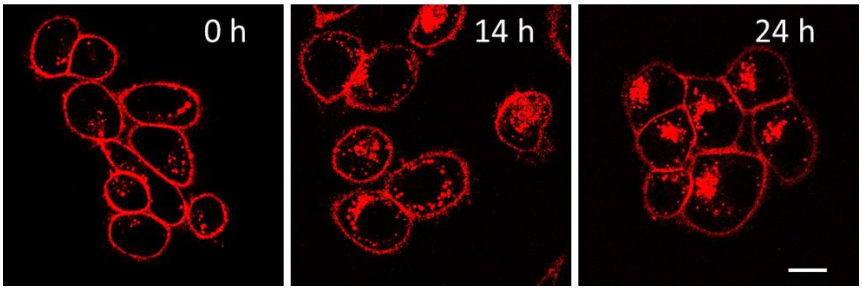

Figure 4: Membrane labelling stability. MCF-7 cell was incubated with PMAZ (5 μM) for 48 h before staining with DBCO-Cy3. The fluorescence intensity of the Cy3 on the cell membrane was monitored after washing the residual dye after incubation (0 h, 14 h, 24 h post-labelling). Red=Cy3 channel. Scale bar: 20 μm.

In conclusion, we designed and developed a precision drug delivery platform through utilizing furin activity in tumor cells. Our design comprised of a furin cleavable peptide-caged metabolic precursor (PMAz) to exogenously generate N_3 groups on the cellular membranes of the tumor cells for subsequent labeling. Based on the preliminary results, we have shown that the PMAz precursor can effectively functionalize N_3 group on furin-expressed tumor cell surface, which can be targeted by DBCO-Cy3 through bioorthogonal "click" reaction. The promising results indicated that furin can be used as a potential biomarker to trigger tumor-specific imaging or drug delivery. Further in vivo investigations are still needed to further consolidate our tumor specific membrane labelling in a complexed microenvironment. The specificity, the simple and long-time conjugating ability of our targeting strategy can be used for more investigation of the cell membrane function monitoring such as glycoprotein functions, membrane receptors, ion channels as well as cell-cell interactions.

3.3 Experiment details

3.3.1. Materials

2-chlorotrityl-chloride resin and all the amino acids were purchased from Bio Basic Asia Pacific Pte Ltd. Triacetylated N-azidoacetyl-D-mannosamine (Ac_3ManNAz) was purchased from FutureChem Co., Ltd. DBCO-Cy3, *p*-aminobenzyl alcohol, HBTU, *N*-Ethyldiisopropylamine (DIPEA), 2-Ethoxy-1-ethoxycarbonyl-1,2-dihydroquinoline (EEDQ), *p*-Nitrophenyl chloroformate were purchased from Sigma-Aldrich. Unless otherwise stated, all commercially purchased chemicals were utilized without any further purificatio. Furin recombinant enzymes were purchased from Biolabs (2000 Unit/mL), The definition is one unit will release 1 pmol of AMC from the fluorogenic peptide Boc-RVRR-AMC (ITS Science & Medical Pte Ltd) per minute at 30 ℃. The furin inhibitor (Dec-RVKR-Cmk) was purchased from Bachem.

3.3.2. Instruments

Reverse-phase HPLC purification was conducted using Shimadzu HPLC system attached with an Alltima C-18 column (10 × 250 mm). Mass spectroscopy (ESI-MS) was conducted using Thermo LCQ Deca XP Max. Nuclear magnetic resonance (NMR) spectroscopy were conducted on Bruker DPX 300 spectrophotometer. Confocal fluorescence imaging of cells was acquired on Carl Zesis LSM 800 confocal laser microscopes. Flow cytometry (FCM) analysis was performed using a BD LSRFortessa™ X-20 cell analyzer (USA).

3.3.3. Synthesis of OAc-RVRR-COOH (1)

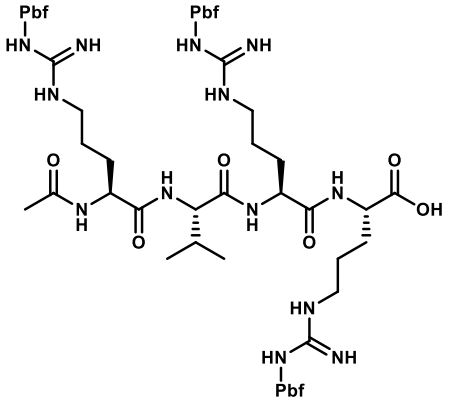

(**1**)

Solid peptide synthesis method was used with 2-chlorotrityl-chloride resin as the solid support. Fmoc-Arg(Pbf)-OH and L-Valine amino acids were loaded with 1.5 eq of the solid support. The coupling reaction was processed under nitrogen gas irritation in addition of HBTU (1.5 eq) and DIPEA (1.5 eq) during 2 h for Valine and 4 h for Arginine. After each step of amino acid linkage, the amine group was deprotected with 20% piperidine in DMF for 20 min. The final peptide sequence was collected by cleaving out from solid resin with 2% TFA in CH_2Cl_2 for 10 min, repeat three times. After concentrating the product in vacuo, the peptide was washed by cold diethyl ether to afford **1** as a white solid. The crude peptide was dissolved in methanol and purified by HPLC to afford a light-yellow solid (yield: 72%). MS (ESI) *m/z* calcd for $C_{64}H_{97}N_{13}O_{15}S_3$ $[M+H]^+$: 1383.64 found: 693.38 $[M+2H]^{2+}$; 462.60 $[M+2H]^{2+}$.

3.3.4. Synthesis of protected OAc-RVRR-PABOH (2)

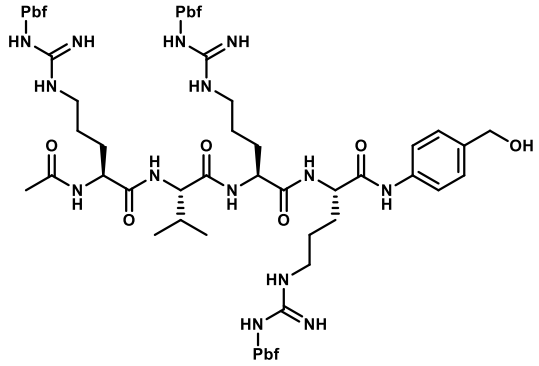

(**2**)

To a solution of **1** (0.42 g, 0.3 mmol) in DMF, *p*-aminobenzyl alcohol (PABOH) (73.8 mg, 0.6 mmol) and EEDQ (148.37, 0.6 mmol) was added and stirred at r.t for 4 h. The product was purified by reverse phased HPLC to obtain **2**. ESI-MS: m/z calcd for $C_{71}H_{104}N_{14}O_{15}S_3$: 1488.70 $[M+H]^+$; found: 745.92 $[M+2H]^{2+}$; 497.53 $[M+3H]^{3+}$.

3.3.5. Synthesis of OAC-RVRR-PABOH-PNP (3)

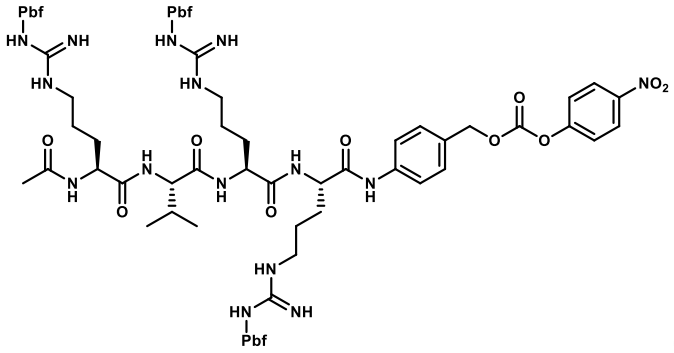

(**3**)

To a solution of **2** (0.074 g, 0.05 mmol) in DCM (1 mL) was added *p*-nitrophenyl chloroformate (PNP) (0.021 g, 0.1 mmol), TEA (42 μL, 0.3 mmol) and stirred overnight at r.t. After the reaction, product was purified by HPLC to afford **3** as a white solid (0.039 g, 47 % yield). ESI-MS: m/z calcd for $C_{78}H_{107}N_{15}O_{19}S_3$: 1653.70 $[M+H]^+$; found: 828.34 $[M+2H]^{2+}$; 552.67 $[M+3H]^{3+}$.

3.3.6. Synthesis of protected PMAz (4)

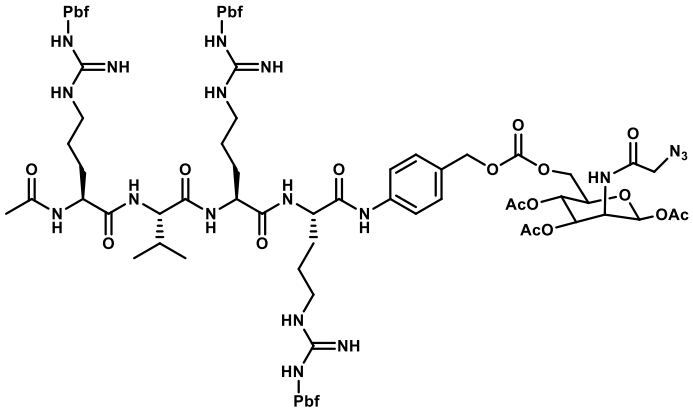

(**4**)

To a solution of **3** (0.02 g, 0.012 mmol) in DMF (500 μL) was added Ac_3ManNAz (9.3 mg, 0.024 mmol) and stirred overnight at r.t. After the reaction, the product was purified by HPLC to attain **4**. ESI-MS: m/z calcd for $C_{86}H_{122}N_{18}O_{25}S_3$: 1902.80 $[M+H]^+$; found: 952.44 $[M+2H]^{2+}$; 635.39 $[M+3H]^{3+}$.

3.3.7. Synthesis of PMAz

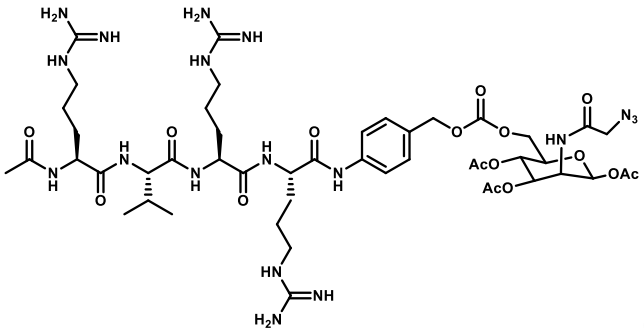

(**PMAZ**)

The Pbf protection **4** was removed by using 95% TFA, 2.5% TIPS and 2.5% H_2O for 2 h. After the reaction, the product was purified by HPLC to attain **PMAz**. ESI-MS: m/z calcd: 1146.55 $[M+H]^+$; found: 575.82 $[M+2H]^{2+}$.

3.3.8. Metabolic glycan labeling on the cell membrane

The cells of Human mammary gland/breast MDA-MB-468 cells (from ATCC) were cultured in DMEM supplemented with 10 % FBS, 100 units mL^{-1} penicillin and 100 μg mL^{-1} streptomycin and maintained in a humidified incubator with 5% CO_2 at 37 °C. Human

colorectal adenocarcinoma LoVo cells (from ATCC) were cultured in F-12K medium supplemented with 10% FBS, 100 units mL^{-1} penicillin and 100 μg mL^{-1} streptomycin and maintained in a humidified incubator with 5% CO_2 at 37 °C. Subsequently, the cells were seeded at a density of 1×10^5 in 35 mm diameter μ-dish plastic bottom (ibidi GmbH) in complete medium and with different concentration of PMAZ or Ac_3ManNAz for at different time indicated at 5% CO_2 and 37ºC. The medium was subsequently replaced with fresh medium containing DBCO-Cy3 (1 μM) for 30 min and washed with medium before adding Hoechst 33342 (1 μM) for 20 min for nucleus staining. The samples were washed before confocal imaging or collected by trypsin for flow cytometry analysis). (Cy3: λex = 561 nm, λem = 585/25 nm, Hoechst: λex = 405 nm, λem = 420/30 nm).

3.4. References

1. Goutsouliak, K.; Veeraraghavan, J.; Sethunath, V.; Angelis, C. A.; Obsborne, C. K.; Rimawi, M. F.; Schiff. R. Towards Personalized Treatment for Early Stage HER2-Positive Breast Cancer. *Nat. Rev. Clin. Oncol.* **2020**, *17*, 233–250.

2. Wang, J.; Xu, B. Targeted Therapeutic Options and Future Perspectives for HER2-Positive Breast Cancer. *Sig. Transduct. Target. Ther.* **2019**, *4*, 34.

3. Sadelain, M.; Rivière, I.; Riddell, S. Therapeutic T Cell Engineering. *Nature* **2017**, *545*, 423–431.

4. Curran, K. J.; Pegram, H.J; Brentjens, R. J. Chimeric Antigen Receptors for T Cell Immunotherapy: Current Understanding and Future Directions. *J. Gene. Med*. **2012**, *14*, 405-415.

5. Bonifant, C.L.; Jackson, H.J.; Brentjens, R.J.; Curran, K.J. Toxicity and Management

in CAR T-cell Therapy. *Mol. Ther. Oncolytics* **2016**, *3*, 16011.

6. Hibodeaux, G. N.; Liang, X.; Moncivais, K.; Umeda, A.; Singer, O.; Alfonta, L. Transforming a Pair of Orthogonal tRNA-aminoacyl-tRNA Synthetase from Archaea to Function in Mammalian Cells. *PLoS ONE* **2010**, *5*, e11263.

7. Kayser, H.; Geilen, C. C.; Paul, C.; Zeitler, R.; Reutter, W. Incorporation of N-acyl-2-amino-2-deoxy-hexoses into Glycosphingolipids of The Pheochromocytoma Cell Line PC 12. *FEBS Lett*. **1992**, *301*, 137–140.

8. Gartner, Z. J.; Bertozzi, C. R. Programmed Assembly of 3-dimensional Microtissues With Defined Cellular Connectivity. *Proc. Natl. Acad. Sci. USA* **2009**, *106*, 4606–4610.

9. Shi, P.; Ju, E.; Yan, Z.; Gao, N.; Wang, J.; Hou, J.; Zhang, Y.; Ren, J.; Qu, X. Spatiotemporal Control of Cell-Cell Reversible Interactions Using Molecular Engineering. *Nat. Commun*. **2016**, *7*, 13088.

10. Jacobs, C. L.; Yarema, K. J.; Mahal, L. K.; Nauman, D. A.; Charters, N. W.; Bertozzi, C. R. Metabolic Labeling of Glycoproteins with Chemical Tags Through Unnatural Sialic Acid Biosynthesis. *Methods Enzymol*. **2000**, *327*, 260-75.

11. Chang, P. V.; Dube, D. H.; Sletten, E. M.; Bertozzi, C. R. A Strategy for the Selective Imaging of Glycans Using Caged Metabolic Precursors. *J. Am. Chem. Soc.* **2010**, *132*, 9516–9518.

12. Shim, M. K.; Yoon, H. Y.; Ryu, J. H.; Koo, H.; Lee, S.; Park, J. H.; Kim, J. H.; Lee, S.; Pomper, M. G.; Kwon, I. C.; Kim, K. Cathepsin B-Specific Metabolic Precursor

for In Vivo Tumor-Specific Fluorescence Imaging. *Angew. Chem. Int. Ed. Engl.* **2016**, *55(47)*, 14698-14703.

13. Wang, H.; Mooney, D. J. Metabolic glycan labelling for cancer-targeted therapy. *Nat. Chem.* **2020**, *12*, 1102–1114.

14. Seidah, N. G.; Prat, A. The biology and therapeutic targeting of the proprotein convertases. *Nat. Rev. Drug. Discov*. **2012**, *11*, 367-83.

15. Dahms, S. O.; Hardes, K.; Becker, G. L.; Steinmetzer, T.; Brandstetter, H.; Than, M. E. X-ray Structures of Human Furin in Complex with Competitive Inhibitors. *ACS Chem. Biol.* **2014**, *9*, 1113–1118.

16. Vankadari, N**.** Structure of Furin Protease Binding to SARS-CoV-2 Spike Glycoprotein and Implications for Potential Targets and Virulence. *Phys. Chem. Lett.* **2020**, *11*, 16, 6655–6663.

17. Mu, J.; Liu, F.; Shafiq, M.; Shi, M.; Lu, L.; Xu, Q.; Liu, B.; Ng, L.; Xing, B. G. Small Molecule FRET Reporter for the Real-time Visualization of Cell-Surface Proteolytic Enzyme Functions. *Angew. Chem. Intl. Ed.* **2014**, *53*, 14357-14362.

18. He, Z.; Thorrez, L.; Siegfried, G.; Meulemans, S.; Evrard, S.; Tejpar, S.; Khatib, A. M.; Creemers, J. W. M. The proprotein convertase furin is a pro-oncogenic driver in *KRAS* and *BRAF* driven colorectal cancer. *Oncogene* **2020**, *39*, 3571–3587.

Chapter 4: Specific Targeting and Degradation of Post-translational Regulation Casein Kinase 2α

4.1. Introduction

Protein balance is a pivotal manifestation channel of cell functions and status which require tightly regulated synthesis and degradation. Tremendous efforts have been placed to interfere that balancing and to investigate the biochemistry of proteins through loss-of-function experiment such as CRISPR-Cas, si/shRNA techniques, or antisense oligonucleotides.[1-3] Besides such systemic delivery of nucleic acid-based protein knockdown agents which may result in delivery and safety challenges, small molecule-based knock-down strategies have also been developed. As a promising candidate in this area, proteolysis targeting chimeras (PROTACs) have recently emerged as new principle of pharmacology.[4] These heterobifunctional degraders simultaneously bind both a target protein and an E3 ubiquitin ligase to facilitate the formation of a ternary complex, thereby promoting the polyubiquitylation of the protein of interest (POI), and its consequent proteasomal degradation.[5] Unlike traditional small-molecule inhibitors, PROTACs offer substoichiometric target occupancy, sustainable pharmacodynamic effects even without constant exposure. Degradation of the full-length protein reduces the possibility of drug resistance through mutations or compensatory protein overexpression and accumulation. The transition from inhibition of proteins to catalytic degradation enables targeting of previously undruggable proteins with reduced drug exposure time and dosage.[6]

One protein kinase, CK2 (casein kinase 2 [CSNK2]) has been implicated in the phosphorylation of hundreds of cellular proteins. This kinase is constitutively active and ubiquitously expressed, making it an important factor in many biological processes (Scheme 1).[7] CK2 exists as a tetrameric complex made up of two catalytic subunits, designated CK2α

(encoded by the CSNK2A1 gene) and CK2α' (encoded by the CSNK2A2 gene), and two regulatory subunits, CK2β.[8] Overexpression of CK2 has been documented in great number of cancers such as lung cancer, breast carcinoma, prostate and kidney cancers, and elevated CK2 activity was found to be associated with tumorigenesis.[9] Thus, CK2 has been regarded as a common denominator of diverse cancer cells and can represent a multi-purpose target for the treatment of different kinds of tumors.[10]

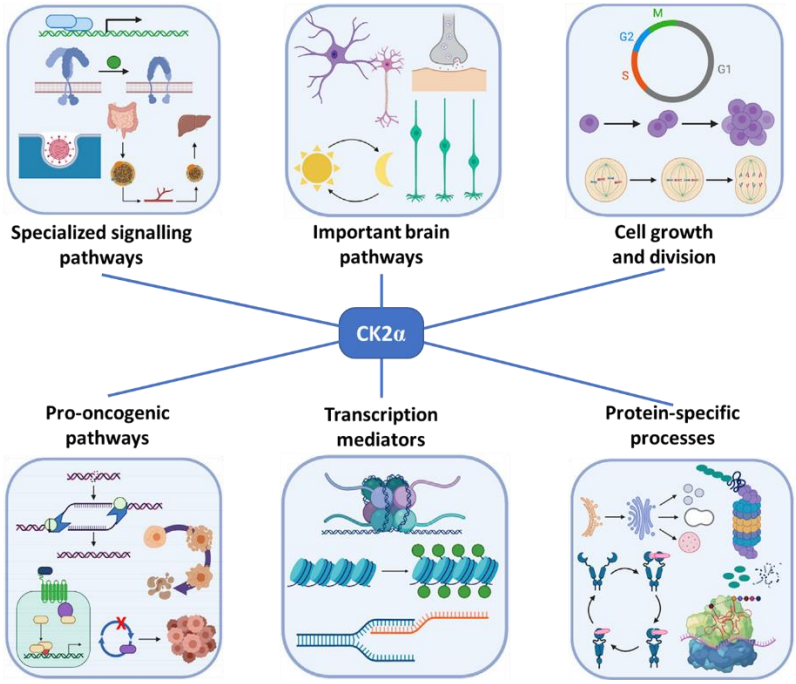

Scheme 1: CK2α plays multiple roles in many biological processes.[7]

In this chapter, we specifically degrade CK2α using PROTAC molecules. Pomalidomide was chosen as a CRBN targeting moiety which is linked with CK2α targeting warhead though different linkers. The efficacy of the molecules in degrading the protein was then evaluated in different cell lines with time and concentration controls.

4.2. Results and discussions

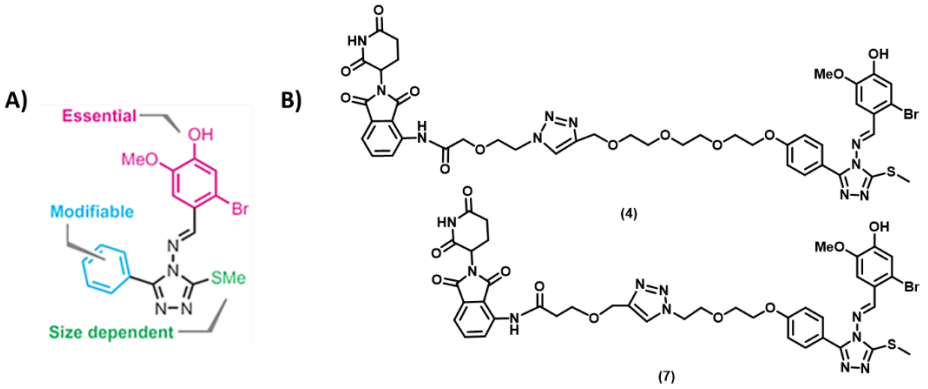

Figure 1. Structure design of heterobifunctional degraders. A) GO289 structure and its modifiable site. B) Structure of GO289 link with pomalidomide via two linker generating compound **4** (longer linker length) and **7** (shorter linker length).

In PROTAC system, a small molecule ligand of protein of interest is connected to a recruiter of ubiquitin E3 ligase which bring them together for ubiquitination and degradation of the interest protein via proteosome pathway. Using PROTAC approach, we initially designed a CK2α degrader based on a recently reported specific inhibitor of CK2α, GO289.[11] Although the bromo guaiacol part in GO289 molecule is essential for the inhibitor activity, the *para* position of the phenyl group is amenable for modification (**Figure 1A**). Therefore, to induce a bivalent degrader, pomalidomide (CRBN ligand) was linked with GO289 at para position of the phenyl group by click reaction with two different linker lengths (**Figure 1B**). The obtained compounds **4** and **7** were then examined for their ability to degrade CK2α protein.

The protein degradation activity of our products showed its time dependence. Immunostaining strategy was used to evaluate the efficient time for the degradation in three different cell lines. Three post-treatment time point of **4** and **7** was recorded, revealing that increasing the time of incubation will leads to higher amount of protein degradation except the case of compound **4** at 30 h in HEK 293T and MCF-7 cells (**Figure 2, 3**).

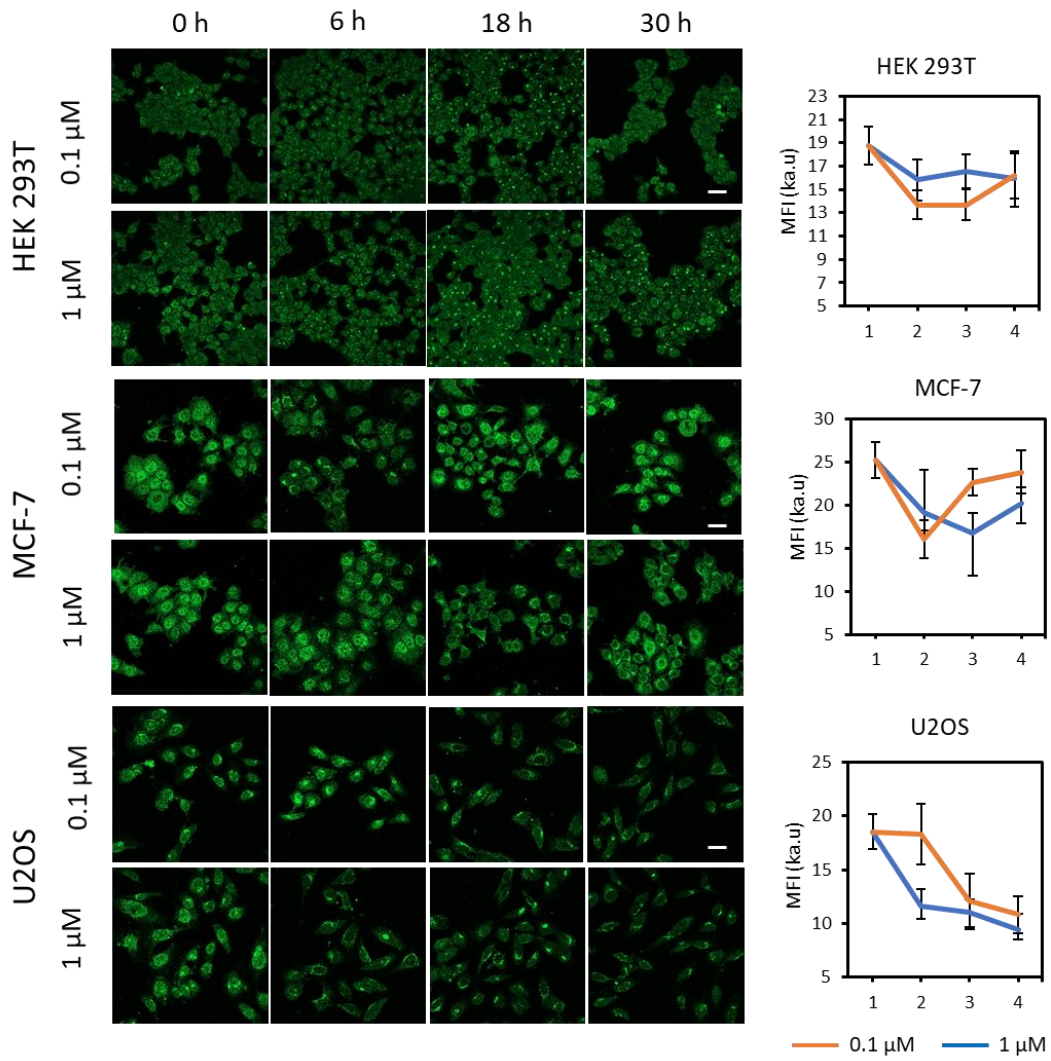

Figure 2: Immunofluorescence staining of time dependent degradation of Casein kinase 2 alpha in different cell lines, HEK293T, MCF-7, U2OS during compound **4** treatment. (1- 0 h; 2-6h; 3-18h; 4-30h). CK2α protein was stained with CK2α primary antibody and detected by Alexa Fluor 488-Goat Anti-Rabbit IgG secondary antibody. Green: Alexa Fluor 488: Ex = 488 nm, Em = 515/30 nm. Scale bar: 50 µm. Mean fluorescence intensity (MFI) of antibody labelled CK2α was reported on the right graphs. Values represent MFI of CK2α in labeled cells + SD (n = 20).

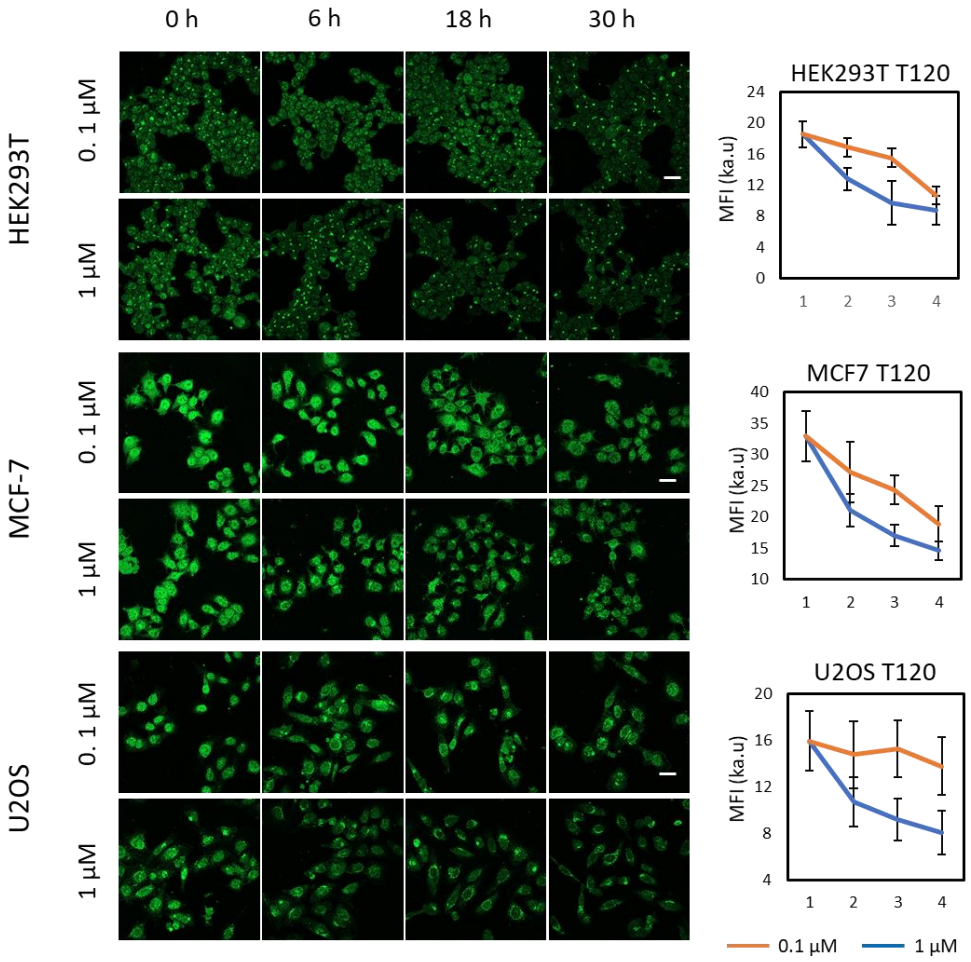

Figure 3. Immunofluorescence staining of time dependent degradation of Casein kinase 2 alpha in different cell lines, HEK293T, MCF-7, U2OS during compound **7** treatment (1- 0 h; 2-6h; 3-18h; 4-30h). Cells after treatment was fixed and stained with CK2a antibody (3 h), then with Alexa Fluor 488-Goat Anti-Rabbit IgG secondary antibody for 30 minutes. Green: Alexa Fluor 488: Ex = 488 nm, Em = 515/30 nm. Scale bar: 50 µm. Mean fluorescence intensity (MFI) was obtained by taking average of fluorescence from 20 cells (n=20). Values represent means + SD.

We evaluated the ability of the two protein degraders by concentration dependent examinations. Cell lines including HEK293T and MCF-7 was incubated with varied

concentrations of **4** and **7** for 24 h (Figure 4). Results from the quantification of fluorescent intensity after immunostaining showing that, compound **7** with shorter linker is generally at higher potent for degradation of CK2α possibly originated from its ability to recruit the protein closer proximity to the E3 ligase. Particularly for HEK 293T cells, **4** generates a maximum degradation of the targeted protein at concentration of around 1 μM with about 32%. Meanwhile, the optimal concentration of **7** is about 60% at a concentration of 10 μM. However, the degradation effects of both substances were reduced in human breast cancer cells line, MCF-7. This reduced efficacy may originate from the less efficient intracellular uptake of the compounds. While the optimum concentration of compound **4** for the highest degradation efficiency is still at around 1 μM with nearly 24%, compound **7** still performed as a better degrader with the amount of protein depletion reached at 44% by using the same 1 μM concentration.

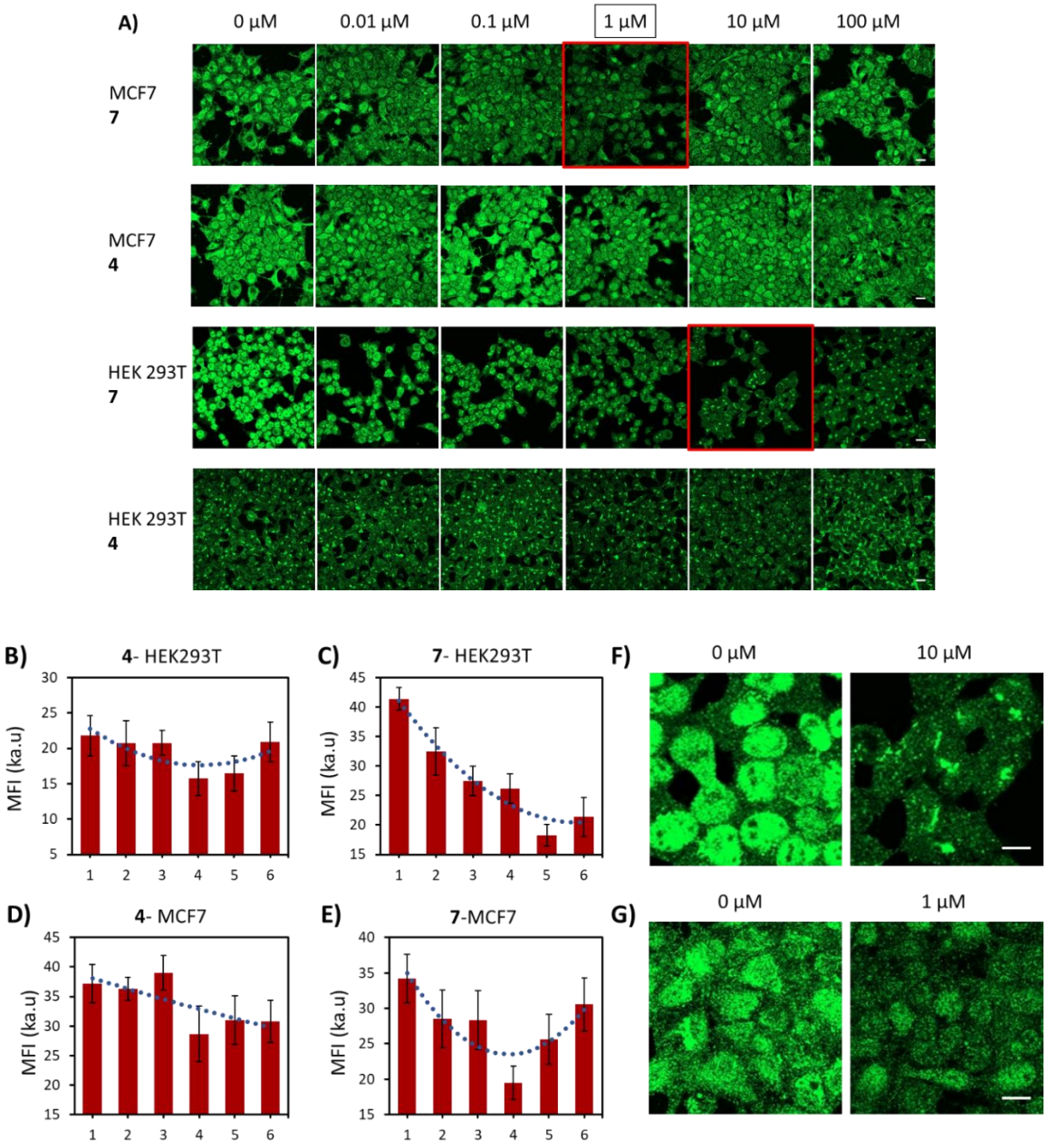

Figure 4: **A**) Immunofluorescence staining of concentration dependent degradation of Casein Kinase 2 alpha in normal (HEK293T) and cancer cell lines (MCF-7) during compound **4** and **7** treatments for 24 h. Mean fluorescent intensity of Alexa Fluor 488 signal in CK2α staining after treatment of HEK293T with **4** (**B**), and **7** (**C**) and MCF-7 with 4 (**D**) and 7 (**E**) for 24 h. (1-0 µM; 2-0.01 µM; 3-0.1 µM; 4-1.0 µM; 5-10 µM; 6-1.0 µM). Optimal condition of compound **7** treatment in HEK293T and MCF-7 was observed at 10 µM and 1 µM, respectively (**F**; **G**). Green: Alexa Fluor 488: Ex = 488 nm, Em = 515/30 nm. Scale bar: 50 µm.

Western blot was then processed to quantify the protein amount after treatment with our CK2α degraders (Figure 5). Although there might be some minor discrepancies in the percentages of depleted protein, similar results were obtained generally. Specifically, both of our degraders showed their ability to induce proteasomal degradation, but the shorter linker length seems to induce better effects. The outcomes suggest that our reagents normally offer best efficiencies at the concentration of around 1 μM to 10 μM. Increase in the concentration of them did not induce any further degradation but made the compounds less potent as degraders, especially in U2OS cell. This is because of the "Hook effect" in which the ternary complexes can only be sufficiently formed with adequate amount of the two protein recruiters. Excessive of a PROTAC reagents induce more separated protein-molecules and E3 ligase-molecules complexes instead of ternary complexes from protein-molecule-E3 ligase. As a result, the protein degradation efficiency is interfered by adding too much bivalent agents in PROTAC. Pomalidomide and the CK2α protein targeting warhead (GO289) showed its inability to degrade the protein themselves.

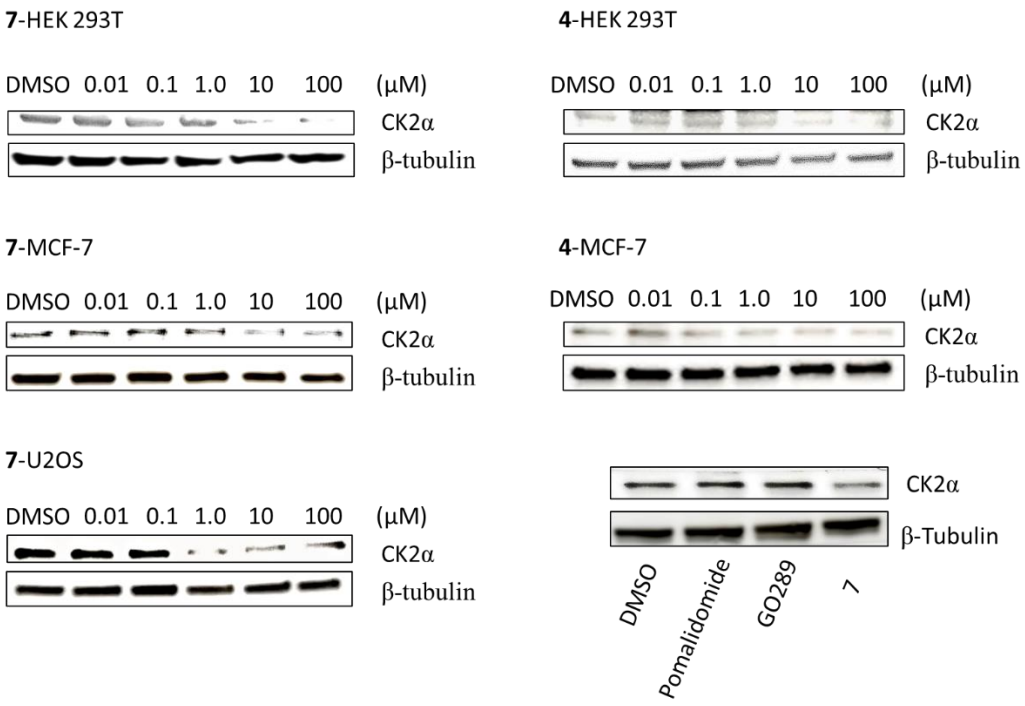

Figure 5. Western blot analysis of CK2α during concentration dependent treatment with **4** and **7** in different cell lines for 24 hours. Pomalidomide and GO289 (10 μM) was treated with HEK-293T cell for 24h and used as negative controls in comparison with compound 7 treatment (10 μM).

We next proceed the protein degradation effect *in vivo* using zebrafish as a study model. As shown in figure 6, the obvious lower level of CK2α protein was observed after treatment of the larva with different concentration of the compound **7** (Figure 6A). The decrease protein level was detected by the lower fluorescent intensity in the zebrafish body after staining the POI with green dye antibody (Figure 6B).

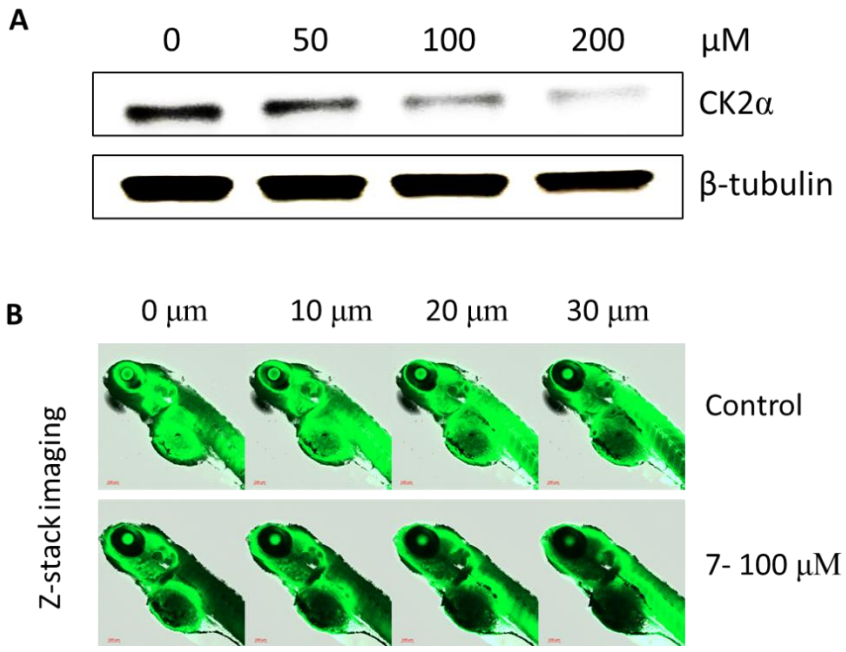

Figure 6. Zebrafish analysis of CK2α protein degradation after treatment with PROTAC molecule **7**. A) Western blot analysis of concentration dependent CK2α degradation in zebrafish lysis after 24 h treatment with **7**. B) Z-stack immunostaining of CK2α in zebrafish after PROTAC compound **7** incubation for 24 h.

In conclusion, considering the importance of CK2α in many cellular processes including cell cycle progression, gene expression, cell growth and differentiation, embryogenesis, circadian rhythms, and apoptosis, we designed heterobifunctional molecules to decrease the level of CK2α *in vitro* and *in vivo*. The different efficacy of our PROTAC molecules suggest that comprehensive consideration need to involve in achieving efficient degraders. Molecule wise, the compounds with the same warheads targeting E3 ligase and POI but with different linkers could provide different performance. The linker length might straightly affect the interaction of the two proteins to induce ubiquitination process for subsequent degradation since the production of polyubiquitin protein results from the close-proximity manner. However, too short of the linker may potentially cause protein crash which affects the efficient binding of

the molecules. Additionally, linker hydrophilicity and flexibility are also noteworthy in designing since it determines the molecule biocompatibility, solubility, and cellular uptake ability. Moreover, our results indicate the high concentration dependence of the PROTAC molecules. Generally, low concentration of PROTAC compound can give significant depletion effect on POI. However, due to the nature of its bifunctional molecules which requires an efficient formation of ternary complexes to action, too high concentration of the degraders might result in “Hook effect” in which saturate formation of binary complexes hinders the performance. Additionally, due to different protein levels and behaviors of the different cell linages, protein degradation of the PROTAC compounds show distinguished actions. Therefore, methods to accurately evaluate the molecule quantity and its functioning still need further investigation. By using this tools, further analysis of CK2α loss-of-function in cellular response and its effect to cell functions need to be studied more in detail in order to target the system to the final goal of therapeutic development.

4.3. Experimental details

4.3.1. Synthesis of compounds

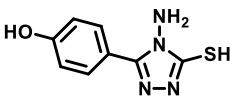

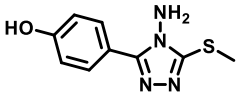

(1)

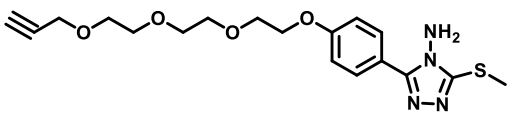

(2)

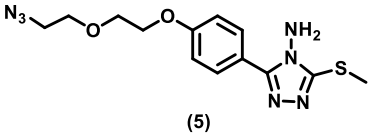

(5)

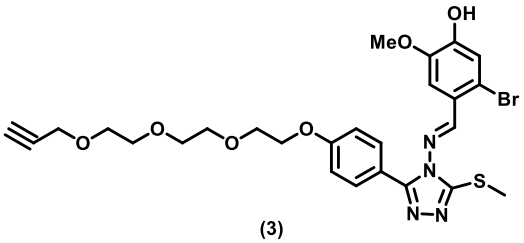

(3)

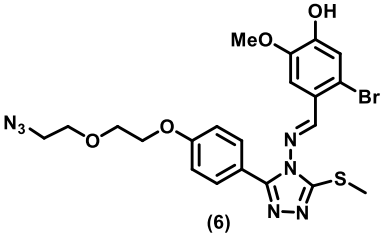

(6)

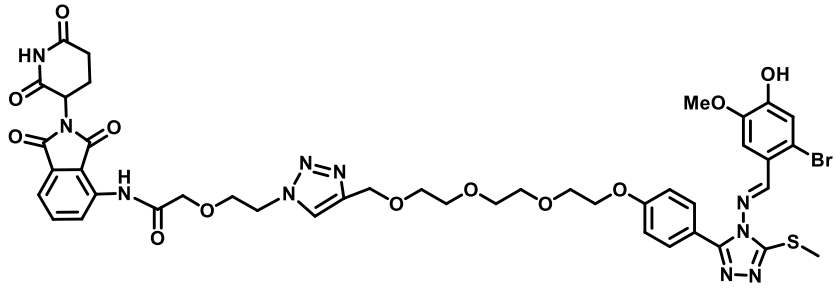

(4)

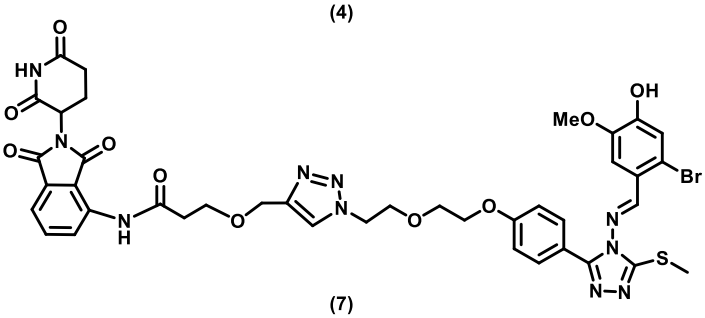

(7)

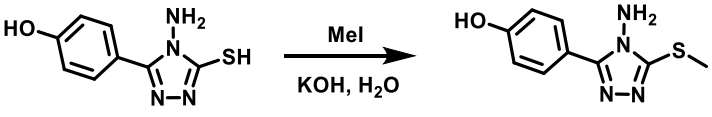

S1 (1)

Synthesis of 1. To a suspension of S1 (500 mg, 2.4 mmol) in H_2O (20 mL) were added potassium hydroxide (148.1 mg, 2.6 mmol, 1.1 equiv) and iodomethane (177.25 mg, 2.6 mmol, 1.1 equiv) at room temperature. After stirring the mixture at room temperature for 14 h, the precipitated solid was filtrated and washed with H_2O to afford 1 (492.4 mg, 92% yield) as a yellow solid. ^{1}H NMR (DMSO*d*6, 400 MHz) δ 8.01-7.95 (m, 2H), 7.54-7.46 (m, 2H), 6.13 (s, 2H), 2.61 (s, 3H); ^{13}C NMR (DMSO-*d*6, 100 MHz) δ 154.5, 154.1, 129.5, 128.5, 127.7, 126.9, 13.7; MS (ESI) *m/z* calcd for $C_{10}H_{13}N_3OS$ [M+H] $^+$: 223.06 found 223.11.

Synthesis of 2.

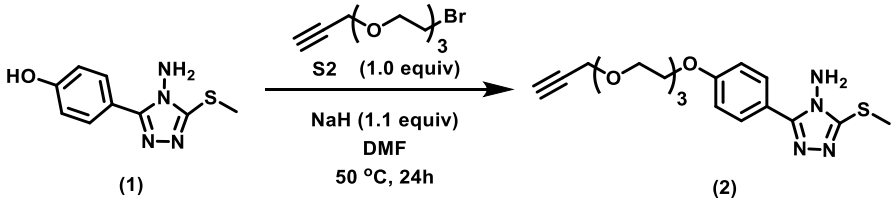

To a solution of 1 (100 mg, 0.45 mmol) in DMF was slowly added NaH (11.9 mg, 0.49 mmol at 0 ℃. After stirring at 30 min at room temperature, a solution of Propargyl-PEG3-bromide (S2) (113 mg, 0.45 mmol) in DMF was added to the mixture at 0 ℃. The reaction was stirred at 60 ℃ for 24 h before being quenched with saturated aqueous NH_4Cl. After that, the mixture was extracted with EtOAc, wash with brine and dry with $NaSO_4$ and the solvent was removed *in vacuo*. The product was then purified by column chromatography with MeOH/DCM (1:20) to obtain a pale-yellow oil compound (56% yield). ^{1}H NMR (300 MHz, MeOD) δ 6.40 (t, J = 8.8 Hz, 2H), 5.55 (d, J = 8.8 Hz, 2H), 2.67 (dd, J = 8.9, 3.4 Hz, 4H), 2.38 – 2.31 (m, 2H), 2.19 (dd, J = 3.7, 1.8 Hz, 2H), 2.15 (d, J = 3.6 Hz, 6H), 1.81 (d, J = 11.6 Hz, 1H), 1.30 (dd, J = 13.2, 10.9 Hz, 1H), 1.16 (d, J = 9.1 Hz, 3H). MS (ESI) *m/z* calcd for $C_{18}H_{24}N_4O_4S$ [M+H] $^+$: 393.15 found 393.31.

Synthesis of 3.

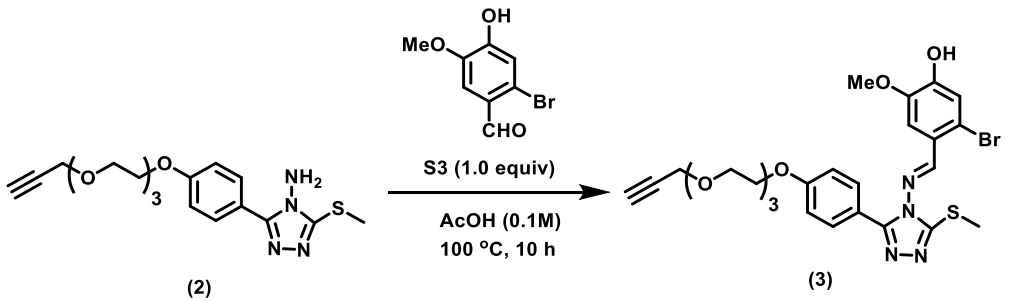

To a solution of **2** (100 mg, 0.26 mmol) and **S3** (60.6 mg, 0.26 mmol) in AcOH was heated at 100 ℃ for 10 h. After removal of the solvent, the mixture was purified by column chromatography with MeOH/ DCM: 1/40. The product was attained in pale yellow viscous oil (73% yield). MS (ESI) *m/z* calcd for $C_{26}H_{29}BrN_4O_6S$ $[M+H]^+$: 606.10 found 607.28.

Synthesis of 4.

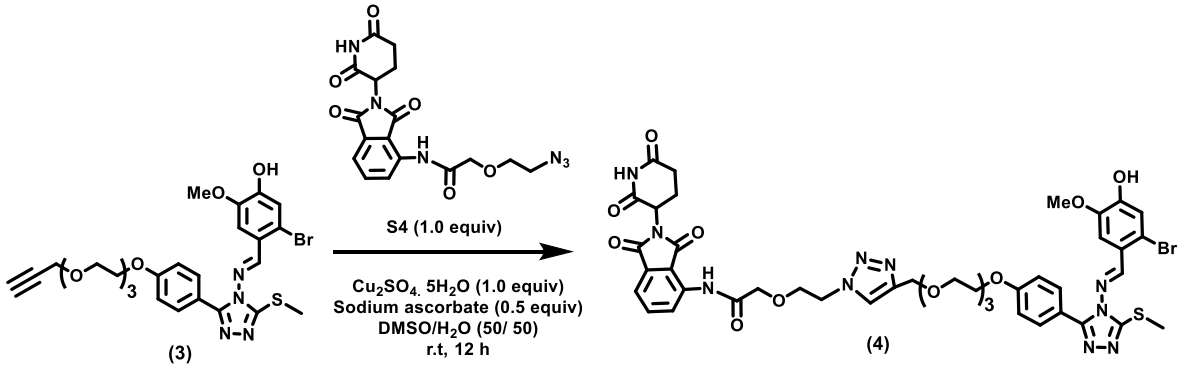

To a solution of 3 (10 mg) in the mixture of DMSO/H_2O (50/50), $Cu_2SO_4.5H_2O$ (4.3 mg, 1.0 equiv) and sodium ascobate (1.7 mg, 0.5 equiv), Pomalidomide-PEG1-azide (S4) was added (6.4 mg, 1.0 equiv). The mixture was then stired under room temperature for 12 h. The crude product was then extracted with brine and DCM before being purified by HPLC to get a pale yellow oil pure product (91% yiled). MS (ESI) *m/z* calcd for $C_{43}H_{45}BrN_{10}O_{12}S$ $[M+H]^+$: 1005.21 found 1007.29.

Synthesis of 5.

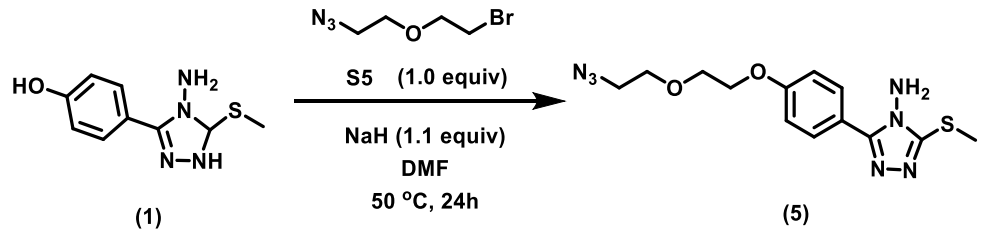

Same procedure as synthesis of **2** was used with using bromo-PEG1-azide (**S5**) instead of **S2**. The white solid product was obtained after being purified by column chromatography with MeOH/DCM (1:20) (72% yield). ^{1}H NMR (500 MHz, $CDCl_3$) δ 7.93 (d, J = 32.1 Hz, 2H), 6.98 (d, J = 8.8 Hz, 2H), 4.72 (s, 2H), 4.17 (d, J = 4.6 Hz, 2H), 3.74 (s, 2H), 3.40 (d, J = 10.0 Hz, 2H), 2.70 (s, 3H), 1.23 (s, 2H). MS (ESI) *m/z* calcd for $C_{13}H_{17}N_7O_2S$ $[M+H]^+$: 336.12. found 336.22.

Synthesis of 6.

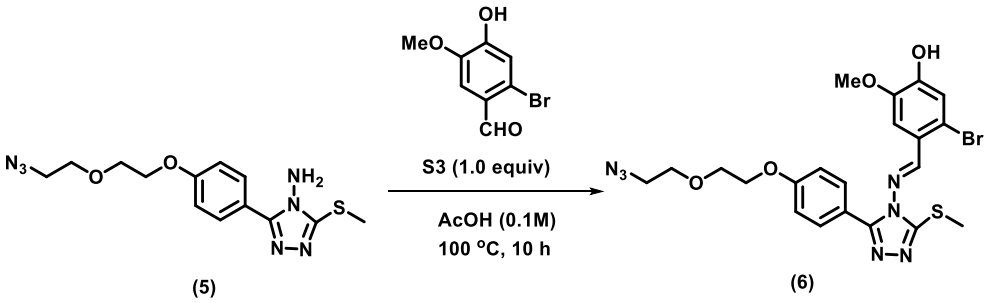

The same procedure for synthesis of **3** was used. White solid product was obtained after being purified by column chromatography with MeOH/DCM (1:20) (85% yield). ^{1}H NMR (500 MHz, MeOD) δ 7.29 (d, J = 1.1 Hz, 1H), 6.17 (d, J = 8.2 Hz, 2H), 6.08 (s, 1H), 5.53 (s, 1H), 5.51 (s, 2H), 2.66 – 2.60 (m, 2H), 2.33 (s, 3H), 2.30 (d, J = 4.1 Hz, 1H), 2.20 – 2.13 (m, 2H), 1.81 (t, J = 4.8 Hz, 2H), 1.15 (s, 3H). MS (ESI) *m/z* calcd for $C_{21}H_{22}BrN_7O_4S$ $[M+H]^+$: 548.06. found 548.15.

Synthesis of 7.

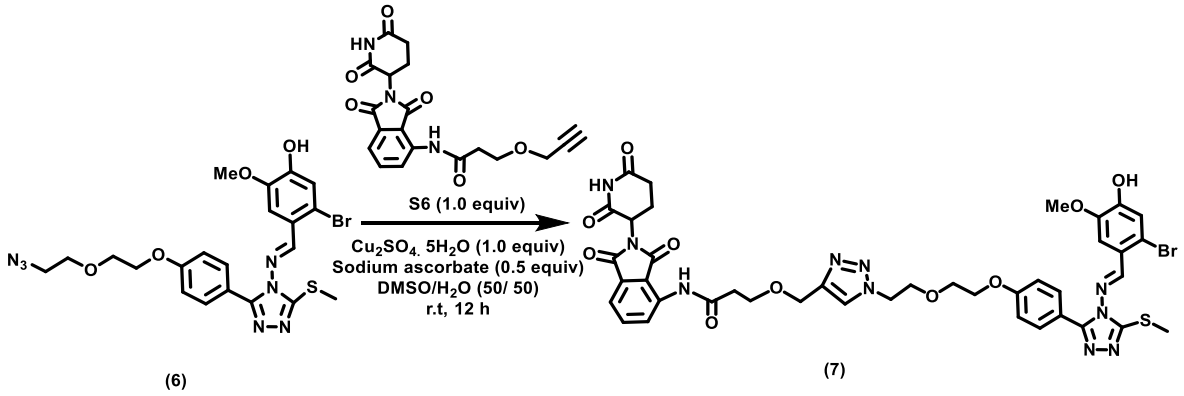

(6) (7)

The same procedure for synthesis of **5** was used with using pomalidomide-PEG1-ankyne (**S6**) instead of **S4.** Pale yealow liquid oil product was obtained after being purified by HPLC (94%). ^{1}H NMR (500 MHz, MeOD) δ 7.28 (s, 1H), 7.06 (d, J = 8.5 Hz, 1H), 6.41 (s, 1H), 6.18 (s, 1H), 6.17 (s, 1H), 6.13 – 6.08 (m, 1H), 6.07 (s, 1H), 5.93 (d, J = 7.2 Hz, 1H), 5.47 (s, 1H), 5.46 (s, 1H), 5.45 (s, 1H), 3.51 (dd, J = 12.7, 5.4 Hz, 1H), 3.06 (s, 2H), 3.01 (d, J = 5.0 Hz, 2H), 2.55 – 2.50 (m, 2H), 2.37 – 2.34 (m, 2H), 2.33 (s, 3H), 2.23 – 2.20 (m, 2H), 2.18 (d, J = 5.7 Hz, 2H), 1.27 (d, J = 13.9 Hz, 1H), 1.20 (s, 1H), 1.16 (s, 1H), 1.16 (s, 3H), 1.12 (d, J = 13.1 Hz, 1H), 1.04 (t, J = 5.7 Hz, 2H), 0.59 (s, 1H). MS (ESI) *m/z* calcd for $C_{40}H_{39}BrN_{10}O_{10}S$ $[M+H]^+$: 931.18, found 931.37.

4.3.2. Immunofluorescence analysis of CK2α protein

Each group of cells with density of 5×10^4 cells in each well of 8-well ibidi-dishes was treated with **4** or **7** at different concentration and time. After treatment, the cells were fixed with 4% paraformaldehyde for 15 minutes, permeabilized with 0.25% Triton™ X-100 for 10 minutes and blocked with 5% BSA for 1 hour at room temperature. The cells were then labelled with CK2α Rabbit polyclonal Antibody (Cell signalling, #2656) in 1% BSA and incubated for 3 hours at room temperature. Subsequently, Alexa Fluor 488-Goat Anti-Rabbit IgG secondary antibody was stained for 30 minutes at room temperature. Nucleus was stained with Hoechst

33342 for 30 minutes at room temperature. The degradation of CK2α protein was visualized with Carl Zeiss LSM 800 microscopes. (Hoechst 33342: Ex = 405 nm, Em = 460/50 nm; Alexa Fluor 488: Ex = 488 nm, Em = 515/30 nm).

4.3.3. Western-blot analysis of CK2α protein

The lysates of each group of cells at different times and concentration treatment of **4** and **7** were collected and centrifuged at 12,000 × g for 20 min at 4 ℃. Protein levels in supernatants were determined using Nanodrop and equalized to the same concentration and boiled for 10 min with SDS-PAGE sample loading buffer before being separated using SDS-PAGE and transferred to the PVDF membrane. The membrane was then blocked with 5% BSA-TBST blocking buffer overnight at 4 ℃. Subsequently, CK2α Rabbit polyclonal Antibody (Cell signalling, #2656) was incubated overnight at 4 ℃ in 1% BSA-TBST buffer. After series of washing, the goat-anti rabbit IGG (H&L) secondary antibody (Abcam) was added and incubated for 1 hour in 1% BSA-TBST. All signals were visualized using AMERSHAM (Image quant 800) system.

4.3.4. Zebrafish experiments

Zebrafish embryos at 24 hpf was incubated with PROTAC compound **7** in E3 medium for 24 h at 28 ℃. After drug treatment, the treated and nontreated control embryos was fixed with 4% formaldehyde for 30 minutes. After a series of washing with PBS, the embryos were blocked with 1% BSA, 0.1 % Triton X-100 at room temperature for 1 h. The embyros were then labelled with CK2α Rabbit polyclonal Antibody (Cell signalling, #2656) in 1% BSA and incubated for 3 hours at room temperature. Subsequently, Alexa Fluor 488-Goat Anti-Rabbit IgG secondary antibody was stained for 30 minutes at room temperature. The degradation of CK2α protein was visualized with Carl Zeiss LSM 800 microscopes by multilayers scanning

of the embryos body. (Alexa Fluor 488: Ex = 488 nm, Em = 515/30 nm). For western blot analysis, the fish embryos after drug treatment were lysis and centrifuge to collect the protein suspension before proceeding to the next steps same as the cell analysis.

4.4. References

1. Pickar-Oliver, A.; Gersbach, C. A. The next generation of CRISPR-Cas technologies and applications. *Nat. Rev. Mol. Cell. Biol.* **2019**, *20*, 490-507.

2. Roberts, T. C.; Langer, R.; Wood, M.J.A. Advances in oligonucleotide drug delivery. *Nat. Rev. Drug. Discov*. **2020**, *19*, 673–694.

3. Hu, B.; Zhong, L.; Weng, Y.; Peng, L.; Huang, Y.; Zhao, Y.; Liang, X. J. Therapeutic siRNA: state of the art. *Signal Transduct. Target. Ther*. **2020**, *5*, 101.

4. Nalawansha, D. A.; Crews, C. M. PROTACs: An Emerging Therapeutic Modality in Precision Medicine. *Cell. Chem. Biol*. **2020**, *27*, 998-1014.

5. Jan, M.; Sperling, A. S.; Ebert, B. L. Cancer therapies based on targeted protein degradation - lessons learned with lenalidomide. *Nat. Rev. Clin. Oncol.* **2021**, *18*, 401-417.

6. Stanton, B. Z.; Chory, E. J.; Crabtree, G. R.; Chemically induced proximity in biology and medicine. *Science*. **2018**, *359*, eaao5902.

7. Wells, C. I.; Drewry, D. H.; Pickett, J. E.; Tjaden, A.; Krämer, A.; Müller, S.; Gyenis, L.; Menyhart, D.; Litchfield, D. W.; Knapp, S.; Axtman, A. D. Development of a potent and selective chemical probe for the pleiotropic kinase CK2. *Cell Chem. Biol*. **2021**, *28*, 546-558.e10.

8. Litchfield, D. W. Protein kinase CK2: structure, regulation and role in cellular decisions of life and death. *Biochem. J*. **2003**, *369*, 1-15.

9. Borgo, C.; D'Amore, C.; Sarno, S.; Salvi, M.; Ruzzene, M. Protein kinase CK2: a potential therapeutic target for diverse human diseases. *Signal Transduct. Target. Ther*. **2021**, *6*, 183.

10. Nitta, R. T.; Bolin, S.; Luo, E.; Solow-Codero, D. E.; Samghabadi, P.; Purzner, T.; Aujla, P. S. Nwagbo G, Cho YJ, Li G. Casein kinase 2 inhibition sensitizes medulloblastoma to temozolomide. *Oncogene* **2019**, *38*, 6867-6879.

11. Oshima, T.; Niwa, Y.; Kuwata, K.; Srivastava, A.; Hyoda, T.; Tsuchiya,Y.; Kumagai, M.; Tsuyuguchi, M.; Tamaru, T.; Sugiyama, A.; Ono, N.; Zolboot, N.; Aikawa, Y.; Oishi, S.; Nonami, A.; Arai, F.; Hagihara, S.; Yamaguchi, J.; Tama, F.; Kunisaki, Y.; Yagita, K.; Ikeda, M.; Kinoshita, T.; Kay, S. A. Itami, K.; Hirota, T. Cell-based screen identifies a new potent and highly selective CK2 inhibitor for modulation of circadian rhythms and cancer cell growth. *Sci. Adv.* **2019**, *23*, eaau9060.

Chapter 5: Nitroreductase Responsive Activation of Molecular Glue for Cell-type Specific Degradation of CK1α

5.1. Introduction

Half a century ago, thalidomide was employed as a medicine for insomnia and morning sickness. However, due to the teratogenicity and its profound limb defects, it was banned quickly later on. Until now, thalidomide and its analogs such as lenalidomide and pomalidomide (IMiDs) are still under intensive investigation and usage as immunomodulators and antineoplastics, especially for multiple myeloma and other B cell malignancies.[1-3] Recently, thalidomide was discovered to specifically bind to a substrate recognition component of the cullin-depenent ubiquitin ligase, cerebron, to inhibit its autoubiquitination activity. It was also shown that IMiDs stabilize the cereblon substrate and therefore cause fin deformations in zebrafish after early drug exposure.[4] Further investigations suggested that myeloma cells induced IMiDs-resistant normally down-regulated cereblon. In contrast, high concentration of cereblon increase IMiDs responsiveness in myeloma cells.[5-7] Those evidence indicated that IMiDs are not only antagonists of cereblon but also the binding of these molecules inhibits the interaction of cereblon to other proteins such as Ikaros family zinc finger proteins 1 and 3 (IKZF1 and IKZF3) in myeloma. These two B cell transcription factors are degraded upon lenalidomide-bound cereblon.[8,9] These two transcription factors play critical roles in B cell development and are highly expressed in B cell malignancies, including myeloma. They are essential for plasma cell as well as mantle cell lymphoma and chronic lymphocytic leukemia development.[10,11] Somatic activation of these two proteins in lymphoblastic leukemia results in accumulation of immature lymphoid progenitor cells.[12] In T cells, IKZF3 mediates the expression of IL-2 gene which is increased by treatment with lenalidomide.[13] The teratogenicity of thalidomide and the activities of

lenalidomide may be regulated by different substrates and cellular lineages dependence. Especially, lenalidomide, which is a highly effective molecule for the treatment of myelodysplastic syndrome (MDS) with deletion of chromosome 5q (del(5q)), also increases ubiquitination and decreases the protein abundance of casein kinase 1A1 (CK1α) in cell and species selective manner. Thalidomide, lenalidomide, and pomalidomide all induce CRL4-CRBN-mediated degradation of IKZF1 and IKZF3, but the subtle differences in chemical structure between these molecules cause dramatic changes in potency. For example, thalidomide induces the degradation of IKZF1 but not CK1α. Thalidomide may have a greater therapeutic window for the treatment of B cell malignancies and other diseases that depend on IKZF1 and IKZF3 but would not be predicted to have activity in del(5q) MDS.[14] These findings provide evidence that thalidomide-related molecules have distinct biological activities, mediated by degradation of distinct sets of substrates, and that these compounds will be the first in a larger class of drugs with therapeutic utility through the targeting of specific proteins for degradation.

Although thalidomide-related molecules can mediate the degradation of specific proteins with high selectivity, but their therapeutic applications are still hindered. One of the reasons for this limitation is that this group of compounds or general molecular glues cannot process under cell selective manner. While these immunomodulatory drugs accurately target to degrade Ikaros proteins or CK1α, relatively abundant types of cells also express high level of these proteins for their normal functioning. Therefore, higher cell selectivity level is prerequisite for the application of the drugs. Remote regulation of the compound was reported by light stimulated uncaging strategy recently. However, spatial resolution of the release can be further enhanced by acquiring the distinct cellular properties including specific enzyme expression. Herein, we report the first-in-class microenvironment responsive method

for the small molecule glue-degradation of proteins which may open a new avenue for larger application of this type of non-drug molecule. In particular, nitroreductase enzyme (NTR) is over-expressed in the tumour or cell under stress such as hypoxia condition. NTR responsive lenalidomide was selected as a proof of concept for the enzyme responsive molecular glue degradation of proteins.

5.2. Results and discussion

Structural studies for a high-affinity complex of CRL4-CRBN, CK1α and lenalidomide reveals a structure restriction of lenalidomide interacting with CK1α and CRBN. CK1α exclusively interacts with the C-terminal domain of CRBN (CTD; residues 317–442), which accommodates lenalidomide in a hydrophobic pocket. CK1α binds CRBN–lenalidomide via a β-hairpin loop in the kinase N-lobe that connects the CK1α β-strands 2 and 3. Residues within this loop interact with the otherwise solvent-exposed phthalimide ring of lenalidomide and contact CRBN residues that surround the lenalidomide binding pocket. Interestingly, Ikaros family transcription factors share a spatial relationship between binding sites on CRBN. A truncated form of human IKZF1 binds $_{N8}CRL4^{CRBN}$ with a higher affinity than CK1α and efficiently displaced CK1α from CRBN. IKZF1 uses a structurally similar β-hairpin loop containing the glycine signature for binding the CRBN–IMiD interface. Thus, CK1α and IKZF1 recruitment are mutually exclusive. Importantly, no interaction between those proteins with CRBN in the absence of lenalidomide. Recruitment of the CK1α and IKZF1 neo-substrates to CRL4CRBN is driven by a surprisingly small 96.8 $Å^2$ compound–protein interface (phthalimide C5–C7) that induces high-affinity binding and occurs through overlapping binding sites on CRBN.[15] A minor modification and difference among IMiDs themselves largely affect the interaction. For example, lenalidomide and pomalidomide

mediates IKZF1 binding to CRBN with comparable affinities, whereas the apparent efficiency was reduced ~1.5-fold in the presence of thalidomide.[15] Only lenalidomide was reported to induce strong interaction and degradation of CK1α due to the different clashes between the carbonyl group at their C3 phthalimide position and the CRBN backbone. We therefore predict that, a small modification of lenalidomide structure would significantly or completely delete the therapeutic effect of the compound. NTR responsive moiety was conjugated on the amine group at the C4 phthalimide position of lenalidomide (Scheme 1).

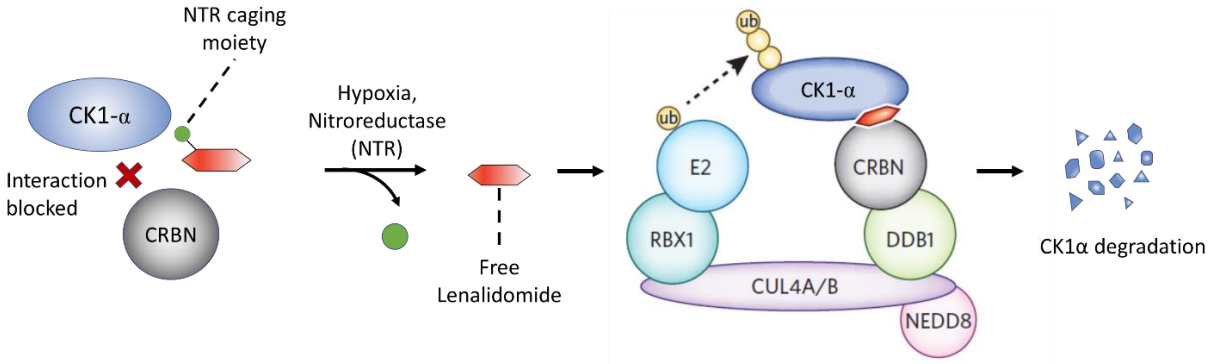

Scheme 1. Nitroreductase responsive uncaging of lenalidomide for selective degradation of CK1α.

Simulation studies suggest that the interaction of CK1α proteins as well as IKZF1 was hindered by NTR-lenalidomide due to the clashes in the interaction of the small molecule with both proteins and CRBN. Both glutarimide and phtalimide part of the compound were not able to position in the active loop of the proteins (Figure 1). This blocking effect suggests that we can potentially mediate the cell type specific degradation of CK1 and Ikaros proteins through modification of lenalidomide structure by adding enzyme responsive moieties.

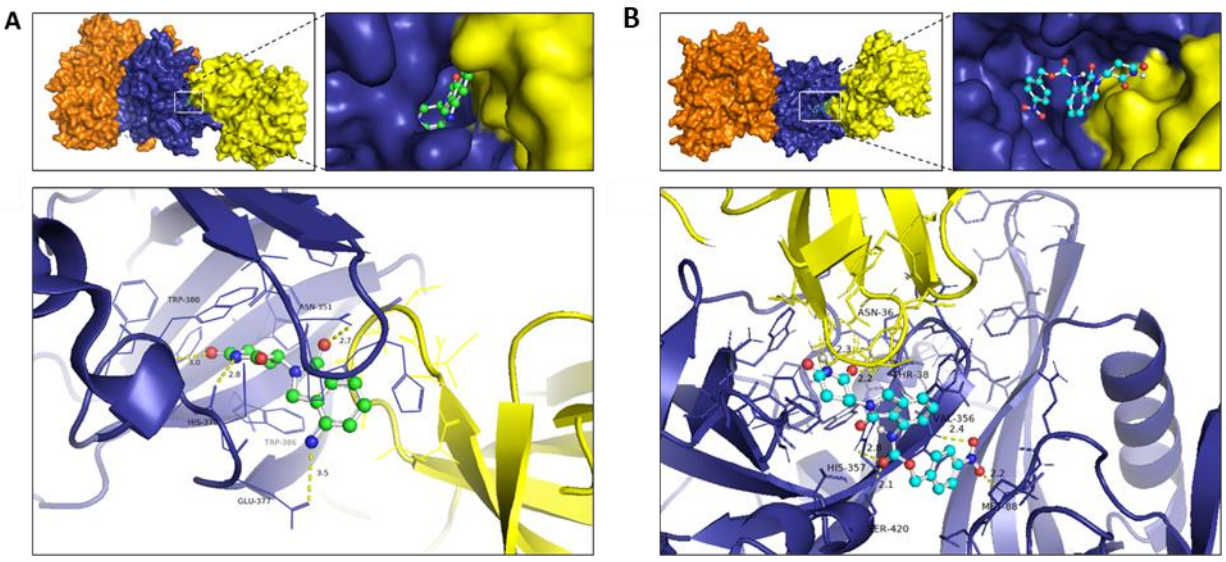

Figure 1. Structure restriction of lenalidomide interacting with CK1α and CRBN. A) Free Lenalindomide interacts with the C-terminal domain of CRBN which accommodates lenalidomide in a hydrophobic pocket. Yellow dash-lines indicate main hydrogen bonding. B) Modification of enalidomide with nitroreductase responsive moiety block the exclusive interaction of CK1α and CRBN.

After successful modification of NTR caging group, NTR-lenalidomide was examined its ability to release free lenalidomide compound upon nitroreductase enzyme activation. The dynamic enzyme response was monitored by LC-MS showing the time and concentration dependence of enzyme to NTR-Lenalidomide. Most of the lenalidomide was released after 1 hour incubation with the enzyme (Figure 2). This efficient uncaging method promises the specific induction of the therapeutic molecular glue at specific targeted cells where the enzyme is overexpressed.

The protein degradation effect of lenalidomide was observed in HEK293T cells. Upon treating with increased concentrations of lenalidomide, the increase in CK1α protein degradation was observed by western blot analysis (Figure 3A). We subsequently examined the degradation of CK1α protein upon incubation of the NTR-lenalidomide with hypoxia

cells. After hypoxia stress, the kinase level was significantly decreased with small molecule concentration dependence (Figure 3B). As a positive control, activity of lenalidomide was observed not to be affected under hypoxia condition. Meanwhile, NTR-lenalidomide was unable to degrade the protein under normal condition (Figure 3C). As a highly cell selective activation of lenalidomide, other cell type such as human breast cancer cell- MCF-7 experienced no degradation of CK1α protein after treating with different concentration of the molecular glue. Similarly, under hypoxia condition, NTR-lenalidomide was also not able to degrade the kinase in this cell line (Figure 4).

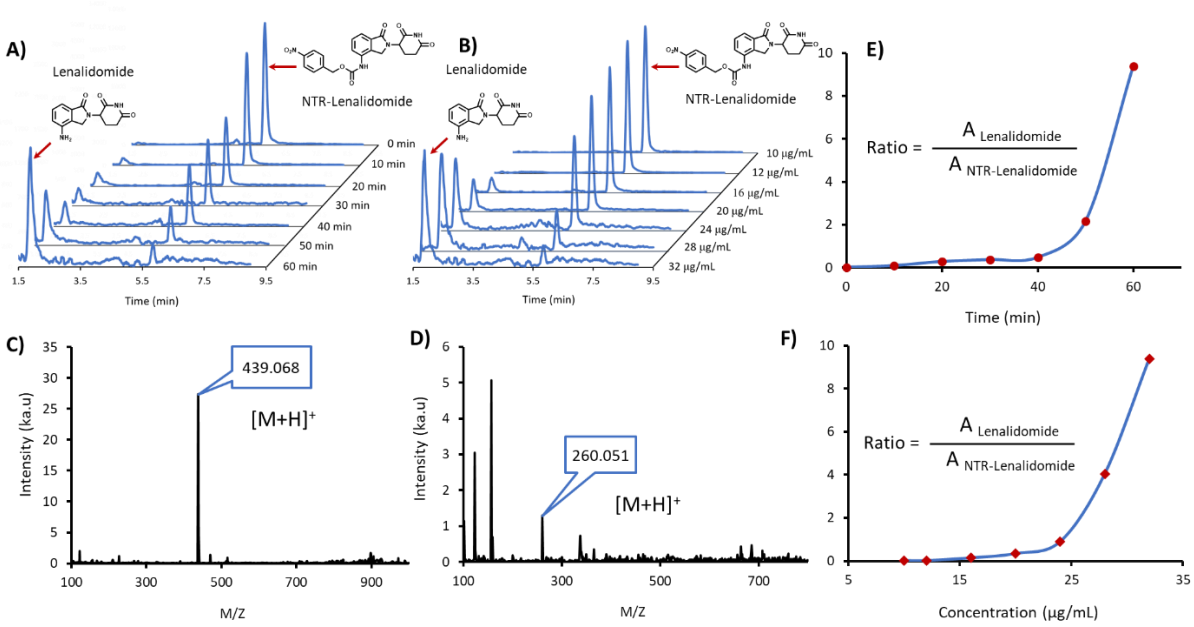

Figure 2. Nitroreductase enzyme response of NTR-Lenalidomide in time (A) and enzyme concentration (B) manner. ESI-MS detection of NTR-Lenalidomide (C) and cleaved free lenalidomide (D) after enzyme responsive. Relative abundance of lenalidomide and NTR-Lenalidomide during time (E) and concentration (F) of enzyme treatment was plotted showing the exponential kinetic.

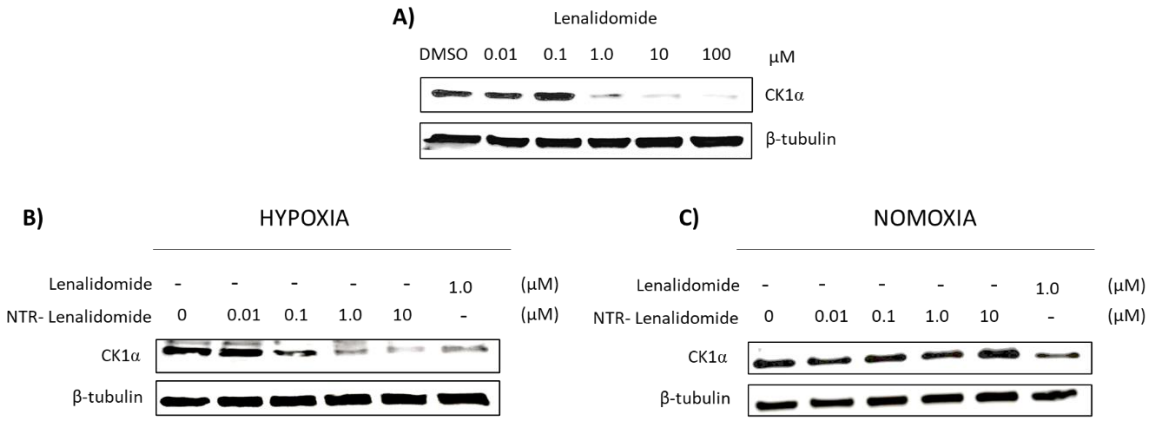

Figure 3. Western blot analysis of CK1α in HEK293T during concentration dependent treatment with A) lenalidomide, B) NTR-lenalidomide for 24 hours and C) NTR-lenalidomide under normoxia condition for 24 h.

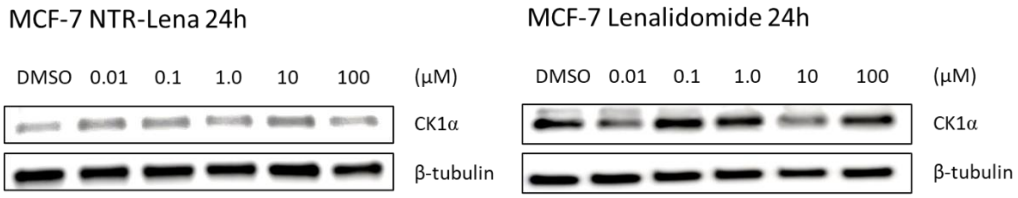

Figure 4. Western blot analysis of CK1α in MCF-7 cells during concentration dependent treatment with lenalidomide and NTR-lenalidomide (under hypoxia) for 24 hours.

In conclusion, this chapter illustrates one of the directions to specifically modulate the protein level in a cell-selective manner. In fact, molecular glue leverages multiple advantages compare to PROTAC compounds. The generally lower molecule weight enhances its cellular uptake and its biological applications. Different from the heterobifunctional compounds, molecular glues use one warhead to simultaneously target to both POI and ubiquitination ligase. Therefore, “hook effect” resulted from saturated presentation of the compounds intracellularly is minimized. These compounds are specialized by their highly cooperative binding in protein-protein interactions. Normally, no requirement of pocket on or affinity

needed for molecular glues which offer opportunities for degradation of unligandable proteins. However, the highly unique structure, protein target and binding make the discovery process of this kind of compound serendipitous and normally lack of rational finding. In this chapter, lenalidomide as molecular glue can be specifically controlled to release the drug activity. Further investigations of cellular behavior manipulations of the drug such as its potential in tumor growth inhibition or tweaking circadian rhythm of the target cells are promising. The study provides new insight to monitor protein degraders in cell-type specific manner, which is essential in precision medicine. Nevertheless, this direction seems to be a great challenge in PROTACs molecules in which addition of enzyme responsive moieties into the compound make the high molecular weight structure become more complicated and hinder their biological applications as clinical drugs.

5.3. Experimental details

5.3.1. Synthesis of NTR-Lenalidomide

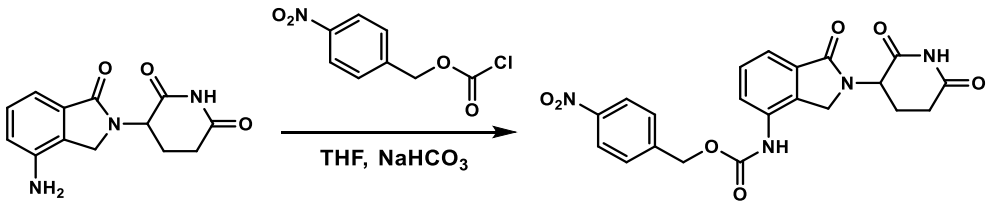

To a 25-mL round bottom flask was added lenalidomide (50 mg, 0.2 mmol) and sodium bicarbonate (45.6 mg) dissolved in tetrahydrofuran. The mixture was cooled to below 0 °C and was subsequently added the 4-nitrobenzyl chloroformate (43.1 mg, 0.2 mmol) in a dropwise manner. The mixture was slowly warmed to room temperature and was left to react for 5 hours. Upon reaction completion, the crude product was filtered and dried to yield a white solid ().

^{1}H NMR (400 MHz, DMSO-*d6*): δ 11.02 (s, 1H), 9.81 (s, 1H), 8.28 (d, *J* = 8.0 Hz, 2H), 7.81 – 7.89 (m, 1H), 7.71 (d, *J* = 8.0 Hz, 2H), 7.54 – 7.49 (m, 2H), 5.34 (s, 2H), 5.13 (dd, *J* = 16.0 Hz, 8.0 Hz, 2H), 4.46 (d, *J* = 16.0 Hz, 2H), 4.37 (d, *J* = 16.0 Hz, 2H), 2.97 – 2.87 (m, 1H), 2.68 – 2.59 (m, 1H), 2.39 – 2.28 (m, 1H), 2.09 – 2.01 (m, 1H). ^{13}C NMR (100 MHz, $(CD_3)_2SO$): δ 172.9, 171.1, 167.8, 153.5, 147.2, 144.4, 133.7, 132.9, 128.9, 128.6, 123.7, 118.8, 64.9, 51.6, 46.3, 31.2, 22.6.

5.3.2. Nitroreductase enzyme responsive of NTR-Lenalidomide

NTR-Lenalidomide (10 mM) was sequentially mixed nicotinamide adenine dinucleotide NADH (0.5 mM) and nitroreductase (0-32 μg/mL) dissolving in PBS (pH 7.4, 10 mM) into a total volume of 500 μL. The mixture in the vial was vortexed and was incubated at 37 °C with varying time control from 0 – 60 mins. Structural mass analysis was performed by ThermoFinnigan LCQ Deca XP MAX Mass instrument to observe any molecular mass alteration and quantification of peak areas.

5.3.3. Western-blot analysis of CK1α protein

The lysates of each group of cells at different times and concentration treatment of NTR-lenalidomide under hypoxia or normoxia were collected and centrifuged at 13,000 × g for 20 min at 4 ℃. Protein levels in supernatants were determined using Nanodrop and equalized to the same concentration and boiled for 5 min with SDS-PAGE sample loading buffer before being separated using SDS-PAGE and transferred to the PVDF membrane. The membrane was then blocked with 5% BSA-TBST blocking buffer overnight at 4 ℃. Subsequently, CK1α Rabbit polyclonal Antibody (Abcam) was incubated overnight at 4 ℃ in 1% BSA-TBST buffer. After series of washing, the goat-anti rabbit IGG (H&L) secondary antibody

(Abcam) was added and incubated for 1 hour in 1% BSA-TBST. All signals were visualized using AMERSHAM (Image quant 800) system.

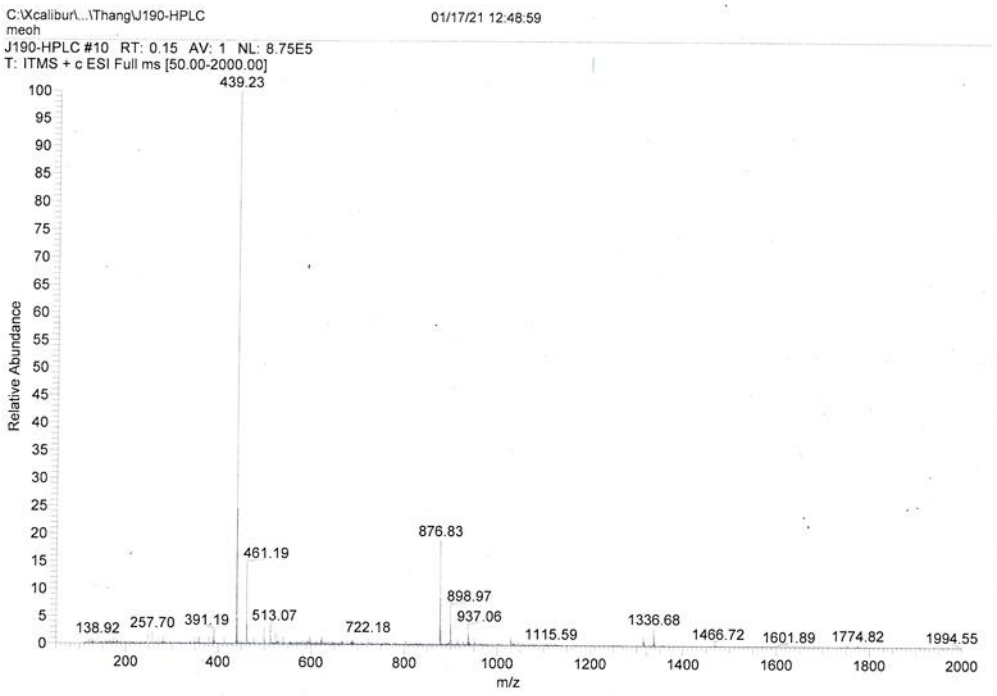

Figure S1. MS (ESI) Spectra of NTR-Lenalidomide.

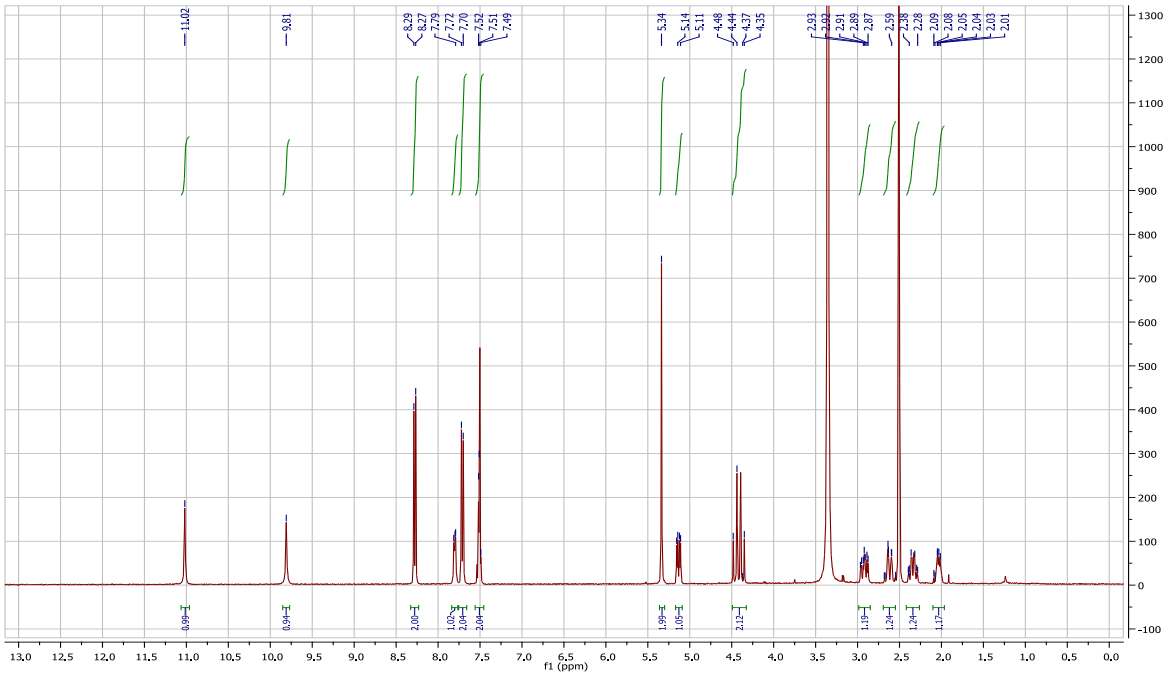

Figure S2. ^{1}H NMR of NTR-Lenalidomide

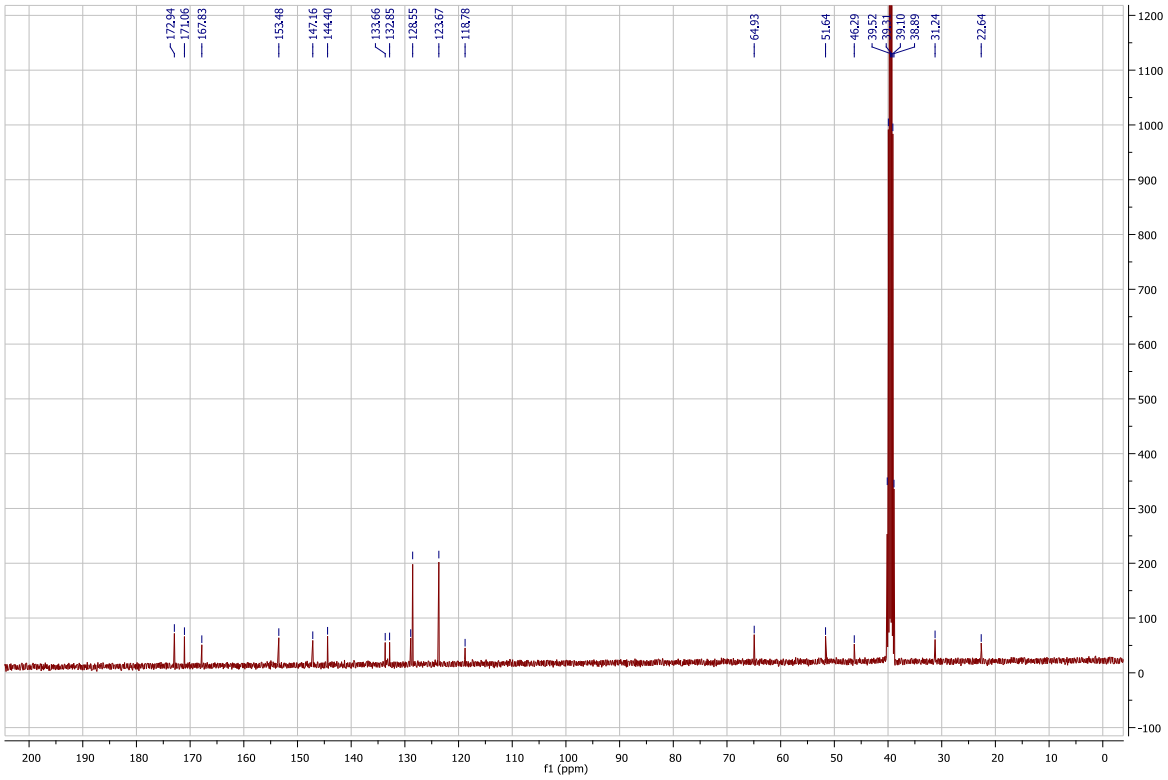

Figure S3. ^{13}C NMR of NTR-Lenalidomide

5.4. References

1. Gandhi, A. K.; Kang, J.; Havens, C. G.; Conklin, T.; Ning, Y.; Wu, L.; Ito, T.; Ando, H.; Waldman, M. F.; Thakurta, A.; Klippel, A.; Handa, H.; Daniel, T. O.; Schafer, P. H.; Chopra, R. Immunomodulatory agents lenalidomide and pomalidomide co-stimulate T cells by inducing degradation of T cell repressors Ikaros and Aiolos via modulation of the E3 ubiquitin ligase complex CRL4(CRBN.). *Br. J. Haematol.* **2014**, *164*, 811-21.

2. Quach, H.; Ritchie, D.; Stewart, A. *Neeson, P.; Harrison, S.; Smyth, M. J. Prince, H. M.* Mechanism of action of immunomodulatory drugs (IMiDS) in multiple myeloma. *Leukemia* **2010**, *24*, 22–32.

3. Lindner, S.; Krönke, J. The molecular mechanism of thalidomide analogs in hematologic malignancies. *J. Mol. Med. (Berl).* **2016**, *94*, 1327-1334.

4. Ito, T.; Ando, H.; Suzuki, T.; Ogura, T.; Hotta, K.; Imamura, Y.; Yamaguchi, Y.; Handa, H. Identification of a primary target of thalidomide teratogenicity. *Science*. **2010**, *327*, 1345-1350.

5. Broyl, A.; Kuiper, R.; van Duin, M.; van der Holt, B.; el Jarari, L.; Bertsch, U.; Zweegman, S.; Buijs, A.; Hose, D.; Lokhorst, H. M.; Goldschmidt, H.; Sonneveld, P.; Dutch-Belgian HOVON group; German GMMG Group. High cereblon expression is associated with better survival in patients with newly diagnosed multiple myeloma treated with thalidomide maintenance. *Blood* **2013**, *121*, 624-627.

6. Zhang, L. H.; Kosek, J.; Wang, M.; Heise, C.; Schafer, P. H.; Chopra, R. Lenalidomide efficacy in activated B-cell-like subtype diffuse large B-cell lymphoma is dependent upon IRF4 and cereblon expression. *Br. J. Haematol.* **2013**, *160*, 487-502.

7. Zhu, Y. X.; Braggio, E.; Shi, C. X.; Bruins, L. A.; Schmidt, J. E.; Van Wier, S.; Chang, X. B.; Bjorklund, C. C.; Fonseca, R.; Bergsagel, P. L.; Orlowski, R. Z.; Stewart, A. K. Cereblon expression is required for the antimyeloma activity of lenalidomide and pomalidomide. *Blood* **2011**, *118*, 4771-4779.

8. Krönke, J.; Udeshi, N. D.; Narla, A.; Grauman, P.; Hurst, S. N.; McConkey, M.; Svinkina, T.; Heckl, D.; Comer, E.; Li, X.; Ciarlo, C.; Hartman, E.; Munshi, N.; Schenone, M.; Schreiber, S. L.; Carr, S. A.; Ebert, B. L. Lenalidomide causes

selective degradation of IKZF1 and IKZF3 in multiple myeloma cells. *Science* **2014**, *343*, 301-305.

9. Lu, G.; Middleton, R. E.; Sun, H.; Naniong, M.; Ott, C. J.; Mitsiades, C. S.; Wong, K. K.; Bradner, J. E.; Kaelin, W. G. Jr. The myeloma drug lenalidomide promotes the cereblon-dependent destruction of Ikaros proteins. *Science* **2014**, *343*, 305-309.

10. Awwad, M. H. S.; Kriegsmann, K.; Plaumann, J.; Benn, M.; Hillengass, J.; Raab, M. S.; Bertsch, U.; Munder, M.; Weisel, K.; Salwender, H. J.; Hänel, M.; Fenk, R.; Dürig, J.; Müller-Tidow, C.; Goldschmidt, H.; Hundemer, M. The prognostic and predictive value of IKZF1 and IKZF3 expression in T-cells in patients with multiple myeloma. *Oncoimmunology* **2018**, *7*, e1486356.

11. Marke, R.; Havinga, J.; Cloos, J.; Demkes, M.; Poelmans, G.; Yuniati, L.; van Ingen Schenau, D.; Sonneveld, E.; Waanders, E.; Pieters, R.; Kuiper, R. P.; Hoogerbrugge, P. M.; Kaspers, G. J.; van Leeuwen, F. N.; Scheijen, B. Tumor suppressor IKZF1 mediates glucocorticoid resistance in B-cell precursor acute lymphoblastic leukemia. *Leukemia* **2016**, *30*, 1599-603.

12. Marke, R.; van Leeuwen, F. N.; Scheijen, B. The many faces of IKZF1 in B-cell precursor acute lymphoblastic leukemia. *Haematologica* **2018**, *103*, 565-574.

13. Thomas, R. M.; Chunder, N.; Chen, C.; Umetsu, S. E.; Winandy, S.; Wells, A. D. Ikaros enforces the costimulatory requirement for IL2 gene expression and is required for anergy induction in CD4+ T lymphocytes. *J, Immunol*. **2007**, *179*, 7305-73015.

14. Krönke, J.; Fink, E. C.; Hollenbach, P. W.; MacBeth, K. J.; Hurst, S. N.; Udeshi, N. D.; Chamberlain, P. P.; Mani, D. R.; Man, H. W.; Gandhi, A. K.; Svinkina, T.;

Schneider, R. K.; McConkey, M.; Järås, M.; Griffiths, E.; Wetzler, M.; Bullinger, L.; Cathers, B. E.; Carr, S. A.; Chopra, R.; Ebert, B. L. Lenalidomide induces ubiquitination and degradation of CK1α in del(5q) MDS. *Nature* **2015**, *523*, 183-188.

15. Petzold, G.; Fischer, E. S.; Thomä, N. H. Structural basis of lenalidomide-induced CK1α degradation by the CRL4(CRBN) ubiquitin ligase. *Nature* **2016**, *532*, 127-130.

Chapter 6. Conclusions and Future Works

The development of precision medicine required detail cellular monitoring with comprehensive understanding of therapeutic agent's action mechanism. This direction requires subcellular precise targeting and manipulating with localized chemical engineering. Non-genetic remodeling methods broaden the applications of subcellular targeting in cellular manipulations. Various cellular compartments including the cell membrane, lysosome, ER, Golgi apparatus and nucleus with chemical engineering were summarized in chapter 1. In chapter 2, detail subcellular localization of photothermal nanoparticles and its effects were investigated showing that activation of nanoheaters on the cell membrane and intracellularly uptake resulted in different photothermal cell death pathways. These differences suggest that simple targeting of nanoparticles to some specific cellular compartments might significantly regulate the cell functions. To further provide the cell-selective targeting of therapeutic agents, enzyme responsive labeling of the cell membrane was reported in chapter 3. Furin as an important proteolytic enzyme was selected for the study. After removing the enzyme substrate peptide sequence, free azide-sugars were released which enables the metabolic labeling of the enzyme-overexpressed cell membrane. This method showed stable and prolonged conjugation of reagents on the cell membrane. These observations suggest future direction for the opportunity of prolonged cell membrane protein or ion channel regulation using chemical agents.

To further enhance the subcellular chemical engineering, protein was our next target. In this thesis, we focus on proteolysis targeting chimeras (PROTACs) which are recently emerged as new principle of pharmacological developments targeting loss of protein balancing. Traditional method such as CRISPR-Cas, si/shRNA techniques, or antisense oligonucleotides

are established but still facing tremendous difficulties mainly from delivery and safety challenges. PROTAC technology overcomes regular protein inhibitors by its general substoichiometric target occupancy, sustainable pharmacodynamic effects with catalytic functions. Depletion of protein minimizes the possibility of drug resistance through mutation. These heterobifunctional molecules enable targeting of traditionally undruggable proteins with reduced time and dosage. In chapter 4, we introduced PROTAC molecules targeting degradation of an important casein kinase 2α. Our compound showed the ability to degrade the targeted protein in time, concentration, and cell linage dependances through immunostaining and western blot analysis. The effect was also observed in zebrafish showing its ability to degrade the protein *in vivo*. However, the high molecular weight which deviates from the conventional "rule of five" for drug-like molecule properties limit their cellular uptake, compromise bioavailability and pharmacokinetics, especially distribution to the central nervous system and therefore constrained its application in systematic practices. Additionally, there are still minimum methods to specifically degrade the protein intracellularly due to its lack of controllable moieties in the compound structures. Addition of light responsive or enzyme responsive moieties to the traditional bifunctional compounds make the system more complicated and give the higher molecule weight compounds. In chapter 5, we introduced a strategy to provide cell selective degradation of protein with the construction of enzyme responsive into a molecule glue with simple and small architecture. The NTR-lenalidomide under nitroreductase presentation can release free lenalidomide to degrade another essential kinase, CK1α. This proof-of-concept studies open new insights toward the possibility of precise manipulation of protein level using small molecules. However, due to the specialty of the molecule glue with unique properties to connect both POI and the ubiquitin machinery, the extension of the method is limited and still cannot

universally be applicable to all protein degraders. Therefore, future development towards revising chemical structure designs of PROTACs and molecular glues are still under high demand. Further investigations of cellular function perturbations by CK2α and CK1α degradations are proceeding together with chemical structure reorganization to minimize all the drawbacks of PROTACs and molecular glues by our group.

Overall, this thesis provides different insights and directions for the development of precision medicine. Rather than investigating new methods for different subcellular cell location targeting, the thesis mainly focusing on the significances of the organelle targeting in manipulating cellular events. By providing practical evidence in the distinguished cell death pathways induced by different locations of photothermal nanoparticles, the results from chapter 2 of the thesis reveal that, meaningful outcomes might not only come from enhancing the nanoparticles or reagents, but also by manipulating its distribution and behaviors in the complex living conditions. Additionally, further enhancement of the subcellular targeting can be achieved by adding the cell-type selection of a subcellular targeting reagent. The results from chapter 3 in the thesis provide a new method for the combination of different cell and subcellular targeting for more efficient labelling or therapy. In addition, targeting reagent can be used to induce protein-protein interactions and degradation of the proteins. The results from chapter 4 and 5 describe PROTAC and molecular glue for manipulation of protein balancing which is importance for the cellular function regulations. This new application of protein targeting approach can be further extended by using a cell-type selective protocol using enzyme regulation. I believe that the directions provided in this thesis will foster the development of chemical-biology based translational medicine in the future.

List of publications

1. **Do Cong Thang**, Zhimin Wang, Xiaoling Lu, Bengang Xing. * Precise Cell Behaviors Manipulations Through Light-Responsive Nano-regulators: Recent Advance and Perspective. *Theranostics*, **2019**, *9*, 3308.
2. Zhimin Wang, **Do Cong Thang**, Xuan Zhao, Xilei Xie, Zhiyong Wang, Jun Lin, Bengang Xing*. Near-Infrared Photo-controlled Therapeutic Release *Via* Upconversion Nanocomposites. *J. Control. Release*. **2020**, *324*, 104.
3. **Do Cong Thang**, Zhimin Wang, Ming Hu, Qinyu Han, Bengang Xing*. Extra-Specific Manifestation of Nanoheater's Position Effect on Distinctive Cellular Photothermal Response. *ACS Nano*, **2020**, *14*, 5836.
4. Qinyu Han, Jun Wei Lau, **Do Cong Thang**, Zhijun Zhang*, Bengang Xing*. Near-infrared Light Brightens Bacterial Disinfecton: Recent Progress and Perspectives. *ACS Applied Bio. Mater.* **2021**, *5*, 3937.
5. Germain Kwek, **Do Cong Thang**, Xiaoling Lu, Jun Lin, Bengang Xing*. Scratching the Surface of Unventured Possibilities within situ Self-assembly: Protease Activated Developments for Imaging and Therapy. *ACS Applied Bio. Mater*. **2021**, *4*, 2192.
6. . Zhimin Wang^{+}, **Do Cong Thang**$^{+}$, Wenbin Zhong, Jun Wei Lau, Germain Kwek, Mary B. Chan-Park, Bengang Xing. Cyanine-Dyad Molecular Probe for Simutaneous Profliling of Multiple Radical Species Evolution in Bacterial Infection. *Angew. Chem. Intl. Ed*. **2021**, *60*, 16900-16905. (**Equal contribution)**
7. Liangliang Liang†, Ziwei Feng†, Qiming Zhang†, **Do Cong Thang**, Yu Wang, Xian Qin, Zhigao Yi, Melgious Jin Yan Ang, Lei Zhou, Han Feng, Bengang Xing, Min Gu*, Xiangping Li* & Xiaogang Liu*. Continuous-wave Near-IR STED Microscopy using

Downshifting Lanthanide Nanoparticles. *Nature Nanotechnology*, **2021**. DOI: 10.1038/s41565-021-00927-y.

8. Patent: **Xing Bengang***, **Do Cong Thang**. Enzyme Triggered Degradation of Tumor Circadian: A New and Unique Drug-Free Strategy for Specific Cancer Therapy. Patent number: 10202104740P.